

1 **VESIcal Part II: A critical approach to volatile**
2 **solubility modelling using an open-source Python3**
3 **engine.**
4 **PLEASE SEE FINAL JOURNAL PDF, AVAILABLE**
5 **OPEN ACCESS, WHICH HAS SOME TYPOS**
6 **CORRECTED AND BETTER FORMATTING!**
7 **<https://doi.org/10.1029/2021EA001932>**

8 **P. E. Wieser^{1,2*}, K. Iacovino³, S. Matthews⁴, G. Moore³, C. M. Allison^{5,6}**

9 ¹Department of Earth Sciences, University of Cambridge, UK.

10 ²College of Earth, Ocean and Atmospheric sciences, Oregon State University

11 ³Jacobs, NASA Johnson Space Center, Houston, TX 77058, USA.

12 ⁴Johns Hopkins University, Department of Earth and Planetary Sciences, Baltimore, MD 21218, USA.

13 ⁵Cornell University, Department of Earth and Atmospheric Sciences, Ithaca, NY 14853

14 ⁶City College of New York, City University of New York, New York, NY 10031

15 **Key Points:**

- 16 • The Python3 tool VESIcal allows extensive comparisons to be drawn between
17 different H₂O-CO₂ solubility models
- 18 • Solubility models are not interchangeable - for a single magma composition,
19 different models can predict a wide range of solubility relationships
- 20 • The P-T-X calibration range of each solubility model must be critically evalu-
21 ated before application to a specific volcanic system

Corresponding author: P. Wieser, penny.wieser@gmail.com

22 **Abstract**

23 Accurate models of H₂O and CO₂ solubility in silicate melts are vital for under-
24 standing volcanic plumbing systems. These models are used to estimate the depths
25 of magma storage regions from melt inclusion volatile contents, investigate the role
26 of volatile exsolution as a driver of volcanic eruptions, and track the degassing paths
27 followed by magma ascending to the surface. However, despite the large increase
28 in the number of experimental constraints over the last two decades, many recent
29 studies still utilize the earlier generation of models, which were calibrated on ex-
30 perimental datasets with restricted compositional ranges. This may be because
31 many of the available tools for more recent models require large numbers of input
32 parameters to be hand-typed (e.g., temperature, concentrations of H₂O, CO₂, and
33 8–14 oxides), making them difficult to implement on large datasets. Here, we use a
34 new open-source Python3 tool, VESIcal, to critically evaluate the behaviours and
35 sensitivities of different solubility models for a range of melt compositions. Using
36 literature datasets of andesitic-dacitic experimental products and melt inclusions
37 as case studies, we illustrate the importance of evaluating the calibration dataset
38 of each model. Finally, we highlight the limitations of particular data presentation
39 methods such as isobar diagrams, and provide suggestions for alternatives, and best
40 practices regarding the presentation and archiving of data. This review will aid the
41 selection of the most applicable solubility model for different melt compositions, and
42 identifies areas where additional experimental constraints on volatile solubility are
43 required. (242/250 words)

44 **Plain Language Summary**

45 Being able to accurately model the solubility of H₂O and CO₂ in magmas is
46 very important for understanding a wide variety of volcanic processes, such as the
47 depths at which magma is stored in the crust, the driving force behind volcanic
48 eruptions, and the release of volatile elements into the atmosphere. However, there
49 has been no easy way for volcanologists to perform calculations on large datasets,
50 or to compare different models. This review uses a new, open-source tool called
51 VESIcal written in the popular programming language Python3. This allows us to
52 compare different models for a wide variety of melt compositions, temperatures and
53 pressures, helping researchers to identify the most suitable model for their study.

54 We also suggest areas where further experimental constraints are required. Finally,
55 we highlight the limitations of particular data presentation methods such as isobar
56 diagrams, and provide suggestions for alternatives, and best practices regarding the
57 presentation and archiving of data.

58 **1 Introduction**

59 The most abundant volatile components found in terrestrial magmatic systems
60 are H₂O and CO₂. It has been known for nearly a century (Bowen, 1928; Tuttle &
61 Bowen, 1958) that these volatile species have profound effects on the chemical and
62 material properties of magmas (e.g., phase equilibria, melting temperatures, magma
63 viscosity and density; Burnham, 1979; Husen et al., 2016; Burnham & Davis, 1974;
64 Hess & Dingwell, 1996; Ochs & Lange, 1999), so significantly affect their geochem-
65 ical and dynamical behavior (e.g., eruption and degassing style, erupted volume;
66 Papale et al., 1999; Huppert & Woods, 2002; La Spina et al., 2021). Thus, it is vital
67 to be able to predict how H₂O and CO₂ solubilities change as a function of inten-
68 sive variables such as pressure, temperature, melt and fluid composition in order to
69 understand plutonic and volcanic systems.

70 The solubility of a volatile species is defined at a given pressure and temper-
71 ature as the maximum concentration that can be dissolved within a silicate melt
72 of a specified composition. Ignoring disequilibrium effects, if the volatile content of
73 the system exceeds this solubility limit, a separate fluid/vapour phase will exsolve
74 from the magma. In this review, we favour the term fluid because of the supercrit-
75 ical nature of exsolved volatile phases at magmatic temperatures. In general terms,
76 a magma is described as volatile undersaturated when there is no fluid phase, and
77 volatile saturated once a fluid phase is present (also referred to as vapour under-
78 saturated/saturated, or fluid undersaturated/saturated). In detail, different volatile
79 species do not act as independent entities, but influence one another. For this rea-
80 son, a magma may exsolve a mixed CO₂-H₂O fluid even if the dissolved concentra-
81 tions of H₂O and CO₂ do not exceed the pure solubility limit of each species.

82 Despite the obvious importance of accurate volatile solubility modelling, very
83 few studies of volcanic systems have evaluated results using several different sol-
84 ubility models to determine possible sources of systematic and random error, and

85 assess the suitability of each model for the conditions of interest (e.g. temperature,
86 pressure, and melt composition). This lack of intercomparison likely results from the
87 fact that it is extremely time consuming to perform the large numbers of calcula-
88 tions necessary for thorough comparisons using available tools. For example, many
89 solubility models were released as stand-alone Excel spreadsheets (e.g., G. Moore
90 et al., 1998; Newman & Lowenstern, 2002; Allison et al., 2019) or web apps (e.g.,
91 Iacono-Marziano et al., 2012; Ghiorso & Gualda, 2015), where saturation pressures,
92 dissolved volatile contents, degassing paths, and isobars can only be calculated for
93 one sample and set of conditions at a time. The more recent models which include
94 several terms accounting for the effect of melt composition on volatile solubility
95 require users to hand-type a large number of input parameters. For example, to
96 calculate a saturation pressure in MagmaSat (Ghiorso & Gualda, 2015), users must
97 hand-type 9–14 oxide concentrations in addition to entering H₂O and CO₂ concen-
98 trations, and a melt temperature. Similarly, the web app of Iacono-Marziano et al.
99 (2012) requires users to input 8 major element oxide concentrations. Calculating
100 isobars using these web apps is a particularly daunting task, as users must evaluate
101 dissolved volatile contents at multiple fluid compositions, and then use curve fitting
102 to produce a smooth isobar to display on plots. Other models were released with no
103 calculator at all, requiring each user to correctly interpret and combine the relevant
104 equations in the manuscript (Dixon, 1997; Shishkina et al., 2014).

105 Here, we take advantage of the recent release of VESIcal (Volatile Equilibria
106 and Saturation Identification calculator; Iacovino et al., 2021), an open-source tool
107 written in Python3. VESIcal contains functions to calculate saturation pressures,
108 dissolved volatile contents, isobars, and degassing paths automatically for seven dif-
109 ferent models. Calculations can be performed based on melt compositions provided
110 in an Excel spreadsheet, and users can take full advantage of Python’s extensive
111 flexibility to perform large numbers of calculations automatically (e.g., creating for
112 loops to perform calculations across a range of pressures, temperatures, and fluid
113 compositions). To our knowledge, the only other model with similar functionality to
114 VESIcal is the Linux program Solwcad supplied by Papale et al. (2006), which per-
115 forms calculations automatically on a user-supplied .txt file containing melt composi-
116 tions, pressures and temperatures (<http://www.pi.ingv.it/progetti/eurovolc/>).

117 Solwcad was used alongside VESICAL in this review, through the Windows Subsystem
118 for Linux (WSL2).

119 The overall aim of this review is to summarize the formulation, strengths and
120 weaknesses of popular solubility models to inform users who wish to model volatile
121 solubility in silicate melts, whether that be the calculation of melt inclusion saturation
122 pressures, degassing paths, incorporating volatile exsolution in physical model of
123 magma chambers (e.g. Huber et al., 2019), or calculating the dissolved volatile con-
124 tents of fluid-saturated experimental products where the pressure, temperature and
125 exsolved fluid composition are known (e.g. Waters & Lange, 2015). Specifically, we
126 demonstrate in a number of ways how users investigating a specific subset of compo-
127 sitional space (e.g., melt inclusions from a single volcano) can assess the similarities
128 and differences between models, and evaluate these findings in the context of the
129 calibration dataset and formulation of each model. We start by briefly summarizing
130 the major results from volatile solubility experiments over the last century (section
131 2), before describing nine of the most popular solubility models (section 3). We then
132 compare the solubility of pure H₂O, mixed H₂O-CO₂, and pure CO₂ predicted by
133 different models for representative mafic and silicic compositions (section 4). We
134 also explore the sensitivity of these models to parameters such as temperature and
135 redox state, which are often poorly constrained in igneous systems (section 5). Fi-
136 nally, we evaluate the suitability of these models for intermediate melt compositions,
137 where experimental constraints are sparse relative to basaltic and rhyolitic melts
138 (section 6). We conclude by discussing best practices for presenting and archiving
139 data related to volatile components in igneous systems (section 7). Overall, these
140 discussions demonstrate that there are large differences between model outputs,
141 even in relatively "normal" melt compositions, so the choice of solubility model is a
142 critical part of any study investigating magmatic volatiles (and needs to be justified
143 in all cases). This manuscript will act as a guide to help users assess the suitability
144 of each model for their specific application (supplemented by the python code pro-
145 vided in the supporting information, which can be easily adapted to evaluate melt
146 compositions and conditions relevant to a specific study).

2 Major findings from experimental studies investigating volatile solubility in magmas

One of the earliest volatile studies was that of Goranson (1931), who investigated the effect of pressure on the solubility of water in granitic melts. The classic treatise of Tuttle and Bowen (1958) investigated the impact of H₂O on mineral phase equilibrium. This study led to a wider recognition of the importance of volatiles, and motivated the development of experimental and analytical approaches to determining volatile solubilities as a function of pressure, temperature, and melt composition. Hamilton et al. (1964) was one of the first to compare H₂O solubilities for differing melt compositions (basalt and andesite), while also investigating the effect of dissolved H₂O and oxidation state on the magmatic phase equilibria. These studies were followed by the fundamental experimental measurements of the Burnham group on the dissolution of H₂O in albite melts (e.g., Burnham & Davis, 1971, 1974).

Further investigation of volatile solubility over the next four decades in natural samples and experimental products was aided significantly by analytical developments, allowing volatile contents in quenched glasses to be measured by techniques such as Fourier Transform infra-red spectroscopy (FTIR; e.g., Stolper, 1982; Fine & Stolper, 1986; Silver et al., 1990) and secondary ion mass spectrometry (SIMS; Hervig & Williams, 1988; Hauri, 2002). In particular, the high spatial resolution of FTIR and SIMS (a few tens of micrometers) meant that volatile concentrations could be measured within quenched pockets of melt trapped within crystals (termed melt inclusions). Unlike subaerially-erupted lavas which have degassed almost all their H₂O and CO₂ following their ascent to shallow pressures, melt inclusions remain pressurized during ascent as they are trapped in relatively incompressible crystals, so retain high volatile contents (Roedder, 1979; Anderson, 1974).

Melt inclusion analyses have greatly advanced our understanding of the behavior of volatiles in volcanic systems (Lowenstern, 2003; Hauri et al., 2002; Roggensack, 2001; Wallace et al., 1995; Métrich & Wallace, 2008; Sides et al., 2014a). For example, melt inclusions provide insights into pre-eruptive volatile contents (e.g., Saal et al., 2002; Hervig et al., 1989), and links between melt volatile contents and eruption styles (Lucic et al., 2016). The strong pressure-dependence on volatile solubility means that H₂O and CO₂ contents within melt inclusions trapped from a

180 volatile-saturated magma can be used to determine the pressure at which the inclu-
181 sion was sealed off (termed the saturation pressure or entrapment pressure). In turn,
182 the distribution of saturation pressures in a suite of melt inclusions can reveal the
183 locations of the main regions of magma storage in a volcanic system. This explosion
184 of new information from melt inclusions greatly increased the demand for flexible
185 and accurate solubilities models that could be applied to a broad range of pressures,
186 temperatures, and melt/fluid compositions (G. Moore, 2008; Ghiorso & Gualda,
187 2015).

188 It has become increasingly apparent from solubility experiments that the
189 solubility of H₂O is relatively insensitive to melt composition (e.g., G. Moore &
190 Carmichael, 1998; Shishkina et al., 2010), while CO₂ solubility is highly sensitive
191 to melt composition, particularly in mafic melts where the carbonate ion is the
192 dominant species (Dixon, 1997; Brooker et al., 2001a; Shishkina et al., 2010; Iacono-
193 Marziano et al., 2012; Shishkina et al., 2014; Allison et al., 2019). This has lead to
194 a great diversity in the way that various models treat the dependence of CO₂ sol-
195 ubility on melt composition. In general, models have become more complex with
196 time as the region of compositional space spanned by solubility experiments has in-
197 creased to include more alkaline lavas. The individual role and relative importance
198 of each cation species in the melt is still associated with a large degree of uncer-
199 tainty (Allison et al., 2019), accounting for the larger discrepancies between different
200 model predictions for CO₂ vs. H₂O.

201 Experimental work has also highlighted the complexities of mixing between
202 H₂O and CO₂ in igneous systems. In the simplest case, the addition of one com-
203 ponent in a melt-fluid system decreases the activity, and therefore the solubility of
204 the other component in the melt (Lowenstern, 2001). This behavior is referred to as
205 Henrian/ideal behavior. Henry's Law states that the amount of a volatile dissolved
206 in a liquid is proportional to its partial pressure in the gas phase in equilibrium with
207 that liquid. Neglecting the possible entropic effects of speciation, the addition of
208 H₂O to the fluid/gas phase acts to lower the partial pressure of CO₂, and therefore
209 lowers the solubility of CO₂ in the liquid. Similarly, addition of CO₂ to the fluid/gas
210 phase causes the solubility of H₂O in the melt to decrease.

211 Experimental studies have shown that Henry's law is generally obeyed at low
212 pressures (<1 kbar) in basaltic (Dixon et al., 1995) and rhyolitic melts (Blank et al.,
213 1993). However, at higher pressures, some experimental observations have shown
214 that the mixing behavior of CO₂ and H₂O becomes strongly non-Henrian (Papale,
215 1999). For example, Eggler (1973), Mysen et al. (1976) and Mysen (1976) show that
216 the solubility of CO₂ in albitic melts increases with the addition of H₂O at higher
217 pressures. This has been attributed to the fact that the addition of small amounts
218 of water as OH⁻ species decreases melt polymerization, and therefore enhances the
219 solubility of CO₂ relative to an entirely anhydrous melt. After a certain amount of
220 H₂O is added, solubility decreases once more because the addition of H₂O to the
221 fluid phase causes the fugacity of CO₂ to decrease (Mysen, 1976; Dingwell, 1986;
222 King & Holloway, 2002). More recently, this behavior has been demonstrated for
223 dacitic and rhyolitic melts by Behrens et al. (2004) and Liu et al. (2005).

224 The non-ideal behavior of H₂O and CO₂ in basaltic and andesitic melts at
225 higher pressures is less well constrained. King and Holloway (2002) show that at
226 1 kbar, andesitic melts (SiO₂=58.4 wt%) exhibit a sharp increase in the solubility
227 of CO₃²⁻ species with increasing melt H₂O contents between 0–3.39 wt%. In con-
228 trast, Jakobsson (1997) show that the solubility of CO₂ in an icelanditic melt (54.6
229 wt% SiO₂) at 10 kbar is essentially constant, despite variation in melt water con-
230 tents between ~1–9 wt%. Similar behaviour to that observed by Jakobsson (1997)
231 was noted for andesitic magmas (57.4 wt% SiO₂) at 5 kbar by Botcharnikov et al.
232 (2006), who suggest that differences between H₂O-CO₂ mixing in their experiments
233 and those of King and Holloway (2002) may result from differences in oxygen fu-
234 gacity of these experiments (Fe³⁺/Fe_T=0.2–0.6 vs. Fe³⁺/Fe_T=0.09–0.2). However,
235 as we discuss in section 4.1, the influence of oxygen fugacity on volatile solubility
236 is still poorly constrained. Recent basaltic H₂O-CO₂ experiments generally show a
237 relatively flat plateau for CO₂ solubility with increasing melt H₂O contents between
238 ~0–4 wt% (Iacono-Marziano et al., 2012; Shishkina et al., 2010, 2014), although
239 relatively large error bars on analyses of CO₂ in experimental products make it dif-
240 ficult to determine whether this plateau is truly flat, or shows a slight positive or
241 negative gradient at low H₂O contents (see Fig. 7a of Iacono-Marziano et al., 2012).
242 The effect of H₂O-CO₂ mixing in the 9 solubility models evaluated here is discussed
243 further in sections 4.2.2 and 4.3.2.

3 Models discussed in this review

In this review, we focus on the seven models implemented in VESICAL (Iacovino et al., 2021):

1. The simplified parameterization of the Dixon (1997) model for H₂O and CO₂, which was implemented in the popular Excel tool VolatileCalc (Newman & Lowenstern, 2002), hereafter VolatileCalc-Basalt.
2. The H₂O model of G. Moore et al. (1998), hereafter M-1998.
3. The H₂O and CO₂ models of Liu et al. (2005), hereafter L-2005.
4. The H₂O and CO₂ models of Iacono-Marziano et al. (2012), hereafter IM-2012.
5. The H₂O and CO₂ models of Shishkina et al. (2014), hereafter S-2014.
6. The combined H₂O and CO₂ model of Ghiorso and Gualda (2015), hereafter MagmaSat.
7. The CO₂ models of Allison et al. (2019), hereafter A-2019.

We also consider the two additional models, reflecting both their popularity and relative ease of calculation using previously published tools:

8. The combined H₂O and CO₂ model of Papale et al. (2006), hereafter P-2006, accessed using the Linux program solwcad.
9. The Rhyolite functions in the VolatileCalc spreadsheet, hereafter VolatileCalc-Rhyolite

We do not consider the models of X. Duan (2014), Eguchi and Dasgupta (2018), or Burgisser et al. (2015) because no tool exists to automate the necessary calculations. We also do not discuss models with more limited pressure (P), temperature (T) or compositional (X) ranges.

A summary of the P, T and X range covered by the calibration dataset of each of the 9 models evaluated, as well as available tools to perform calculations, is provided in Figure 1. The calibration dataset of each model is shown on a total alkali-silica diagram in Figure 2. Detailed descriptions of each model are provided below.

Publication	Volatile	Speciation	P (bar)	T (°C)	Notes
Moore et al., 1998	H ₂ O	N/A	0–3000 ¹	700–1200 ¹	¹ Author-suggested calibration range. The calibration dataset spans 190 to 6067 bar, and 800–1200°C
Newman and Lowenstern (2002) VolatileCalc–Basalt	H ₂ O CO ₂	H ₂ O as OH ⁻ and H ₂ O _{mol} CO ₂ as CO ₃ ²⁻	0–5000 ¹ 0–2000 ² 0–1000 ³	600–1500 ¹ 1200 ⁴	¹ Warnings implemented in VolatileCalc (Newman and Lowenstern, 2002). ² Calibration range suggested by Lesne et al. (2011) ³ Calibration range suggested by Iacono–Marziano et al. (2012) ⁴ Calibration temperature of Dixon (1997) *if normalized (not recommended), different proportions of FeO and Fe ₂ O ₃ will slightly change the normalized SiO ₂ content
Newman and Lowenstern (2002) VolatileCalc–Rhyolite	H ₂ O CO ₂	H ₂ O as OH ⁻ and H ₂ O _{mol}	0–5000 ¹	600–1500 ¹	¹ Calibration range warning implemented in VolatileCalc (Newman and Lowenstern, 2002).
Liu et al. 2005	H ₂ O CO ₂	N/A	0–5000 ¹	700–1200 ¹	¹ Author-suggested calibration range for the mixed fluid model. The calibration dataset covers 750–5510 bar and 800–1150°C for the carbon model, and 1–5000 bar and 700–1200°C for the water model
Papale et al. (2006)	H ₂ O CO ₂	N/A	0–10,000 ¹	~630–1630 ¹	¹ Interception of H ₂ O–CO ₂ fields on Fig. 10 of Papale (1999)
Iacono–Marziano et al., 2012	H ₂ O CO ₂	N/A	100–10000 (mostly <5000) ¹	1100–1400 (preferably 1200–1300) ²	¹ Range of calibration dataset, as authors do not state a preferred range. We note that the vast majority of experiments were conducted at <5000 bar. ² Authors state that most experiments were conducted between 1200–1300°C (whole range 1100–1400°C).
	H ₂ O		163–6067 ¹	1000–1250 ¹	
Shishkina et al. 2014	H ₂ O ¹ CO ₂ ¹	N/A	0–5000 ² 500–5000 ²	1050–1400 (preferably 1150–1250) ^{2,3} 1200–1250 ^{2,3}	¹ Although their empirical expressions are for pure fluids, they were mostly calibrated on mixed CO ₂ –H ₂ O experiments. ² Author-suggested range ³ Note, this model contains no temperature term.
Magmasat (Ghiorso and Gualda, 2015)	H ₂ O CO ₂ H ₂ O–CO ₂	H ₂ O: as OH ⁻ CO ₂ : as CaCO ₃ and CO _{2mol}	0–20,000 ¹ 0–30,000 ¹ 0–10,000 ¹	550–1420 ¹ 1139–1400 ¹ 800–1400 ¹	¹ Ranges extracted from Fig. 2d of Ghiorso and Gualda, 2015
Allison et al., 2019	CO ₂ ¹	N/A	0–7000 ²	1200 ³ (~1000–1400)	¹ Although this model is for pure CO ₂ , it was calibrated on mixed CO ₂ –H ₂ O experiments. ² Author-suggested range. The calibration dataset spans: (SFVF:4133–6141 bar, Sunset Crater: 4071–6098 bar, Erebus: 4078–6175 bar, Vesuvius: 269–6175 bar, Etina=485–6199 bar, Stromboli=524–6080 bar). ³ Note, all calculations and experiments were performed at 1200°C. Authors suggest applicable between 1000–1400°C

Continued over page...

Publication	Compositional range	Formulation	Redox sensitive?	Available Tools
Moore et al., 1998	Broad compositional range: subalkaline basalts to rhyolites, alkaline trachybasalts–andesites, foidites, phonolites	Thermodynamic basis, empirical effect of melt composition	No (input FeO _T)	<ul style="list-style-type: none"> Macro-enabled Excel spreadsheet supplied by authors Python3 code (VESICAL; Iacovino et al. 2021)
Newman and Lowenstern (2002) VolatileCalc–Basalt	Alkali basalts: 40–49 wt% SiO ₂	Thermodynamic basis, empirical effect of melt composition	No (input SiO ₂ only)*	<ul style="list-style-type: none"> Macro-enabled Excel spreadsheet (VolatileCalc; Newman and Lowenstern, 2002) Python2 code (Rasmussen et al. 2020) Python3 code and web application (VESICAL; Iacovino et al. 2021)
Newman and Lowenstern (2002) VolatileCalc–Rhyolite	Rhyolites	Thermodynamic basis, no compositional term	No	<ul style="list-style-type: none"> Macro-enabled Excel spreadsheet (VolatileCalc; Newman and Lowenstern, 2002)
Liu et al. 2005	Haplogranites and rhyolites	Empirical basis, no compositional term	No	<ul style="list-style-type: none"> Python3 code (VESICAL; Iacovino et al. 2021)
Papale et al. (2006)	Broad compositional range (SiO ₂ =37–85, Na ₂ O+K ₂ O=0–20) for H ₂ O, more limited for CO ₂ and CO ₂ –H ₂ O liquids. Poor coverage of intermediate compositions (SiO ₂ =55–75 wt%).	Fully thermodynamic (formulation + effect of melt composition)	Yes (input FeO and Fe ₂ O ₃)	<ul style="list-style-type: none"> Web application, Linux application, and Fortran source code (SOLWCAD, hosted at http://www.pi.ingv.it/progetti/eurovolc/)
Iacono–Marziano et al., 2012	Predominantly mafic compositions: subalkaline and alkaline basalts–andesites	Thermodynamic basis, empirical effect of melt composition	No (input FeO _T)	<ul style="list-style-type: none"> Web application (http://calcul-isto.cnrs-orleans.fr/apbs/h2o-co2-systems/) Python3 code (VESICAL; Iacovino et al. 2021)
Shishkina et al. 2014	H ₂ O: Mafic and intermediate compositions: Subalkaline basalts–basaltic andesites, alkali basanites–phonolites. SiO ₂ >65 wt%. CO ₂ : Predominantly mafic compositions: subalkaline basalts, alkaline basanites, trachybasalts	Fully empirical (formulation+ effect of melt composition)	Only for CO ₂ (π* uses Fe ²⁺). Calibrated with Fe=Fe ²⁺	<ul style="list-style-type: none"> Python3 code (VESICAL; Iacovino et al. 2021), which uses Fe=Fe²⁺
Magmasat (Ghiorso and Gualda, 2015)	Very broad compositional range of natural silicate melt compositions: subalkaline picrobasalts–rhyolites, wide variety of mafic–silicic alkaline compositions	Fully thermodynamic (formulation + effect of melt composition)	Yes (input FeO and Fe ₂ O ₃)	<ul style="list-style-type: none"> Web application (http://melts.ofm-research.org/CORBA_CTserver/GG-H2O-CO2.html) Mac App Store (MagmaSat) Python3 code (VESICAL; Iacovino et al. 2021)
Allison et al., 2019	Alkali–rich mafic magmas from 6 volcanic fields (San Francisco Volcanic Field, Sunset Crater, Erebus, Vesuvius, Etna, Stromboli). Separate model coefficients for each composition.	Thermodynamic basis, separate parameters for each of 6 melt compositions.	No	<ul style="list-style-type: none"> Excel spreadsheet supplied by authors Python3 code (VESICAL; Iacovino et al. 2021)

Figure 1. Summary of the calibration range of each model, as well as available tools to perform calculations. Models are colored using the same palette used for comparison figures.

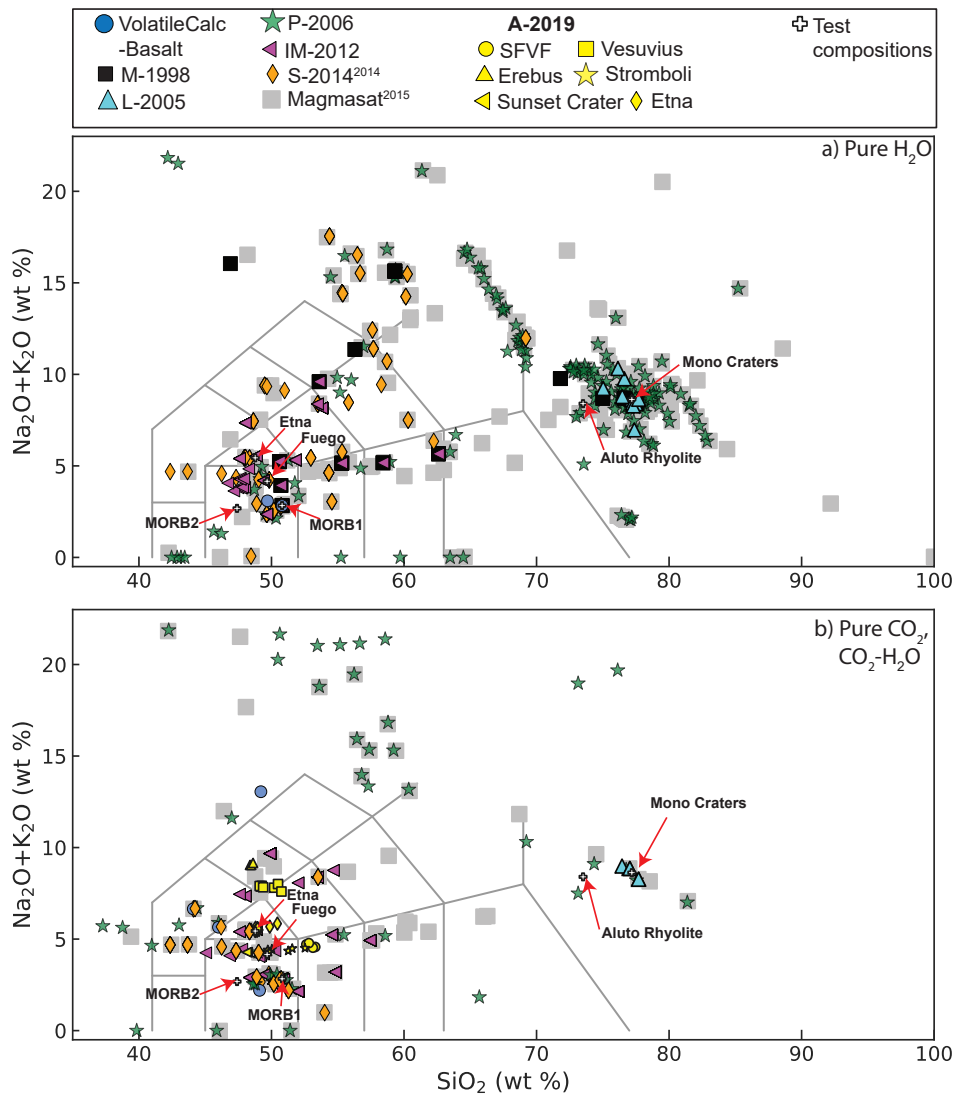


Figure 2. Total alkalis (Na₂O+K₂O) vs. SiO₂ (TAS) diagram showing the composition of melts in the calibration dataset of each model for a) pure H₂O and b) pure CO₂ and mixed CO₂-H₂O. Pure CO₂ and CO₂-H₂O experiments are combined because pure CO₂ experiments are often contaminated by variable amounts of H₂O due to exposure with the earth's atmosphere, and the high mobility of H⁺ through experimental apparatus (Mangan et al., 2021). As dissolved H₂O contents in glasses from pure CO₂ experiments are rarely reported, it is nontrivial to distinguish these from a mixed H₂O-CO₂ experiment. For P-2006 and MagmaSat, points were extracted from the TAS diagrams shown in these papers using Web Plot Digitizer (Rohatgi, 2017). For the other models, the calibration dataset is provided in the supplementary information of Iacovino et al. (2021). TAS plot drawn using Python code from Stevenson (2015).

273 **3.1 VolatileCalc-Basalt: a simplification of Dixon (1997)**

274 The Dixon (1997) model calculates the solubility of H₂O and CO₂ in basaltic
 275 silicate melts, combining thermodynamic expressions as a function of pressure and
 276 temperature described in Dixon et al. (1995) with empirical parameters accounting
 277 for the effect of melt composition in terms of melt SiO₂ content from Dixon (1997).
 278 The thermodynamic expressions are originally from Fine and Stolper (1986) for car-
 279 bon, and Silver and Stolper (1989) for water. The Dixon (1997) model considers the
 280 solubility of the carbonate ion (CO₃²⁻) for CO₂, and both molecular water (H₂O_{mol})
 281 and hydroxyl groups (OH⁻) for H₂O.

The solubility of molecular H₂O is calculated using an adapted version of equa-
 tion 3 of Dixon et al. (1995). In the original 1995 equation the X_{H₂O_{mol}}^m(P₀, T₀)
 term representing the mole fraction of molecular H₂O in equilibrium with fluid with
 a fugacity of water specified by $f_{H_2O}(P_0, T_0)$ at 1473.15 K and 1 bar was fixed at
 3.28×10^{-5} . To account for the effect of melt composition on H₂O solubility, Dixon
 (1997) parametrize this term as a function of melt SiO₂ content:

$$X_{H_2O_{mol}}^m(P_0, T_0) = 3.04 \times 10^{-5} + 1.29 \times 10^{-6} [SiO_2]^{wt\%} \quad (1)$$

282 This relationship was derived from experimental observations of Cocheo and
 283 Holloway (1993), and predicts that there is a ~30% increase in the solubility of H₂O
 284 with increasing SiO₂ between nephelinite (~40 wt% SiO₂) and tholeiite (~49 wt%
 285 SiO₂) melt compositions. The concentration of OH⁻ is then calculated as a function
 286 of the mole fraction of molecular H₂O in the melt using the solution model of Silver
 287 and Stolper (1989) (see equation 4 of Dixon, 1997). Interestingly, this is the only
 288 model discussed here which considers more than one species for dissolved H₂O in the
 289 melt.

For CO₂ solubility, Dixon (1997) adapted the model of Dixon et al. (1995) to
 account for the effect of melt composition, based on observations from experiments
 that CO₂ solubility increases from tholeiitic (49 wt% SiO₂) to basaltic (46 wt%
 SiO₂) to leucitic (44.1 wt% SiO₂) melts at 1200°C, 1 kbar. A linear regression with
 CO₂ solubility was achieved using a composition parameter (II) expressed in terms

of the cation fractions, X_i (Dixon, 1997):

$$\Pi = -6.50(X_{\text{Si}^{4+}} + X_{\text{Al}^{3+}}) + 20.17(X_{\text{Ca}^{2+}} + 0.8X_{\text{K}^+} + 0.7X_{\text{Na}^+} + 0.4X_{\text{Mg}^{2+}} + 0.4X_{\text{Fe}^{2+}}) \quad (2)$$

However, based on the strong correlation between Π and SiO_2 in a suite of lavas from the North Arch Volcanic Field, Dixon (1997) express the $X_{\text{CO}_3^{2-}}^m(P_0, T_0)$ term from equation 6 of Dixon et al. (1995) solely as a function of melt SiO_2 content:

$$X_{\text{CO}_3^{2-}}^m(P_0, T_0) = 8.70 \times 10^{-6} - 1.70 \times 10^{-7}[\text{SiO}_2]^{\text{wt}\%} \quad (3)$$

290 Where $X_{\text{CO}_3^{2-}}^m(P_0, T_0)$ is the mole fraction of carbonate in equilibrium with fluid
 291 with a fugacity of carbon dioxide specified by $f_{\text{CO}_2}(P_0, T_0)$ at 1473.15 K and 1 bar.
 292 Fugacities are calculated using the Redlich-Kwong equation of state (Holloway,
 293 1977), with the correction of Flowers (1979).

294 This simplified expression was designed to aid the investigations of volatile
 295 solubility in the suite of lavas from the North Arch, where it effectively captures
 296 the observed $5\times$ decrease in CO_2 solubility from 40 to 49 wt% SiO_2 . However, this
 297 simplified parameterization became very widely used in a wide variety of tectonic
 298 settings following its implementation in the Excel-based tool VolatileCalc (New-
 299 man and Lowenstern, 2002). Here, we refer to this model as VolatileCalc-Basalt, to
 300 differentiate it from the full Π parameterization of Dixon (1997).

301 The advantage of the Π - SiO_2 simplification is that users only have to input the
 302 concentration of one oxide component (melt SiO_2) in addition to melt temperature
 303 and melt volatile contents to calculate saturation pressures or degassing paths. The
 304 limited number of inputs required by this model meant that users can calculate sat-
 305 uration pressures for large numbers of melt inclusions relatively quickly compared
 306 to more recent models such as Iacono-Marziano et al. (2012) and MagmaSat (which
 307 require users to input 8–14 oxide concentrations).

308 However, extreme care must be taken when using this simplified model to
 309 calculate CO_2 solubility. Firstly, the North Arch lavas span SiO_2 contents of only
 310 40–49 wt%. Because of the rapid drop in Π with increasing SiO_2 , extrapolation
 311 beyond 51.2 wt% SiO_2 yields a negative value for $X_{\text{CO}_3^{2-}}^m(P_0, T_0)$, corresponding
 312 to a negative amount of dissolved CO_2 . To avoid this issue, VolatileCalc-Basalt re-
 313 turns an error, and will not perform the calculation if users enter a SiO_2 content

314 >49 wt%. Most studies extrapolate beyond this by simply entering $\text{SiO}_2=49$ wt%
315 into VolatileCalc-Basalt if their melts have higher silica contents (e.g. Sides et al.,
316 2014a, 2014b; Tucker et al., 2019), and this approach is implemented in VESIcal for
317 consistency. Newman and Lowenstern (2002) suggest that this extrapolation will be
318 “generally applicable for other basaltic rocks with <52 wt% SiO_2 ”. However, if a
319 large proportion of a sample suite has SiO_2 contents with >49 wt% SiO_2 , the simpli-
320 fied II- SiO_2 parameterization treats all melts as if they have the same composition,
321 neglecting variations in solubility that may exist within that suite (see Wieser et al.,
322 2021). Additionally, even if samples have SiO_2 contents between 40–49 wt%, this
323 simplification can yield spurious results for melts which do not follow the same trend
324 in II- SiO_2 space to the North Arch lavas (see section 4.2.3). Thus, we suggest that
325 any users wishing to apply VolatileCalc-Basalt to their system first check whether
326 their melt compositions lie close to the trend defined by the North Arch lavas using
327 the Jupyter notebook provided in the supplementary information of Iacovino et al.
328 (2021).

329 It is also worth noting that, because VolatileCalc-Basalt parameterizes the
330 effect of melt composition in terms of the absolute concentration of SiO_2 (rather
331 than other empirical models which use cation fractions), it is extremely sensitive to
332 normalization. For example, consider the MORB2 composition in Table 1 which has
333 a measured SiO_2 content of 47.4 wt%, and an anhydrous total of 97.375 wt%. For
334 1000 ppm CO_2 and $T=1200^\circ\text{C}$, using raw data ($\text{SiO}_2=47.4$ wt%) the calculated sat-
335 uration pressure is 1206 bars. However, it is relatively common in the literature that
336 major elements (excluding volatiles) are scaled to sum to 100%, while volatile con-
337 centrations are left unchanged. This would cause the melt SiO_2 content to increase
338 to 48.68 wt% SiO_2 , corresponding to a saturation pressure of 1765 bar respectively
339 ($1.5\times$ higher!). We encourage users not to normalize their data, as we note that the
340 II- SiO_2 plot of North Arch Glasses in Dixon (1997) is best recreated using unnor-
341 malized data (see Supporting Fig. S1). Unnormalized data is used throughout this
342 review for all VolatileCalc-Basalt outputs, which gives results comparable to those
343 produced in the VolatileCalc-Basalt spreadsheet when users enter the SiO_2 contents
344 given in Table 1.

3.2 VolatileCalc-Rhyolite: Newman and Lowenstern, 2002

In addition to the functionality for basalts described above, the VolatileCalc spreadsheet also allows users to calculate saturation pressures, degassing paths, isobars and isopleths for rhyolitic magmas (hereafter, VolatileCalc-Rhyolite). For CO₂, VolatileCalc-Rhyolite uses the simple thermodynamic model from Stolper et al. (1987) that was later applied to rhyolitic melts by Fogel and Rutherford (1990). The molar enthalpy change for CO₂ dissolution in the melt is from Fogel and Rutherford (1990), the single-O melt mass from Silver et al. (1990), and the CO₂ molar volume and solubility at standard state from Blank et al. (1993). The thermodynamic basis for the H₂O model is the same as that used in VolatileCalc-Basalt. The fitted parameters for H₂O solubility in the standard state is from Silver (1988), and the single-O melt mass and molar enthalpy change for H₂O dissolution in the melt from Silver et al. (1990). The partial molar volume of H₂O was adjusted to 5 cm³/mol to provide a better fit to experimental data. There are two main differences of the rhyolite model relative to the basaltic model. First, while both the models use a temperature-dependent equation of state, VolatileCalc-Rhyolite model also contains a term for the heat of solution of volatile solubility, so is far more sensitive to temperature (see section 5). Second, unlike VolatileCalc-Basalt which require users to enter melt SiO₂ contents, VolatileCalc-Rhyolite is independent of melt composition. Thus, Newman and Lowenstern (2002) caution that this model may not be applicable for strongly peralkaline or peraluminous rhyolites.

3.3 M-1998 (Moore et al., 1998)

The Moore et al. (1998) model calculates the solubility of H₂O for a wide range of silicate melt compositions using an empirical expression valid between 700–1200°C and 0–3000 bars:

$$2 \ln(X_{\text{H}_2\text{O}}^{\text{melt}}) = \frac{a}{T} + \sum_i b_i X_i \frac{P}{T} + c \ln(f_{\text{H}_2\text{O}}^{\text{fluid}}) + d \quad (4)$$

Where $X_{\text{H}_2\text{O}}^{\text{melt}}$ is the mole fraction of H₂O dissolved in the melt, T is the temperature in Kelvin, P is the pressure in bars, and X_i is the anhydrous molar fraction of each oxide component. $f_{\text{H}_2\text{O}}^{\text{fluid}}$ is the fugacity of H₂O in the fluid, calculated using the modified version of the Redlich-Kwong equation of state provided in the ap-

pendix of Holloway and Blank (1994). Equation 4 is associated with the following fit parameters (\pm standard error):

Coefficient	a	$b_{Al_2O_3}$	b_{FeO_r}	b_{Na_2O}	c	d
Value ($\pm 1\sigma$)	2565 (± 362)	-1.997 (± 0.706)	-0.9275 (± 0.394)	2.736 (± 0.871)	1.171 (± 0.069)	-14.21 (± 0.54)

As equation 4 includes a term for the fugacity of H₂O in the fluid, this model can be integrated with CO₂ models implemented in VESICAL (e.g., the II-SiO₂ simplification of Dixon, 1997, Liu et al., 2005, Iacono-Marziano et al., 2012, Shishkina et al., 2014, Allison et al., 2019) to investigate mixed H₂O-CO₂ fluids.

The model calibration dataset combines the authors' pure H₂O experiments with literature data, spanning sub-alkaline basaltic to rhyolitic compositions, as well as some alkaline compositions (Fig. 2). As with other fully-empirical models implemented in VESICAL, or those including empirical expressions, extreme care must be taken when extrapolating this model outside of the calibration range. In particular, the authors warn against extrapolating this model to pressures exceeding 3 kbar, in part due to the complexities of the critical behavior of fluids at higher pressures.

3.4 L-2005 (Liu et al., 2005)

The Liu et al. (2005) model calculates the solubility of H₂O and CO₂ in metaluminous, high-silica rhyolitic melts using empirical expressions, valid between 700–1200°C, and 0–5000 bars. The following expression is used to calculate CO₂ solubility:

$$[CO_2]^{ppm} = \frac{P_{CO_2}(b_1 + b_4 P_W)}{T} + P_{CO_2}(b_2 P_W^{0.5} + b_3 P_W^{1.5}) \quad (5)$$

T is temperature in Kelvin, b_1 – b_4 are fit parameters, and the P_W and P_{CO_2} terms account for the partial pressures of each volatile species in the co-existing fluid, with:

$$P_{CO_2} = X_{CO_2}^f P \quad (6)$$

$$P_W = X_W^f P \quad (7)$$

Where P is pressure in MPa, $X_{CO_2}^f$ is the mole fraction of CO₂ in the fluid, and X_W^f is the mole fraction of H₂O in the fluid. These empirical terms mean that no equation of state is used (unlike M-1998 and VolatileCalc-Basalt). The fit parameters associated with equation 5 are shown below (\pm error):

Coefficient	b_1	b_2	b_3	b_4
Value (Error)	5668 (± 127)	0.4133 (± 0.0491)	2.041×10^{-3} ($\pm 0.285 \times 10^{-3}$)	-55.99 (± 8.36)

390

Similarly, they provide the following expression for H₂O:

$$[\text{H}_2\text{O}_t]_{\text{wt}\%} = \frac{a_1 P_w^{0.5} + a_2 P_w + a_3 P_w^{1.5}}{T} + a_4 P_w^{1.5} + P_{\text{CO}_2} (a_5 P_w^{0.5} + a_6 P_w) \quad (8)$$

391

Using the following fit parameters:

Coefficient	a_1	a_2	a_3	a_4
Value (Error)	354.94 (± 4.55)	9.623 (± 0.923)	-1.5223 (± 0.0722)	0.0012439 (± 0.0000499)
	a_5		a_6	
	-1.084 $\times 10^{-4}$ ($\pm 0.406 \times 10^{-4}$)		-1.362 $\times 10^{-5}$ ($\pm 0.352 \times 10^{-5}$)	

392

The model calibration dataset combines pure H₂O solubility experiments by the authors between ~ 1 and 250 bars with literature experiments investigating the solubility of pure H₂O, H₂O-H₂, CO₂ and CO₂-H₂O fluids, spanning significantly higher pressures (up to 5000 bars). Unlike the M-1998 model, their empirical expressions do not incorporate a term for melt composition, so care is needed when applying this model to melts with different major element compositions to the calibration dataset (Fig. 2).

399

3.5 P-2006 (Papale et al., 2006)

400

Papale et al. (2006) present a fully non-ideal thermodynamic model for H₂O and CO₂ solubility, which is a recalibration of the earlier models of Papale (1999) and Papale (1997). This updated model capitalizes on the large amount of volatile solubility experiments performed between 1997 and 2005, which nearly doubled the size of the calibration dataset, and allowed experimental data on CO₂ solubility collected prior to 1980 to be discarded (removing systematic errors associated with different analytical techniques, see Papale, 1999). Unlike the models discussed above which are calibrated on a specific subregion of compositional space and use empirical parametrizations to account for the effect of melt composition, the models of Papale et al. (2006) and Papale (1999) treat the composition of the silicate liquid using a thermodynamic approach based on Ghiorso et al. (1983). Papale et al. (2006) note that this thermodynamic approach means that for any specific region of composition space (e.g., comparing model results to a specific experiment), the fit may not be as good as an empirical model tuned to that composition. However, carefully calibrated

414

415 thermodynamic models will be significantly more successful than empirical models
 416 when applied to melts which are not represented in the calibration dataset.

P-2006 considers a silicate liquid in mechanical, thermal and chemical equilibrium with a fluid phase containing H₂O and CO₂. The model uses the modified Redlich-Kwong equation of state of Kerrick and Jacobs (1981) to describe the fluid phase, and considers only the dissolution of CO₂ and H₂O in the melt (while natural silicate melts contain molecular CO₂ and CO₃²⁻ species, and molecular H₂O and OH⁻ species). The model calculates the Gibbs free energy of mixing, considering 10 major oxide components in addition to CO₂ and H₂O. Binary interaction coefficients, denoted by w_{ij} , account for the attractive-repulsive behaviour between an oxide and volatile component. For example, $w_{CO_2, MgO}$ describes the interaction of MgO with CO₂. Interaction coefficients for CO₂ are expressed as a function of pressure (relative to a reference pressure of 0.1 MPa) requiring two coefficients, while those for H₂O are invariant of pressure (requiring 1 coefficient):

$$w_{CO_2,i} = w_{CO_2,i}^0 + w_{CO_2,i}^1 \ln \frac{P}{P_0} \quad (9)$$

$$w_{H_2O,i} = w_{H_2O,i}^0 \quad (10)$$

417 P-2006 uses interaction terms for SiO₂, Al₂O₃, MgO, CaO, Na₂O, K₂O, FeO and
 418 Fe₂O₃. The presence of two Fe terms means that the model is sensitive to melt re-
 419 dox. Papale et al. (2006) show that the inclusion of w terms for MnO and TiO₂ lead
 420 to overfitting, so the effect of these oxides on model outputs is only through the di-
 421 lution of the concentration of components allocated w terms. The values of the 24 w
 422 terms, as well as 5 terms accounting for molar volumes and fugacities, are calculated
 423 from a calibration dataset comprising \sim 1100 solubility experiments with pure CO₂,
 424 pure H₂O and mixed CO₂-H₂O fluids. While the calibration dataset contains well
 425 populated clusters for basaltic and rhyolitic compositions, intermediate compositions
 426 and basaltic melts with high alkali contents are poorly represented, particularly for
 427 CO₂ (Fig. 2).

428 Papale et al. (2006) demonstrate that despite the addition of hundreds of new
 429 experimental datapoints for H₂O, there are no significant changes in coefficients
 430 compared to those which were published with their 1999 model. The percent errors
 431 on the H₂O coefficients in the 2006 model are $< 10\%$ for all species (defined as $100^* \sigma / \text{coefficient}$).
 432 In contrast, the addition of new CO₂ data to the calibration dataset

433 resulted in significant changes in coefficients, and the percentage errors on these
 434 coefficients in the 2006 model remained large ($\sim 800\%$ for FeO, $\sim 150\%$ for Na₂O,
 435 $\sim 190\%$ for MgO, Fig. 3). Based on these large error values, these coefficients would
 436 likely change again if this model was recalibrated to include all new CO₂ experi-
 437 ments published since 2006.

438 The pressure-dependence of the CO₂ melt interaction terms, combined with
 439 the fact that the w_o and w_1 terms have different signs for all oxides except FeO,
 440 means that a given change in melt chemistry may cause an increase in CO₂ solu-
 441 bility at one pressure, but a decrease at another pressure (see Section 4.1). Ghiorso
 442 and Gualda (2015) note that the coefficient for the compressibility of CO₂ in the
 443 P-2006 model is negative, which is physically impossible (implying the volume of the
 444 CO₂ fluid increases when pressure is increased), which they suggest may arise from
 445 the inclusion of pressure-dependent w -terms.

P-2006

Element	CO ₂				H ₂ O	
	w_o	% error (1 σ)	w_1	% error	w_o	% error
SiO ₂	-59,962	18	6049	19	-34,093	1.85
Al ₂ O ₃	-590,957	32	41,395	47	-189,117	2.54
Fe ₂ O ₃	4,469,623	9	-529,301	9	135,935	9.32
FeO	21,666	806	1214	1500	-195,751	3.13
MgO	52,866	189	-13,446	78	-86,418	7.06
CaO	-328,792	23	12,789	63	-209,997	1.67
Na ₂ O	140,034	146	-35,213	60	-322,253	1.42
K ₂ O	309,070	48	-58,010	27	-349,798	1.79

MagmaSat

Element	CO ₂ -CO ₃ ²⁻				H ₂ O	
	W (CO ₂)	% error (1 σ)	W (CaCO ₃)	% error	W	% error
SiO ₂			63.281	2.52	27.557	0.065
TiO ₂	-19.266	1.34	-79.203	0.46	88.199	2.87
Al ₂ O ₃			46.716	2.52	11.768	21.8
Fe ₂ O ₃	-3.187	4.3	65.509	0.26	50.105	17.0
Fe ₂ SiO ₄	-32.465	0.95	-72.997	0.40	30.936	18.8
Mg ₂ SiO ₄	-40.854	1.6	-24.873	4.17	20.910	21.5
CaSiO ₃	30.012	4.8	37.534	2.70	9.715	27.5
Na ₂ SiO ₃			-311.011	0.24	-82.460	2.9
KAlSiO ₄			-27.865	8.21	1.057	112
Ca ₃ (PO ₄) ₂	-3.473	0.86	2.012	2.49	44.133	0.76

Figure 3. Interaction coefficients for P-2006 and MagmaSat. Percentage errors calculated as $100 \times 1\sigma / \text{coefficient}$. Error are colored green if they are $< 10\%$, light pink if $10\text{--}25\%$, and red if $> 25\%$.

446

3.6 IM-2012 (Iacono-Marziano et al. 2012)

The Iacono-Marziano et al. (2012) model expresses the solubility of H₂O and CO₂ in mafic melts by combining simplified thermodynamic expressions for melt-fluid thermodynamics with empirical formulations accounting for melt composition. For CO₂, they present the following expression:

447

448

$$\ln[\text{CO}_2]^{\text{ppm}} = X_{\text{H}_2\text{O}}d_{\text{H}_2\text{O}} + X_{\text{Al}}d_{\text{Al}} + X_{\text{FeO}+\text{MgO}}d_{\text{FeO}+\text{MgO}} + X_{\text{Na}_2\text{O}+\text{K}_2\text{O}}d_{\text{Na}_2\text{O}+\text{K}_2\text{O}} + a_{\text{CO}_2}\ln[\text{P}_{\text{CO}_2}] + b_{\text{CO}_2}\left[\frac{\text{NBO}}{\text{O}}\right] + B_{\text{CO}_2} + C_{\text{CO}_2}\frac{\text{P}}{\text{T}} \quad (11)$$

Where P is the pressure in bars, T is the temperature in Kelvin, X_{H₂O} is the molar fraction of H₂O in the melt and P_{CO₂} is the partial pressure of CO₂ in bars. The partial pressure of CO₂ is calculated from the pressure multiplied by the mole fraction of CO₂ in the fluid. This means that this model does not rely on an equation of state (as with the L-2005 model). The other terms account for the effect of melt composition using molar fractions calculated on a hydrous basis; X_{FeO+MgO} is the sum of molar fractions of FeO_t and MgO, X_{Na₂O+K₂O} is the sum of the molar fractions of Na₂O and K₂O, and X_{AI} is the aluminic index (AI):

$$X_{\text{AI}} = \frac{X_{\text{Al}_2\text{O}_3}}{X_{\text{CaO}} + X_{\text{K}_2\text{O}} + X_{\text{Na}_2\text{O}}} \quad (12)$$

The NBO/O term represents the number of non-bridging oxygens divided by oxygen, expressing the availability of oxygen to form carbonate groups within the melt. NBO/O can be calculated from mol fraction of different oxides, X_i, on an anhydrous or hydrous basis:

$$\frac{\text{NBO}}{\text{O}}^{\text{Anhyd}} = \frac{2(X_{\text{K}_2\text{O}} + X_{\text{Na}_2\text{O}} + X_{\text{CaO}} + X_{\text{MgO}} + X_{\text{FeO}} - X_{\text{Al}_2\text{O}_3})}{2X_{\text{SiO}_2} + 2X_{\text{TiO}_2} + 3X_{\text{Al}_2\text{O}_3} + X_{\text{MgO}} + X_{\text{FeO}} + X_{\text{CaO}} + X_{\text{Na}_2\text{O}} + X_{\text{K}_2\text{O}}} \quad (13)$$

$$\frac{\text{NBO}}{\text{O}}^{\text{Hyd}} = \frac{2(X_{\text{H}_2\text{O}} + X_{\text{K}_2\text{O}} + X_{\text{Na}_2\text{O}} + X_{\text{CaO}} + X_{\text{MgO}} + X_{\text{FeO}} - X_{\text{Al}_2\text{O}_3})}{2X_{\text{SiO}_2} + 2X_{\text{TiO}_2} + 3X_{\text{Al}_2\text{O}_3} + X_{\text{MgO}} + X_{\text{FeO}} + X_{\text{CaO}} + X_{\text{Na}_2\text{O}} + X_{\text{K}_2\text{O}} + X_{\text{H}_2\text{O}}} \quad (14)$$

449

450

451

452

In both cases, mole fractions are calculated on a hydrous basis (Iacono-Marziano, written comms). Iacono-Marziano give coefficients for equation 11 for both cases ($\pm 2\sigma$), leading to two forms of this model: IM-2012-A (anhydrous) and IM-2012-H (hydrous):

Coefficient	d _{H₂O}	d _{AI}	d _{FeO+MgO}	d _{Na₂O+K₂O}	a _{CO₂}	b _{CO₂}	c _{CO₂}	B _{CO₂}
Hydrous (±error)	-16.4 (± 1.2)	4.4 (±0.4)	-17.1 (± 0.9)	22.8 (± 1.1)	1 (± 0.03)	17.3 (± 0.9)	0.12 (±0.02)	-6 (±0.4)
Anhydrous (±error)	2.3 (± 0.5)	3.8 (±0.4)	-16.3 (± 0.9)	20.1 (± 1.1)	1 (± 0.03)	15.8 (± 0.9)	0.14 (±0.02)	-5.3 (±0.4)

453

454 We note for completeness that in the original publication, equation 11 was
 455 incorrectly expressed in terms of $\ln[\text{CO}_3^{2-}]$ (Iacono-Marziano, written. comms).

456 For H_2O , the authors state that it is statistically unjustified to include d_i
 457 terms similar to those in the CO_2 expression, due to the relatively small effect of
 458 melt composition on H_2O solubility. The effect of melt composition is incorporated
 459 only through the NBO/O term:

$$\ln [\text{H}_2\text{O}]^{\text{wt}\%} = a_{\text{H}_2\text{O}} \ln[\text{P}_{\text{H}_2\text{O}}] + b_{\text{H}_2\text{O}} \left[\frac{\text{NBO}}{\text{O}} \right] + B_{\text{H}_2\text{O}} + C_{\text{H}_2\text{O}} \frac{\text{P}}{\text{T}} \quad (15)$$

460 Where $\text{P}_{\text{H}_2\text{O}}$ is the partial pressure of H_2O in bars. As for CO_2 , coefficients are
 461 provided for NBO/O calculated on a hydrous and anhydrous basis. The hydrous co-
 462 efficients in the published paper differ from those used in the web app over the last
 463 decade (although a new web app using the published coefficients appeared briefly in
 464 2021). VESICAL uses the web app hydrous coefficients by default, as recommended
 465 by Iacono-Marziano (written. comms). The coefficients in the published paper were
 466 from an older version of the model, and predict extremely high H_2O solubility at
 467 ~ 10 kbar (>100 wt%).

Coefficient	$a_{\text{H}_2\text{O}}$	$b_{\text{H}_2\text{O}}$	$B_{\text{H}_2\text{O}}$	$C_{\text{H}_2\text{O}}$
Hydrous (\pmerror)	0.53 (\pm 0.02)	2.35 (\pm 0.28)	-3.37 (\pm 0.13)	-0.02 (\pm 0.02)
Anhydrous (\pmerror)	0.54 (\pm 0.02)	1.24 (\pm 0.28)	-2.95 (\pm 0.17)	0.02 (\pm 0.02)
Web App	0.52096846	2.11575907	-3.24443335	0.02238884

469 The authors state that the differences between calculations performed with
 470 NBO/O calculated on a hydrous and anhydrous basis are relatively small, but that a
 471 slightly better fit to experimental data is obtained using the hydrous model (particu-
 472 larly for H_2O -rich, and CO_2 -poor melts). For completeness, we perform calculations
 473 using both versions (referred to as IM-2012-H and IM-2012-A). Interestingly, we
 474 show that the anhydrous version is most similar to other models for MORB-like
 475 compositions.

476 The calibration dataset for CO_2 combines the authors experiments with those
 477 from a variety of literature studies for mixed H_2O - CO_2 fluids, spanning tempera-
 478 tures between 1100 and 1400°C, and pressures between 100 and 10,000 bars (but
 479 mostly <5000 bars). The calibration dataset for H_2O incorporates pure H_2O exper-
 480 iments from the literature (spanning 163–6067 bars, and 1000–1250°C), as well as

481 the experiments on H₂O-CO₂ fluids used to calibrate the CO₂ expression. Melt com-
 482 positions are predominantly mafic, spanning subalkaline-alkaline basalts to basaltic
 483 andesites (45–57 wt% SiO₂ for mixed H₂O-CO₂ experiments, and 46–63 wt% SiO₂
 484 for pure H₂O; Fig. 2).

485 The empirical nature of the fitting terms incorporating melt composition, pres-
 486 sure and temperature means that users should be cautious when extrapolating this
 487 model to conditions lying outside the P-T-X range of the calibration dataset. In
 488 particular, Iacono-Marziano et al. (2012) highlight five weaknesses of their model:

- 489 1. The effect of melt MgO and FeO contents on CO₂ solubility is poorly con-
 490 strained, because of the small variation in the concentrations of these oxides
 491 in the calibration database.
- 492 2. While their compositional terms for the effect of melt composition on CO₂
 493 solubility gives equal weight to Na₂O and K₂O, the calibration dataset only
 494 includes K₂O-rich melts with a range of pressures, so the effect of substituting
 495 Na and K is poorly constrained.
- 496 3. The effect of temperature on the solubility of mixed H₂O-CO₂ is poorly con-
 497 strained because the majority of experiments in the calibration dataset were
 498 performed at 1200–1300°C.
- 499 4. The relative role of molecular H₂O vs. OH⁻ on melt structure, which in turn
 500 influences CO₂ solubility, needs to be evaluated further.
- 501 5. The model was calibrated assuming that all Fe was Fe²⁺, so calculated solu-
 502 bilities are not sensitive to melt redox (unlike the model of P-2006).

503 These weaknesses are explored in more detail in sections 5 and 6.

504 3.7 S-2014 (Shishkina et al., 2014)

The Shishkina et al. (2014) model calculates the solubility of H₂O and CO₂ using fully-empirical expressions. Their expression for CO₂ solubility was calibrated on a dataset of mixed H₂O-CO₂ experiments on predominantly mafic compositions between 1200–1300°C, and 500–5000 bars:

$$\ln[\text{CO}_2]^{\text{ppm}} = 1.150 \ln(P) + 6.71 \Pi^* - 1.345 \quad (16)$$

Where P is the pressure in MPa, and Π^* is a compositional parameter expressed in terms of the cation fractions of 7 species:

$$\Pi^* = \frac{X_{\text{Ca}^{2+}} + 0.8 X_{\text{K}^+} + 0.7 X_{\text{Na}^+} + 0.4 X_{\text{Mg}^{2+}} + 0.4 X_{\text{Fe}^{2+}}}{X_{\text{Si}^{4+}} + X_{\text{Al}^{3+}}} \quad (17)$$

505 We note for completeness that the expression provided in Shishkina et al. (2014)
506 incorrectly states that CO_2 in equation 16 was in wt%, rather than ppm.

Their expression for H_2O solubility was calibrated on a dataset of pure H_2O experiments with mafic to intermediate compositions between 1200–1250°C, and 485–5009 bars. It incorporates a composition parameter expressed in terms of the anhydrous cation fractions of Na and K:

$$[\text{H}_2\text{O}]^{\text{wt}\%} = (3.36 \times 10^{-7} P^3 - 2.33 \times 10^{-4} P^2 - 0.0711 P - 1.1309)(X_{\text{Na}} + X_{\text{K}}) - 1.2 \times 10^{-5} P^2 + 0.0196 P + 1.1297 \quad (18)$$

507 In general, the compositional range of the Shishkina et al. (2014) dataset includes
508 a larger variety of mafic compositions than that of Iacono-Marziano et al. (2012),
509 particularly with respect to alkali-rich, or highly depolymerized melts (Fig. 2). How-
510 ever, as was true for IM-2012, the empirical nature of the compositional term means
511 that extreme care is needed when extrapolating this model beyond the composi-
512 tional range of the calibration dataset (see section 6).

513 One caveat of the implementation of this model in VESIcal is the treatment of
514 mixing between CO_2 and H_2O . Shishkina et al. (2014) note that their experimental
515 data shows evidence for significant non-ideality, with isobars remaining almost hori-
516 zontal between 0–4 wt% H_2O (see their Fig. 6). However, the isobars shown on their
517 plots are fitted to experimental data, rather than derived from their equations for
518 CO_2 and H_2O solubility. These fits cannot be applied to melts with different com-
519 positions, and the authors give no guidance as to how to combine their equations for
520 pure CO_2 and pure H_2O to reproduce this non-ideal behaviour for any given melt
521 composition. Thus, due to an absence of other information, VESIcal treats mixing
522 between H_2O and CO_2 as ideal in this model. To emphasize this assumption, the
523 H_2O - CO_2 model called ShishkinaIdealMixing in VESIcal.

524 **3.8 MagmaSat: Ghiorso and Gualda (2015)**

525 Ghiorso and Gualda (2015) present a comprehensive thermodynamic model
526 (MagmaSat) for mixed H_2O - CO_2 solubility, calibrated on the most chemically-

527 diverse set of natural silicate melt compositions of all the models discussed thus far
528 (Fig. 2). For this reason, it is the default model in VESIcal. MagmaSat uses the
529 equation of state of Z. Duan and Zhang (2006) for the CO₂-H₂O fluid, and is the
530 volatile solubility model implemented in rhyolite-MELTS v.1.2 (Gualda et al., 2012).
531 Thus, it is currently the only model which can be directly integrated with phase
532 equilibrium calculations (e.g., to track microlite growth during degassing upon as-
533 cent, or post-entrapment modification to melt inclusions). Like P-2006, the model
534 considers the Gibbs free energy of solution using interaction parameters (denoted
535 with a capital *W* in this model), although, unlike in P-2006, these terms are in-
536 dependent of pressure (as well as temperature). The exact choice of components
537 differs from that of P-2006, as MagmaSat adapts the formulation from Rhyolite-
538 MELTS (e.g., Mg is considered as Mg₂SiO₄, Ghiorso & Sack, 1995). Unlike P-2006,
539 MagmaSat considers the dissolution of CO₂ as both molecular CO₂ and carbonate
540 species (as CaCO₃), with a set of *W* coefficients for each. MagmaSat assumes that
541 water dissolves entirely as a hydroxyl species, rather than considering both hydroxyl
542 and molecular species. This helps to reduce the number of interaction parameters
543 for volatile-melt species, and seems to be a justified simplification based on available
544 experimental data (see Ghiorso and Gualda, 2015 for a more detailed discussion).

545 The calibration dataset for H₂O spans 550–1420°C, and pressures of 0–20,000
546 bars, and for CO₂ spans 1140–1400 °C and 0–30,000 bars. However, as discussed in
547 detail later, care is required when interpreting H₂O solubility at pressures >10 kbar.
548 Importantly, unlike P-2006, MagmaSat is not calibrated for synthetic liquids (e.g.,
549 compositions only containing a small number of oxide species like albite), so should
550 only be applied to natural silicate liquid compositions.

551 **3.9 A-2019: Allison et al. (2019)**

552 Allison et al. (2019) present thermodynamic models to calculate CO₂ solubility
553 for six different basaltic compositions from Stromboli (alkali basalt), Etna (trachy-
554 basalt), Vesuvius (phonotephrite), Erebus (phonotephrite), Sunset Crater (alkali
555 basalt), and the San Francisco Volcanic Field (basaltic andesite, Fig. 2). Specifi-
556 cally, they performed experiments at 1200°C, and ~4000–6000 bars to address the
557 paucity of experiments examining CO₂ solubility in alkali systems at mid crustal
558 pressures. In addition to these experiments, their models for Vesuvius, Etna and

559 Stromboli incorporate experiments from the literature, extending the calibration
560 range of these three models to upper crustal pressures (see Fig. 1). Unlike models
561 which incorporate the effect of changing melt composition empirically (e.g., Newman
562 & Lowenstern, 2002; Iacono-Marziano et al., 2012; Shishkina et al., 2014), Allison
563 et al. (2019) determine the parameters $\Delta V_r^{0,m}$ (the molar volume change of the
564 condensed components of the reaction) and $K_0(P_0, T_0)$ (the equilibrium constant
565 at the reference pressure and temperature) within their thermodynamic equation
566 empirically for each of the six compositions they examine, and create 6 separate
567 models (each of which contains no compositional dependence). The A-2019 models
568 incorporate the modified Redlich-Kwong equation of state provided in the appendix
569 of Holloway and Blank (1994).

570 Interestingly, Allison et al. (2019) show that CO_2 solubility does not sim-
571 ply scale with total alkali contents. Erebus melts have $\text{Na}_2\text{O}+\text{K}_2\text{O}=8.8$ wt%, but
572 dissolve less CO_2 than Etna and Vesuvius melts ($\text{Na}_2\text{O}+\text{K}_2\text{O}=5.2$ and 7.8 wt% re-
573 spectively). They suggest that CaO, MgO and Al_2O_3 may play a role in the lower
574 solubility of Erebus compared to Etna, but the fact that 5 of the 7 major elements
575 they examine show notable differences between these melt compositions make it
576 difficult to conclusively determine the origin of solubility variations. Ideally, users
577 would apply the A-2019 Etna model to lavas erupted at Etna, the Stromboli model
578 to lavas erupted at Stromboli and so on. The absence of an empirical term for melt
579 composition means that extreme care should be taken when applying these equa-
580 tions to alkaline lavas with different major element contents to those used in the
581 experiments of Allison et al. (2019), even if the lavas originated from one of the 6
582 volcanoes they examine.

583 Allison et al. (2019) only present equations for CO_2 solubility, as their experi-
584 ments weren't designed to have a wide range of H_2O contents at different pressures,
585 and their high $X_{\text{CO}_2}^f$ values mean that errors in their fluid fraction measurements
586 propagate into large errors for H_2O fugacity (relative to the insignificant errors for
587 CO_2 fugacity). In their supplementary spreadsheet, they integrate their CO_2 sol-
588 ubility models with an power law fit for water solubility developed specifically for
589 Etna (Equation 2 of Lesne, Scaillet, Pichavant, Iacono-Marziano, & Beny, 2011).
590 In VESical, users can combine any of the A-2019 carbon models with H_2O models
591 from M-1998, IM-2012 and S-2014, or write their own.

4 Model Comparisons

To aid comparisons between models, we use a number of silicate melt compositions spanning a range of typical end-member compositions found in nature (Table 1, Fig. 2) to examine the relationship between volatile solubility and pressure, the treatment of mixing between H₂O and CO₂ (manifested in the shapes of isobars), as well as sensitivity to parameters such as temperature and oxygen fugacity. For basalts, we consider two mid-ocean ridge basalts (MORB1, 50.8 wt% SiO₂, (Dixon et al., 1995), MORB2, 47.4 wt% SiO₂, (Allan et al., 1989), one alkali basalt from Etna (48.8 wt% SiO₂, (Allison et al., 2019) and an arc basalt from Fuego (49.7 wt% SiO₂, (Lloyd et al., 2013). Comparisons between the MORB and Etna compositions were performed at 1200°C, while those for Fuego were performed at 1000°C to reflect the lower temperatures typical of more H₂O-rich basalts.

For rhyolitic magmas, we perform calculations at 800°C for a high-Si rhyolite from Mono Craters (Eastern California) with 77.19 wt% SiO₂ from Liu et al. (2005), and a peralkaline rhyolitic melt inclusion from Aluto Volcano with 73.5 wt% SiO₂ measured by Iddon and Edmonds (2020). The Aluto rhyolite has much lower Al₂O₃ and higher FeO contents than the Mono Craters Rhyolite (Table 1).

Table 1. Representative compositions used for comparisons. MORB1 is a Mid-Oceanic Ridge Basalt tholeiite from Dixon et al. (1995). MORB2 is the MORB composition given in Table 3 of Ghiorso and Gualda (2015), originally from Allan et al. (1989). Etna is sample ET-8 from the supplementary information of Allison et al. (2019). Fuego is the composition of a melt inclusion from Lloyd et al. (2013). Mono Craters is from Table 1 of Liu et al. (2005). Aluto rhyolite is the composition of a quartz-hosted melt inclusion from the East African Rift (MI70 from sample MER055A; Iddon & Edmonds, 2020).

Name	MORB1	MORB2	Etna	Fuego	Mono Craters	Aluto Pumice
SiO ₂	50.8	47.4	48.77	49.67	77.19	73.51
TiO ₂	1.84	1.01	1.79	1.17	0.06	0.23
Al ₂ O ₃	13.7	17.64	16.98	16.50	12.8	9.18
Fe ₂ O ₃	2.1	0.89	2.51	1.65	0.26	1.41
FeO	10.5	7.18	6.44	8.43	0.71	3.81
MnO	0	0	0.18	0.19	0	0.25
MgO	6.67	7.63	6.33	4.38	0.03	0
CaO	11.5	12.44	11.26	7.90	0.53	0.2
Na ₂ O	2.68	2.65	3.65	3.37	3.98	4.18
K ₂ O	0.15	0.03	1.79	0.79	4.65	4.22
P ₂ O ₅	0.19	0.08	0.53	0.22	0	0

609 4.1 Redox sensitivity

610 Before proceeding with these comparisons, it is worth noting that the vast
 611 majority of studies report whole-rock, melt inclusion and matrix glass composi-
 612 tions in terms of FeO_t , because the proportions of FeO vs. Fe_2O_3 are difficult to
 613 determine precisely using common analytical techniques such as electron probe mi-
 614 croanalysis (EPMA) and x-ray fluorescence (XRF). VolatileCalc-Rhyolite and L-2005
 615 have no compositional terms, and VolatileCalc-Basalt is only parametrized in terms
 616 of the melt SiO_2 content, so these 3 models are not sensitive to the choice of FeO
 617 vs. Fe_2O_3 for the representative compositions in Table 1. Similarly, IM-2012 and
 618 M-1998 are parameterized using an FeO_t term, so also show no sensitivity to melt
 619 redox. S-2014 is technically slightly redox-sensitive for CO_2 , because the Π^* term
 620 is expressed in terms of Fe^{2+} species (equation 17). However, as the model was
 621 calibrated assuming $\text{Fe}^{2+} = \text{Fe}_T$, any sensitivity to redox is likely spurious. Thus,
 622 VESical calculates Π with Fe_T by default for consistency with their calibration. In
 623 Figure 4, we perform calculations for different Fe^{3+} ratios for completeness, but the
 624 rest of the figures in the manuscript for S-2014 are calculated using Fe_T . H_2O solu-
 625 bility in S-2014 is not redox sensitive, because the effect of melt composition is only
 626 parametrized in terms of cation fractions of Na and K (equation 18). Both P-2006
 627 and MagmaSat have interaction parameters for Fe^{2+} and Fe^{3+} -bearing species, so
 628 are redox sensitive for both CO_2 and H_2O solubility.

629 We examine the sensitivity of calculations using S-2014, MagmaSat and P-2006
 630 to melt redox by performing calculations for 0, 10 and 20% Fe^{3+} for MORB2, and
 631 0, 30 and 60% Fe^{3+} for Etna (the higher redox accounting for the highly oxidising
 632 conditions of experiments on Etna melts, e.g., Lesne, Scaillet, Pichavant, & Beny,
 633 2011).

634 For Etna, pure H_2O solubility in MagmaSat is relatively insensitive to redox,
 635 predicting variations in dissolved H_2O which are well within model error (Fig. 4a).
 636 Pure CO_2 solubility in MagmaSat is more redox sensitive than H_2O , predicting
 637 $\sim 1.2\text{--}1.3\times$ more CO_2 for 0% Fe^{3+} vs. 60% Fe^{3+} (Fig. 4b). Pure H_2O solubility in
 638 P-2006 shows the same directionality as MagmaSat, but is more sensitive to redox
 639 ($1.8\times$ more H_2O dissolves at 0.1 kbar for 0% Fe^{3+} vs. 60% Fe^{3+} , dropping to $1.2\times$
 640 at > 2 kbar). Pure CO_2 solubility in P-2006 is extremely redox-sensitive, with melts

641 with 0% Fe^{3+} vs. 60% Fe^{3+} dissolving $25\times$ more CO_2 at 0.5 kbar, but $0.5\times$ less
 642 CO_2 at 5 kbar. S-2014 is slightly less redox sensitive than MagmaSat for CO_2 .

643 Varying Fe^{3+} proportions between 0–20% for MORB2 produces similar pat-
 644 terns as Etna, with changes lying within model error for MagmaSat and S-2014,
 645 but showing significant differences for P-2006 (Fig. 4c-d). Isobars for different redox
 646 states for this composition can be found in Supporting Figure S2. For the smaller
 647 changes in Fe^{3+} proportions considered for MORB2, changes in dissolved H_2O and
 648 CO_2 contents for MagmaSat and S-2014 are well within model uncertainty (gener-
 649 ally stated as 10–20%). In contrast, P-2006 shows changes in dissolved CO_2 which
 650 are significantly larger than quoted errors on solubility models.

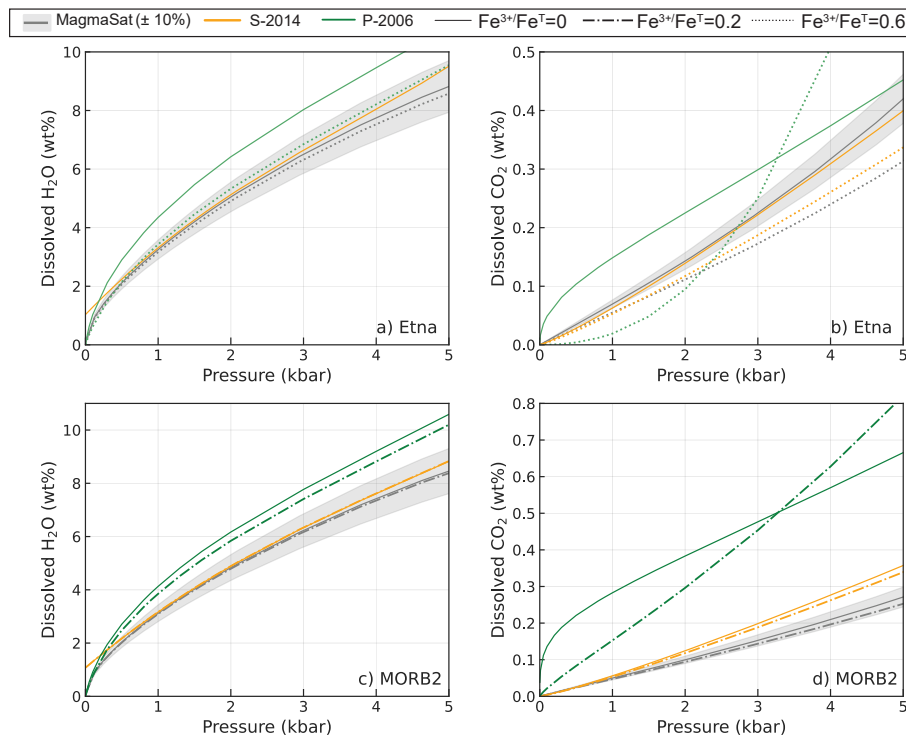


Figure 4. Relationship between volatile solubility and the proportion of Fe^{3+} for: a-b) the Etna composition at 1200°C ; c-d) the MORB2 composition at 1200°C . VESICAL uses FeO_t in S-2014 to calculate Π^* for consistency with the calibration of this model. Here, dashed and dotted lines show the results from calculations where FeO_t is multiplied by $\text{Fe}^{2+}/\text{Fe}_T$, to show the results that would be obtained if VESICAL calculated Π^* using only Fe^{2+} . Isobars for MORB2 and lines for intermediate Fe^{3+} ratios for each composition are shown in Supporting Fig. S2.

651 The cause of the extreme sensitivity of CO₂ in P-2006 to redox relative to
 652 MagmaSat is apparent from examining the interaction coefficients in Table 3. In
 653 MagmaSat, the $W_{Fe_2O_3, H_2O}$ coefficient is only $1.6\times$ bigger than $W_{Fe_2SiO_4, H_2O}$ (~ 50
 654 vs. 31), and these two coefficients overlap within $\pm 1.5\sigma$ of the uncertainty of these
 655 coefficients. This accounts for the relatively weak effect of redox on calculated H₂O
 656 solubility. For the CaCO₃ component representing the carbonate ion, the coefficients
 657 have similar magnitudes, but opposite signs ($W_{Fe_2O_3, CaCO_3} \sim 66$, $W_{Fe_2SiO_4, CaCO_3}$
 658 ~ -73), and this difference is much larger than the error on the coefficients (account-
 659 ing for the stronger effect of melt redox on CO₂ solubility compared with H₂O). The
 660 Fe₂O₃ and Fe₂SiO₄ coefficients for the CO₂ component (which becomes more domi-
 661 nant in more evolved compositions) are also significantly different outside the quoted
 662 error but have the same sign ($W_{Fe_2O_3, CO_2} \sim -32$, $W_{Fe_2SiO_4, CO_2} \sim -3$).

663 In P-2006, the $w_{H_2O-FeO}^0$ coefficient is of similar magnitude, but opposite sign
 664 to $w_{H_2O-Fe_2O_3}^0$ (1.4×10^5 vs. -2×10^5), and clearly distinct outside the error on
 665 each coefficient. This accounts for the slightly stronger sensitivity of H₂O in P-2006
 666 to redox compared with MagmaSat. In stark contrast to all the comparisons thus
 667 far, the $w_{CO_2-Fe_2O_3}^0$ coefficient is $>200\times$ larger than $w_{CO_2-FeO}^0$ for P-2006. In fact,
 668 $w_{CO_2-Fe_2O_3}^0$ is $\sim 8\times$ higher than the next largest coefficient, suggesting that for a
 669 given mole fraction in the melt, it has the largest effect on carbonate ion solubil-
 670 ity. The $w_{CO_2-Fe_2O_3}^1$ coefficient in P-2006 model, which becomes more dominant
 671 at higher pressures, has the opposite sign to that for w_0 . This accounts for the fact
 672 that at low pressures (<3 kbar), increasing proportions of Fe³⁺ cause CO₂ solubility
 673 to decrease, while at higher pressures, increasing proportions of Fe³⁺ cause CO₂
 674 solubility to increase.

675 It is difficult to trust the extreme sensitivity of CO₂ in P-2006 to redox given
 676 the large uncertainty associated with the proportions of Fe³⁺ in volatile solubility
 677 experiments. For example, S-2014 note that only 7 of the 48 experiments in their
 678 calibration dataset contain non-zero values of Fe₂O₃, which is why they choose to
 679 calibrate the model using FeO_t. In the P-2006 dataset, only 6 studies used in the
 680 calibration directly determined the proportion of Fe³⁺, and a further 9 reported
 681 the experimental oxygen fugacity. Thus, for the vast majority of their experimental
 682 calibration dataset, Papale et al. (2006) calculate the proportion of Fe³⁺ assuming
 683 the oxygen fugacity is controlled by the H₂O-H₂ equilibrium at the stated experi-

684 mental conditions. However, this method requires accurate measurements of fluid
685 composition, is affected by Fe and H⁺-loss during experiments, and it is unclear
686 how applicable this method is for mixed H₂O-CO₂ experiments (Botcharnikov et al.,
687 2006). The P-2006 calibration dataset contains some very surprising values: in the
688 calibration dataset for pure CO₂ experiments, the experiments of Fogel and Ruther-
689 ford (1990) have been allocated Fe³⁺/Fe_T ratios of ~0.9–1, despite the authors
690 debating whether their experiments were actually reducing enough to stabilize a CO
691 species. Overall, it is worth noting that the coefficients for CO₂ are relatively under-
692 constrained. While there are 10 coefficients for H₂O calibrated using 865 datapoints
693 of pure-H₂O solubility, there are 20 coefficients for CO₂, and only 173 datapoints for
694 pure-CO₂ solubility and 84 for mixed fluids. In particular, the highly oxidising
695 Fe³⁺/Fe_T ratios calculated assuming H₂O-H₂ equilibrium are more concentrated
696 in experiments with low CO₂ contents and pressures, making it difficult to decon-
697 volve the differential effects of these parameters in a model with a large number of
698 coefficients being calibrated on a relatively small calibration dataset.

699 In sections 4.2 to 5, we show calculations using the Fe³⁺/Fe_T proportions
700 in Table 1, as these best-estimates for each center are representative of what a
701 user would select when calculating melt inclusion saturation pressures, dissolved
702 volatile contents etc. For MORB1, MORB2, and Fuego, these proportions are from
703 the original publications. For Etna, Fe₂O₃ was calculated from FeO_t assuming
704 Fe³⁺/Fe_T=0.26 after Gaborieau et al. (2020). For Mono Craters and the Aluto
705 pumice, Fe³⁺/Fe_T was set at 0.25 based on available data on other rhyolites (e.g.,
706 Ghiorso and Gualda, 2015), and modelling studies of the fractional crystallization
707 path at Aluto (Gleeson et al., 2017).

708 **4.2 Mafic Compositions**

709 **4.2.1 Pure H₂O**

710 The 7 models applicable to H₂O in basaltic systems predict a sharp rise in pure
711 H₂O solubility with increasing pressure (Fig. 5). For all three melt compositions,
712 S-2014, IM-2012-A, VolatileCalc-Basalt, and M-1998 predict H₂O concentrations
713 within ±10% of MagmaSat (grey envelope) between ~1–5 kbar. For MORB1 and
714 MORB2, IM-2012-H begins to deviate to higher H₂O contents than MagmaSat at

715 >1 kbar. For Etna, IM-2012-H follows a similar trajectory between 0–3 kbar to the
 716 solubility model of Lesne, Scaillet, Pichavant, Iacono-Marziano, and Beny (2011)
 717 developed specifically for Etna melts (yellow line, Fig. 5d). In contrast, P-2006 plots
 718 to substantially higher H₂O solubilities compared to all other models at >0.5 kbar
 719 (although P-2006 and IM-2012-H intercept at higher pressures).

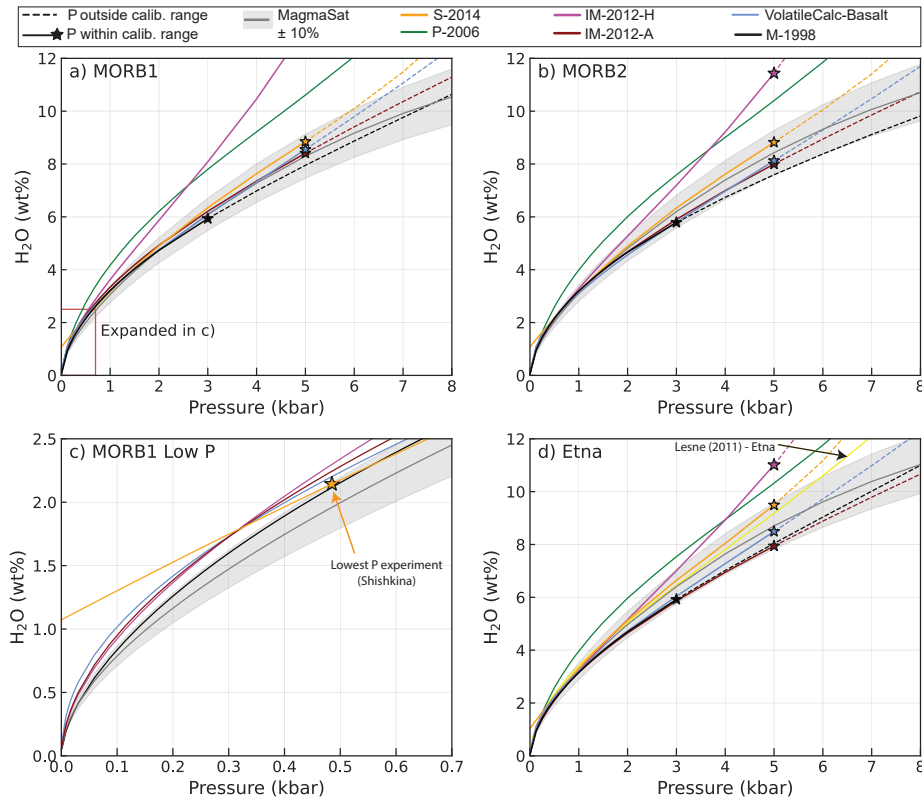


Figure 5. Relationship between pure H₂O solubility and pressure for MORB1, MORB2 and Etna melts at 1200°C. The grey field shows a ±10% error window around MagmaSat. Model lines are dashed when extrapolated above the recommended pressure range. The low pressure region of a) is expanded in c), emphasizing the non-zero solubility of H₂O at P=0 bar in the S-2014 model.

720 The fact that IM-2012-H predicts higher H₂O solubility relative to the cluster
 721 of other models lying within the error window of MagmaSat is an interesting obser-
 722 vation. Iacono-Marziano et al. (2012) favour their hydrous model, particularly for
 723 CO₂-poor, H₂O-rich melts, based on regressions between predicted and measured
 724 H₂O contents, and by comparing the two models to experiments conducted between

725 1 and 4 kbar on Etna melts (their Figure 7a). However, their Figure 8c, which com-
 726 pares dissolved volatile contents calculated by the model for the entire calibration
 727 dataset, shows that predicted H₂O contents using the hydrous version are overesti-
 728 mates for experimental products with >6–7 wt% H₂O (although these predictions
 729 still lie within the ~17% error associated with their H₂O model). Our comparisons
 730 suggest that the anhydrous model is most similar to other models, so should not
 731 automatically be discounted in favour of the hydrous model.

Another notable oddity is the nearly linear trajectory of H₂O vs. P in S–2014
 at <0.5 kbar, causing this model to predict a non-zero solubility of H₂O at 0 bar
 (Fig. 5c). This contrasts with the power-law shapes followed by the other models
 which intercept very close to the origin. This anomalous behaviour is because the
 S–2014 equation for H₂O solubility (equation 18) simplifies at P=0 to:

$$[\text{H}_2\text{O}]^{\text{wt}\%} = -1.1309(\text{X}_{\text{Na}} + \text{X}_{\text{K}}) + 1.1297 \quad (19)$$

732 In the S–2014 calibration dataset, $\text{X}_{\text{Na}} + \text{X}_{\text{K}}$ varies from 0.05 to 0.25, which corre-
 733 sponds to solubilities of 0.85–1.07 wt% H₂O at 0 bar. This demonstrates the issue
 734 with extrapolating empirical expressions beyond the calibration range (the lowest
 735 pressure experiment in the calibration dataset of S–2014 was conducted at 485 bar).
 736 When combined with the assumption of ideal mixing used in VESIcal, this non-zero
 737 solubility of H₂O at 0 bar results in S–2014 predicting unusual degassing paths and
 738 isobar shapes relative to other models. For example, if a melt has <1 wt% H₂O, S–
 739 2014 predicts that the co-existing fluid contains no H₂O, despite abundant evidence
 740 that volcanic plumes in low H₂O systems such as Hawai’i are dominated by H₂O at
 741 low pressures (Gerlach, 1986). It also causes isobars to be entirely flat at low H₂O
 742 contents (see section 4.2.2, Fig. 6).

743 Overall, excluding P–2006 and IM–2012–H based on their higher predictions
 744 of H₂O solubility, and S–2014 based on anomalous behavior at low H₂O contents,
 745 the remaining four solubility models predict dissolved H₂O concentrations within
 746 error of one another at pressures lower than the upper calibration limit. This likely
 747 reflects the relatively small effect of melt composition of H₂O solubility, meaning
 748 that more recent models calibrated on a wider compositional range display similar
 749 behavior to older models (G. Moore & Carmichael, 1998; Papale et al., 2006). The
 750 larger deviation between models at higher pressures reflect the fact that very few

751 pure-H₂O solubility experiments have been performed at > 5 kbar (Table 1). One
752 reason for this shortage of higher pressure experimental data results from the fact
753 that it is very difficult to quench silicate melts with >9 wt% H₂O to a glass phase
754 which can be analysed by FTIR or SIMS (Gavrilenko et al., 2019; Mitchell et al.,
755 2017).

756 *4.2.2 Mixed H₂O-CO₂*

757 The majority of experiments used to calibrate expressions for pure-CO₂ solu-
758 bility contained dissolved H₂O and CO₂ (e.g., Iacono-Marziano et al., 2012; Shishk-
759 ina et al., 2014; Allison et al., 2019), requiring authors to assess H₂O-CO₂ mixing
760 behaviour to determine the solubility of pure-CO₂ fluids. Thus, it makes sense to
761 consider the treatment of mixing between CO₂ and H₂O species in each model
762 before considering predictions of pure CO₂ solubility which are affected by these
763 assumptions. The treatment of H₂O-CO₂ mixing is best demonstrated using isobar
764 diagrams, which show the solubility of H₂O and CO₂ in a given silicate melt com-
765 position at a given pressure for proportions of $X_{H_2O}^f$ in the co-existing fluid ranging
766 from 0 (interception with the y axis) to 1 (interception with the x axis). The treat-
767 ment of mixed fluids differs quite considerably in each model.

768 VolatileCalc-Basalt models mixed fluids under the assumption of Henrian
769 (ideal) mixing in the fluid and melt phase. Thus, the addition of H₂O always causes
770 the solubility of CO₂ to decrease (and vice versa), and isobars possess a nega-
771 tive gradient, with a slightly sloping plateau at low H₂O contents merging into a
772 concave-down shape (Fig. 6).

773 S-2014 does not provide an equation for the treatment of non-ideal mixing,
774 despite their experiments showing that increasing H₂O contents at high pressure
775 cause almost no change in CO₂ solubility. Using the assumption of ideal mixing in
776 VESIcal, S-2014 isobars exhibit a flat plateau at low H₂O contents, merging into
777 a negative slope at higher H₂O contents. This flat plateau results from the fact
778 that there are no partial pressures at which S-2014 yields H₂O < 1 wt%, so the y
779 co-ordinate for lower H₂O contents is equal to the solubility of pure CO₂.

780 P-2006 is fully non-ideal, which causes isobars to have complex shapes, ex-
781 hibiting both positive and negative gradients. In detail, the shape of isobars calcu-

782 lated using P-2006 differ as a function of both melt composition and temperature
783 (see Fig. 12 of Papale, 1999). For the basaltic compositions considered here, isobars
784 show a sharp increase to higher CO₂ contents at very low H₂O contents (Fig. 6a,
785 c), because the model predicts a decrease in CO₂ solubility following the addition of
786 small quantities of H₂O.

787 IM-2012-A and IM-2012-H incorporate empirical representations of non-
788 ideality through the inclusion of a term for the molar fraction of H₂O in the melt in
789 their expression for CO₂ solubility (equation 11). This means that these models pre-
790 dict that maximum CO₂ solubility occurs at non-zero H₂O concentrations, causing
791 isobars to display prominent domed shapes (Fig. 6). Isobars calculated using IM-
792 2012-A show a more extreme peak than IM-2012-H, because of the difference in the
793 sign and magnitude of the d_{H_2O} coefficient combined with the differences between
794 NBO/O calculated on a hydrous and anhydrous basis (see Supporting Information
795 for further detail).

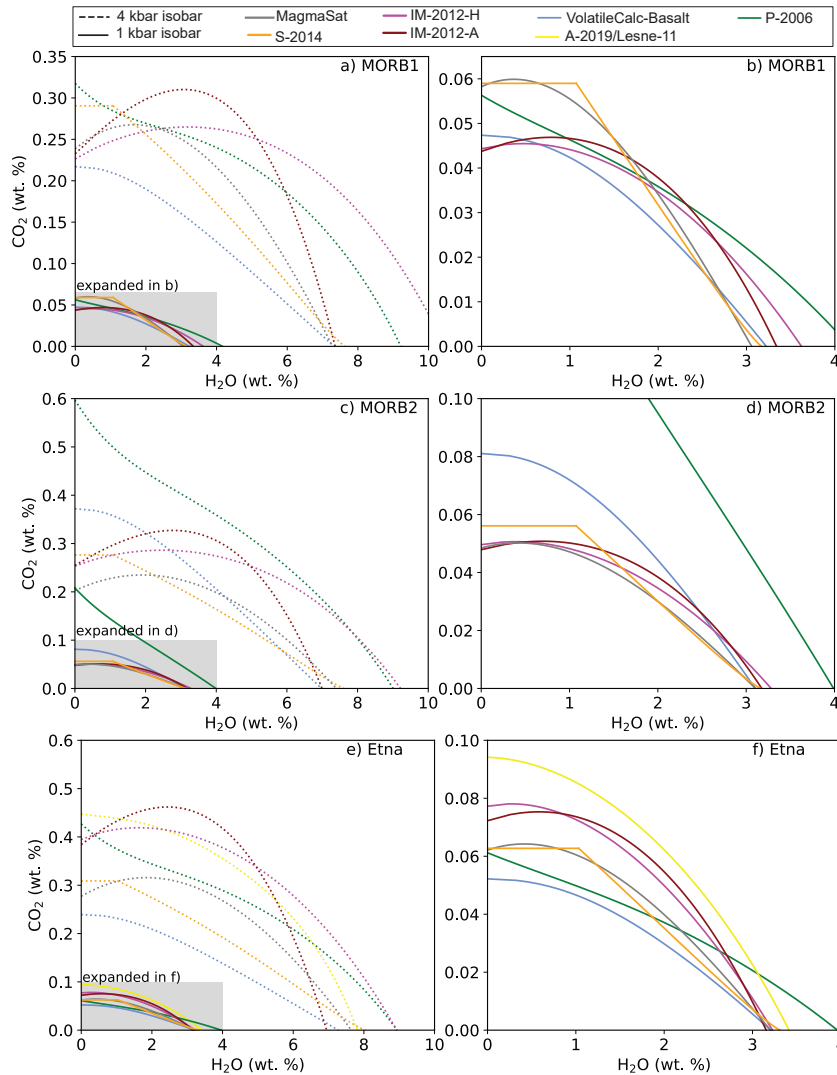


Figure 6. 1 and 4 kbar isobars for MORB1 (a-b) and MORB2 (c-d) and Etna (e-f) at 1200°C. The 1 kbar isobar is expanded in b), d) and e). The distinctive shapes of isobars from different models reflects different treatment of H₂O-CO₂ mixing. This is most apparent at higher pressures. The prominent plateau at <1 wt% H₂O for S-2014 at all pressures results from the non-zero solubility of H₂O at low pressures.

796 Like P-2006, MagmaSat is fully non-ideal. However, unlike P-2006, the treat-
 797 ment of non-ideality in MagmaSat predicts that the addition of small amounts of
 798 H₂O always causes the solubility of CO₂ to increase (so isobars peak at non-zero
 799 H₂O concentrations; Fig. 6, c). This peak becomes more pronounced at higher pres-
 800 sures, but is generally smaller than that predicted by IM-2012.

801 These different mixing assumptions result in large discrepancies between the
802 predicted volatile solubilities for melts in equilibrium with H₂O-CO₂ fluids, par-
803 ticularly at higher pressures where non-ideal behaviour is more pronounced. For
804 example, while IM-2012-A predicts similar pure CO₂ and pure H₂O solubilities to
805 VolatileCalc-Basalt and MagmaSat for MORB1 at 4 kbar (interception with x and
806 y axis on Fig. 6a), IM-2012-A predicts that melts with ~ 4 wt% H₂O can dissolve
807 more than twice as much CO₂ as that predicted by VolatileCalc-Basalt.

808 4.2.3 Pure CO₂

809 All basaltic compositions and models show a large increase in the solubility of
810 pure CO₂ with increasing pressure (Fig. 7). The solubility of pure CO₂ is approx-
811 imately an order of magnitude lower than for H₂O (compare Fig. 7 with Fig. 5).
812 This solubility difference accounts for the fact that Mid Oceanic Ridge (MOR) mag-
813 mas, which have similar concentrations of H₂O and CO₂ (~ 0.07 wt% H₂O, 0.1–0.2
814 wt% CO₂; Le Voyer et al., 2019), are almost always CO₂ saturated during crustal
815 storage (Saal et al., 2002) but only exsolve measurable quantities of H₂O if erupted
816 at very low pressures (Le Voyer et al., 2019).

817 For MORB1, IM-2012-A and H, and VolatileCalc-Basalt lie within, or close to
818 the ± 10% error window on MagmaSat at <5 kbar, and S-2014 lie within ± 20%.
819 The deviation at higher pressures is expected, because only P-2006 and MagmaSat
820 are calibrated on large numbers of experiments performed at > 5 kbar (Fig. 1). For
821 example, the relationship between II and CO₂ solubility of Dixon (1997) used in
822 VolatileCalc-Basalt was based on experiments at 1 kbar, and Newman and Lowen-
823 stern (2002) suggest that it should not be extrapolated above 5 kbar. Similarly, only
824 the experiments of Jakobsson (1997) in the IM-2012 database were conducted at >5
825 kbar, and there are no experiments in the calibration dataset of S-2014 performed at
826 >5 kbar. Unlike for pure H₂O, IM-2012-A and H predict very similar pure CO₂ sol-
827 ubilities to one another. This reflects the fact the coefficients for CO₂ between these
828 2 model versions are very similar apart from the d_{H_2O} term, which is multiplied by a
829 zero when calculating pure CO₂ solubility. In contrast, P-2006 plots to significantly
830 higher pressures than the other models (~ 2× higher at ~8 kbar).

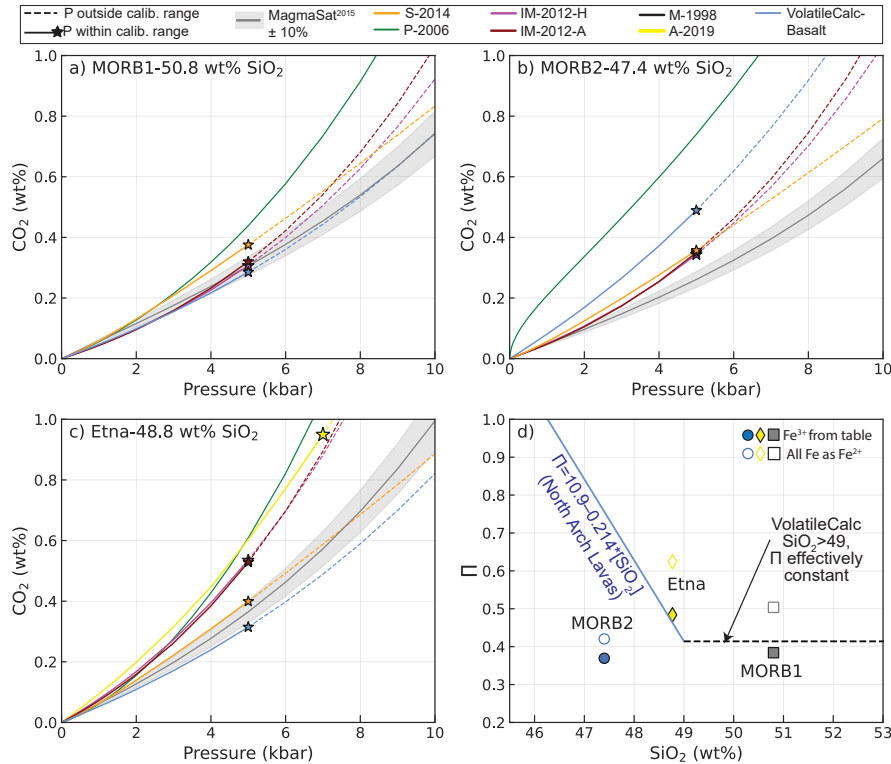


Figure 7. Relationship between pure CO₂ solubility and pressure for three mafic melts at 1200°C: a) MORB1 from Dixon et al. (1995), b) MORB2 from Ghiorso and Gualda (2015), and c) Etna from Allison et al. (2019). Models extrapolated beyond their calibrated pressure range are shown as dashed lines, with the colored star marking the recommended upper calibration limit. d) The relationship between II and SiO₂ defined by the North Arch lavas is shown in blue (Dixon, 1997). Generally, VolatileCalc-Basalt is applied to melts with >49 wt% SiO₂ by setting SiO₂=49 wt%; the black dashed line represents this extrapolation. These simplified relationships incorporated into VolatileCalc-Basalt (blue and black lines) underestimate the true II value for Etna, and overestimate it for MORB2.

831 MORB2 shows a significantly larger discrepancy between models than MORB1
 832 (Fig. 7b), While S-2014, IM-2012-H and -A follow very similar trajectories at
 833 <5 kbar, P-2006 predicts that MORB2 dissolves ~3370 ppm CO₂ at 2 kbar while
 834 MagmaSat predicts only ~950 ppm (factor of 3.5×), and VolatileCalc-Basalt also
 835 predicts higher CO₂ solubility relative to MagmaSat by a factor of 1.8× at 2 kbar.

836 The high CO₂ solubility predictions by P-2006 relative to other models and ex-
 837 perimental measurements has also been noted by Shishkina et al. (2010), Shishkina

838 et al. (2014) and Mangan et al. (2021). This may result from the fact that the P-
839 2006 uses a negative compressibility for the CO₂ fluid (Ghiorso & Gualda, 2015).
840 Alternatively, it may reflect the large errors on the CO₂ w coefficients, meaning that
841 the effect of melt composition is uncertain, accounting for the larger discrepancy
842 for MORB1 vs. MORB2 compared to other models. Finally, Shishkina et al. (2010)
843 suggest that the overprediction of CO₂ solubility by P-2006 may result from the
844 inclusion of anomalously high CO₂ contents from the experiments of Freise (2004)
845 in the calibration dataset of P-2006 (these values have now been revised to lower
846 numbers, as the original FTIR thickness correction factor is thought to have been
847 incorrect).

848 The fact that VolatileCalc-Basalt plots close to other models for MORB1 but
849 not MORB2 is a good example of the main caveat of the Π -SiO₂ simplification
850 used to account for the effect of melt composition on CO₂ solubility. For melts with
851 40–49 wt% SiO₂, VolatileCalc-Basalt assumes that the relationship between CO₂
852 solubility and SiO₂ is identical to that defined by the North Arch lavas, shown in Π
853 vs. SiO₂ space as a blue line in Fig. 7d. This is a reasonable approximation for the
854 MORB1 composition, which has a Π value similar to North Arch Lavas with 49 wt%
855 SiO₂. However, the MORB2 composition lies significantly below the line defined by
856 North Arch lavas, so has a lower Π value, and therefore a lower CO₂ solubility at a
857 given SiO₂ content compared to the North Arch Lavas. Thus, VolatileCalc-Basalt
858 likely overpredicts the solubility of CO₂ in this melt composition.

859 Furthermore, VolatileCalc-Basalt predicts that MORB2 dissolves ~ 1.7 times
860 more CO₂ at a given pressure than MORB1. This is because MORB2 has 3.4 wt%
861 less SiO₂ than MORB1, and VolatileCalc-Basalt predicts that CO₂ solubility in-
862 creases drastically with decreasing SiO₂. However, if the full Π expression of Dixon
863 (1997) were used, MORB1 and MORB2 would have very similar CO₂ solubility,
864 as they have similar Π values despite different SiO₂ contents. P-2006 also predicts
865 that MORB2 dissolves $5\text{--}6\times$ more CO₂ at 0.4 kbar, and $1.9\times$ more at 4 kbar than
866 MORB1. In contrast, the models of S-2014, IM-2012, and MagmaSat predict that
867 MORB1 and MORB2 dissolve similar amounts of CO₂ (MORB2/MORB1= $\sim 0.99\times$,
868 $\sim 1.125\times$ and $\sim 0.81\text{--}0.89\times$ respectively). These three more recent models utilize
869 significantly larger basaltic calibration datasets to parametrize the effect of multiple
870 oxide species melt on CO₂ solubility (Fig. 2), so likely predict more realistic solubil-

871 ity relationships than VolatileCalc-Basalt and P-2006. In summary, CO₂ solubility
872 in melt compositions that do not follow a similar trajectory in II-SiO₂ space as the
873 North Arch Lavas (Fig. 7d) is unlikely to be accurately predicted by VolatileCalc-
874 Basalt.

875 There is also significant deviation between different models for Etna melts
876 (Fig. 7c), which is far greater than that observed for H₂O (Fig. 5). The A-2019
877 model, developed specifically for the composition of Etna magmas, predicts much
878 higher CO₂ solubility at a given pressure than VolatileCalc-Basalt, S-2014, and
879 MagmaSat, while P-2006 and IM-2012-H and -A follow similar trajectories to
880 A-2019. The success of both IM-2012 models likely reflects the large number
881 of alkaline compositions in their calibration dataset, including some from Etna.
882 VolatileCalc-Basalt predicts the lowest CO₂ solubility (factor of 0.5–0.6× that of
883 A-2019). The calculated II value for Etna lies significantly above the line defined
884 by North Arch lavas (so VolatileCalc-Basalt predicts lower CO₂ solubility; Fig. 7d).
885 However, even the full II expression of Dixon (1997) is unlikely to be successful, be-
886 cause alkaline magmas show considerable variation in CO₂ solubility at a given II
887 value (Allison et al., 2019). As S-2014's expression for CO₂ solubility incorporates
888 a II* term very similar to the II term of Dixon (1997), the deviation of this model
889 from that of A-2019 (0.6–0.7×) may also result from variations in CO₂ solubility
890 that are not incorporated by this simplified melt composition parameter (Allison et
891 al., 2019).

892 Interestingly, MagmaSat also underpredicts CO₂ concentrations at a given
893 pressure relative to A-2019 by a factor of 0.6–0.7×, despite incorporating CO₂ ex-
894 periments on Etna basalts from Lesne, Scaillet, Pichavant, and Beny (2011) and
895 Iacono-Marziano et al. (2012) in its calibration dataset. This is a good example of
896 the main pitfall of comprehensive models such as MagmaSat and P-2006 which can
897 predict volatile solubility across the entire range of natural silicate melt composi-
898 tions (Papale et al., 2006). For any specific melt composition, the model is highly
899 unlikely to be as well tuned as models calibrated on melts from a specific volcanic
900 center (e.g., Allison et al., 2019) or heavily weighted towards a specific region of
901 compositional space (e.g., Iacono-Marziano et al., 2012, for alkaline basalts). Tuning
902 MagmaSat to provide a better fit to Etna would almost certainly cause this model to
903 show larger discrepancies for experiments conducted on different melt compositions.

904 **4.3 Silicic Compositions**

905 **4.3.1 Pure H₂O**

906 All five H₂O models calibrated for silicic magmas (MagmaSat, P-2006, L-2005,
907 VolatileCalc-Rhyolite and M-1998) predict very similar H₂O concentrations at <1–
908 1.5 kbar for the Mono Craters rhyolite composition (Fig. 8a, Table 1). At higher
909 pressures, P-2006, and to a much lesser extent L-2015, show a smaller increase in
910 H₂O solubility with pressure compared to MagmaSat, M-1998 and VolatileCalc-
911 Rhyolite (the difference in H₂O solubility between models reaches ~4 wt% at 5
912 kbar). As discussed for basalt, the large discrepancies at higher pressures and H₂O
913 contents likely results from an absence of experimental constraints because of chal-
914 lenges related to quenching melts with >6-9 wt% H₂O (Gavrilenko et al., 2019). The
915 trajectories of models with compositional terms (M-1998, P-2006, MagmaSat) are
916 very similar for Aluto.

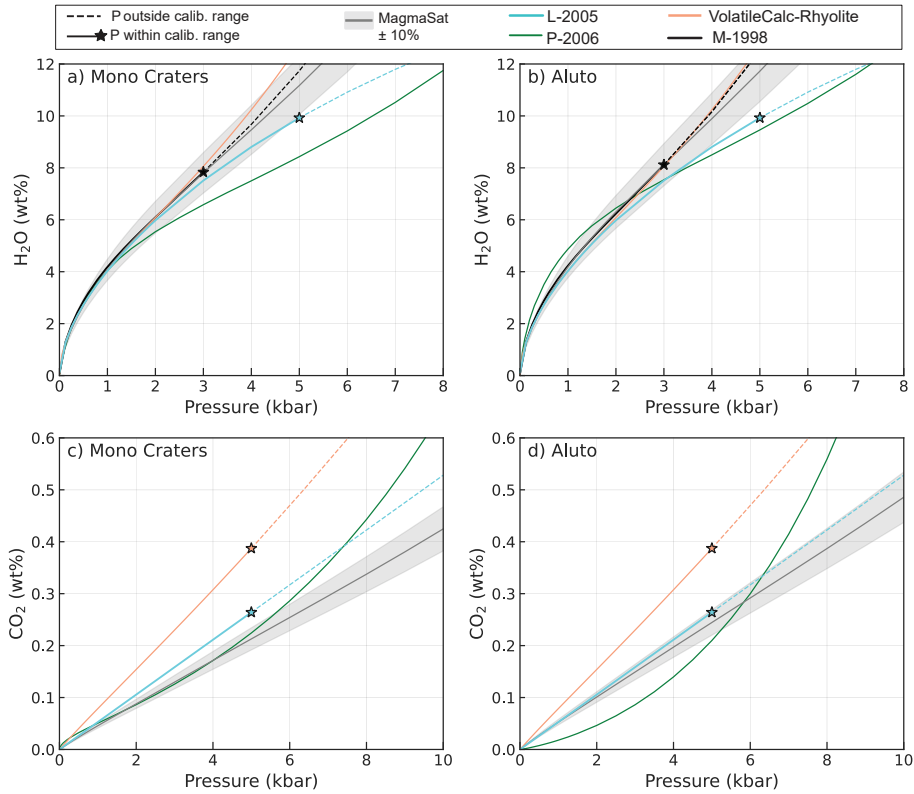


Figure 8. Relationship between pure H₂O (a-b) and pure CO₂ (c-d) solubility and pressure at 800°C for the Mono Lake rhyolite from Liu et al. (2005), and a peralkaline Rhyolite from Aluto in the East African Rift (Iddon and Edmonds, 2020). Models extrapolated beyond their calibrated pressure range are shown as dashed lines, with the colored star marking the recommended upper calibration limit.

917

4.3.2 Mixed H₂O-CO₂

918

919

920

921

922

923

924

925

926

Differences in the treatment of H₂O-CO₂ mixing for rhyolitic melts are more subtle than for basaltic compositions (Fig. 9). Unlike for basalts, the differences in isobar positions mostly result from large differences between the pure CO₂ solubility predicted by different models rather than different formulations of mixing. Only VolatileCalc-Rhyolite assumes ideal mixing of H₂O-CO₂, causing isobars to have a negative gradient at all pressures. L-2005 accounts for non-ideal mixing through the inclusion of a term for the mole fraction of H₂O in the fluid in their expression for CO₂ solubility (equation 5). This empirical representation of non-ideality causes isobars to exhibit a prominent peak at low H₂O contents (Fig. 9). MagmaSat and

927 P-2006, which include a fully non-ideal treatment of mixing, show a far less promi-
 928 nent peak than L-2005. The slight up-tick in the P-2006 isobars at very low H₂O
 929 contents is much smaller than for basaltic compositions (e.g., Fig. 6).

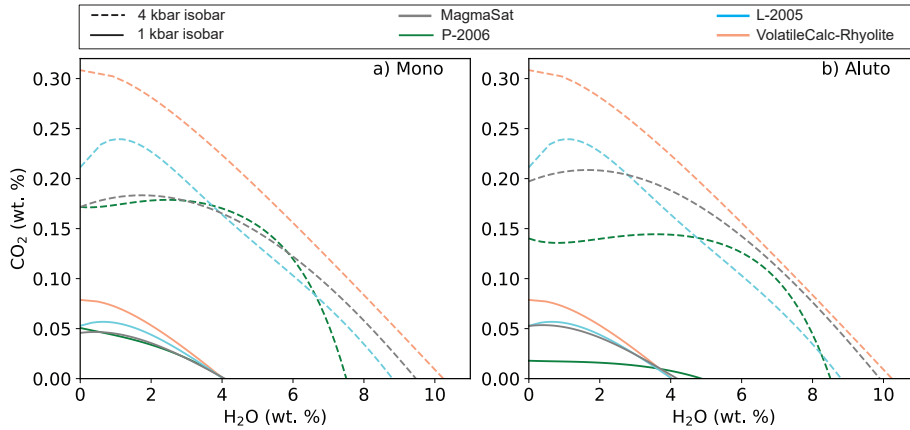


Figure 9. 1 and 4 kbar isobars for Mono Craters (a) and the Aluto rhyolite (b) at 800°C.

930 4.3.3 Pure CO₂

931 Unlike the relatively good correspondence between rhyolite H₂O models (par-
 932 ticularly at low pressures), there is substantial divergence between CO₂ models at all
 933 pressures (Fig. 8c, d). For the Mono Craters rhyolite, VolatileCalc-Rhyolite predicts
 934 $\sim 1.8\times$ more dissolved CO₂ than MagmaSat at 2 kbar, while Liu, P-2006 and Mag-
 935 maSat plot relatively close to each other at <5 kbar. As VolatileCalc-Rhyolite and
 936 L-2005 have no compositional dependence, the model lines are identical for Mono
 937 Craters and Aluto. MagmaSat predicts that the Aluto composition has slightly
 938 higher CO₂ solubility at a given pressure compared to the Mono Lake composition
 939 (factor of $\sim 1.2\times$), so the discrepancy between MagmaSat, VolatileCalc-Rhyolite and
 940 L-2005 is smaller for Aluto than Mono Craters.

941 The P-2006 model shows a substantially different trajectory for CO₂ vs. pres-
 942 sure compared to the other three solubility models for both rhyolite compositions,
 943 showing a strongly concave-up shape compared to the near linear trajectory of L-
 944 2005 and VolatileCalc-Rhyolite, and the slightly concave-up shape of MagmaSat
 945 (Fig. 8c-d). For Mono Craters, P-2006 predicts similar CO₂ solubility to MagmaSat
 946 at <4 kbar, but rapidly rises to higher CO₂ contents at higher pressures, predict-

947 ing almost as much dissolved CO₂ as VolatileCalc-Rhyolite at ~12 kbar (Fig. 8c).
948 For Aluto, the curvature of the P-2006 model is even more prominent, predicting
949 drastically lower CO₂ contents than all other models at <6 kbar, and then rapidly
950 rising, predicting higher CO₂ solubility than even VolatileCalc-Rhyolite at >9 kbar
951 (Fig. 8d). These large deviations between models, as well as the large errors on the
952 interaction terms for CO₂ solubility in MagmaSat (Table 3) demonstrate that while
953 H₂O solubility in rhyolites is well constrained, more work is required to determine
954 the effect of melt composition on CO₂ solubility at a range of pressures and temper-
955 atures.

956 **4.4 Comparisons between Basalts and Rhyolites**

957 In this section, we briefly discuss the differences in solubility between basalts
958 (using the MORB1 composition) and rhyolites (using the Mono Craters composi-
959 tion). To differentiate the effect of melt composition from temperature (because
960 basaltic melts tend to be hotter), we perform calculations at 800 and 1000°C for
961 Mono Craters, and 1000°C and 1200°C for MORB1.

962 When all solubility models are compared (4 applicable to rhyolites, 6 to
963 basalts), there is substantial overlap between curves calculated for MORB1 at
964 1200°C and Mono Craters at 800°C (compare Fig. 11a vs. Fig. 8a). To get around
965 this problem of large differences between models, we compare the predictions from
966 the three models which can be applied to both Rhyolites and Basalts: MagmaSat
967 (Fig. 10a-b), P-2006 (Fig. 10c-d) and VolatileCalc-Basalt and -Rhyolite (Fig. 10e-f).

968 MagmaSat and VolatileCalc (Rhyolite vs. Basalt) predict that Mono Craters
969 dissolves more H₂O than MORB1 at realistic temperatures (800°C vs. 1200°C and
970 at a fixed temperature (1000°C). In contrast, P-2006 predicts that MORB1 dis-
971 solves more H₂O than Mono at realistic temperatures (although their solubilities are
972 nearly identical when compared at 1000°C). For CO₂, MagmaSat and P-2006 pre-
973 dict higher solubilities in MORB1, with the difference becoming more pronounced at
974 higher pressures, while VolatileCalc predicts that at realistic temperature, Mono
975 Craters has higher CO₂ solubility. When compared at the same temperature,
976 VolatileCalc predicts very similar CO₂ solubility for Mono Craters and MORB1.
977 These comparisons demonstrate that at <5 kbar, the difference in solubility between

978 basalts and rhyolites in each model easily overwhelmed by differences in predictions
979 from different solubility models. These discrepancies are enhanced by the different
980 sensitivities of these models to temperature (see section 5.3).

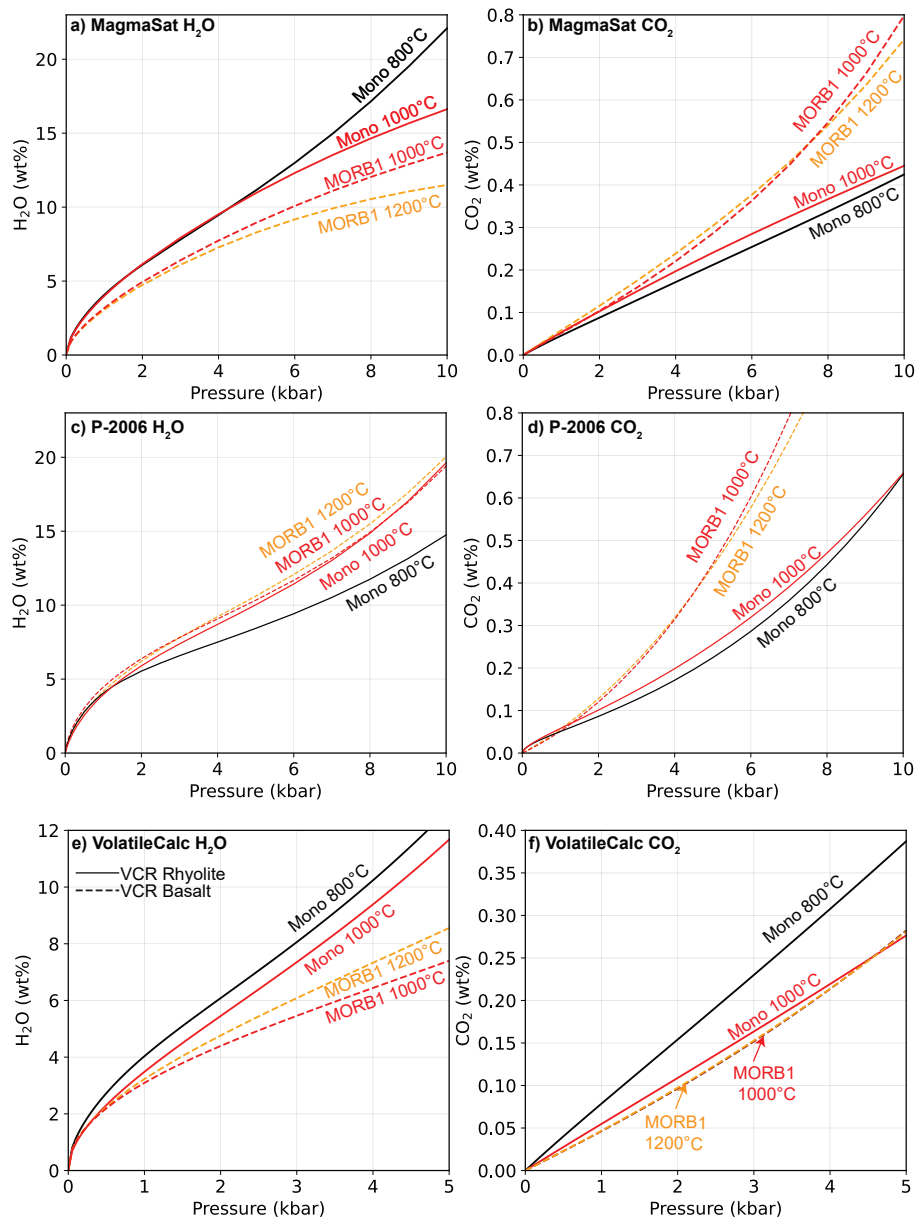


Figure 10. Comparison of solubility of basalt (represented by MORB1) to rhyolite (represented by Mono Craters) using MagmaSat (a-b), P-2006 (c-d) and VolatileCalc-Basalt and Rhyolite (d-e). Solubility curves are calculated for 1200°C and 1000°C for basalt, and 1000°C and 800°C for rhyolite.

5 Model Sensitivities

In this section, we explore the sensitivity of the different models to parameters such as temperature and variable proportions of H₂O and CO₂. Specifically, we consider how these inputs affect calculations of the pressure at which a melt inclusion was trapped (termed the saturation pressure). To calculate saturation pressures, the initial concentration of major and volatile elements as well as the temperature must be estimated at the time of melt inclusion entrapment. However, a number of processes, such as crystallization of the host mineral on the wall of the inclusion (termed post-entrapment crystallization, or PEC), growth of a vapour bubble or daughter phases within the inclusion, and diffusive re-equilibration with a changing carrier liquid composition can make it difficult to reconstruct initial major element and volatile contents (Lowenstern, 1995). Similarly, diffusive re-equilibration of the major elements in the melt inclusion and host mineral, as well as the errors associated with mineral-melt and melt-only thermometers, can lead to uncertainties in the entrapment temperature, which propagates into the saturation pressure. By investigating the effect of varying these parameters within realistic limits, insight can be gained into the uncertainties associated with estimating magma storage depths using melt inclusions.

5.1 Relationship between saturation pressure and dissolved H₂O content

Melt inclusion H₂O contents are vulnerable to diffusional re-equilibration with the melt surrounding the crystal (here termed the carrier melt), because of the fast diffusion rate of H⁺ through silicate minerals (Portnyagin et al., 2008). H⁺ diffusion is particularly fast in olivine (Gaetani et al., 2012), with melt inclusions losing significant amounts of water in hours to days (Bucholz et al., 2013). Thus, this discussion focuses on mafic compositions, where olivine-hosted melt inclusions are frequently analysed.

In relatively H₂O-poor mafic systems such as MORs and ocean islands (e.g., Hawai'i), diffusive re-equilibration can increase melt inclusion H₂O contents if crystals are mixed into more H₂O-rich carrier melts (Hartley et al., 2015), or, more commonly, cause melt inclusion H₂O contents to drop if the crystal is in contact

1012 with a carrier melt that has degassed its H₂O upon eruption (Gaetani et al., 2012;
1013 Bucholz et al., 2013). To assess how uncertainty in initial H₂O contents translates
1014 into errors on saturation pressures, we calculate saturation pressures for the MORB1
1015 melt composition with 200, 1000, and 3000 ppm CO₂ (representing melt inclusions
1016 trapped at low, medium and high pressures) for H₂O contents between 0–1.5 wt%
1017 (Fig. 11a-c). CO₂ contents are held constant while H₂O contents are varied, sim-
1018 ulating the changes undergone by melt inclusions during diffusive re-equilibration
1019 (which strongly affects H₂O contents in the inclusion, but does not change the total
1020 CO₂ budget of the inclusion).

1021 The relationship between saturation pressure and dissolved H₂O predicted by
1022 each solubility model is strongly dependent on the amount of CO₂ in the melt, and
1023 therefore the pressure. To quantify model sensitivity to H₂O, saturation pressures
1024 calculated at H₂O=1.5 wt% are divided by the saturation pressure calculated at
1025 H₂O=0 wt%, representing the possible discrepancy between the calculated satura-
1026 tion pressure and the real saturation pressure for melt inclusions which have under-
1027 gone complete H⁺ re-equilibration with a fully degassed erupted melt at 0 bar. At
1028 low pressures (200 ppm CO₂), all models show a decrease in calculated saturation
1029 pressure with decreasing H₂O contents, with entrapment pressures being 1.2–1.8×
1030 higher before complete H₂O-loss (Fig. 11a). MagmaSat shows the strongest sensitiv-
1031 ity to H₂O content, and both IM-2012 models the weakest.

1032 At moderate pressures (1000 ppm CO₂), loss of H₂O causes a significantly
1033 smaller decrease in saturation pressure for VolatileCalc-Basalt, P-2006 and S-2014
1034 compared to the 200 ppm CO₂ scenario (Fig. 11b, 1.1–1.2×). Saturation pressures
1035 for 1000 ppm CO₂ calculated using MagmaSat and IM-2012-H first decrease, then
1036 increase with H₂O loss. This is because these models predict that the maximum
1037 CO₂ solubility occurs at H₂O contents at ~0.5–1.25 wt% (see Fig. 6).

1038 At higher pressures (3000 ppm CO₂), saturation pressures from VolatileCalc-
1039 Basalt, P-2006 and S-2014 only drop by ~5-10% with progressive H₂O-loss, while
1040 saturation pressures continually increase with progressive H₂O-loss for IM-2012-H
1041 and -A and MagmaSat (because these models predict that maximum CO₂ solubility
1042 is found at H₂O contents >1.5 wt% at these pressures; Fig. 6).

1043 Within a given suite of MORB or OIB melt inclusions, the range of measured
1044 H₂O contents, and the uncertainty involved in reconstructing initial H₂O contents
1045 following diffusional re-equilibration, is likely significantly smaller than the 1.5 wt%
1046 H₂O considered here (Koleszar et al., 2009; Sides et al., 2014a; Wieser et al., 2021).
1047 Thus, except at low pressures (<1 kbar), uncertainties in saturation pressures due to
1048 diffusive re-equilibration of H₂O in relatively anhydrous systems are likely compara-
1049 ble to the analytical errors associated with the measurements of volatile species by
1050 FTIR or SIMS (± 5 –10%), errors on each solubility model (~ 10 –20%), and signifi-
1051 cantly smaller than the differences between solubility models.

1052 The higher H₂O contents of melt inclusions from subduction zones (~ 2 –6
1053 wt%; Plank et al., 2013) mean that substantially more H₂O can be lost following
1054 diffusive re-equilibration with a degassed carrier melt upon eruption. Additionally,
1055 arc melt inclusions are vulnerable to diffusive re-equilibration during crustal stor-
1056 age. This is because these relatively hydrous magmas saturate in a H₂O-rich fluid
1057 at high pressures in the crust. Thus, as a melt and its crystal cargo ascends from
1058 a deeper storage reservoir to a shallower storage reservoir, significant quantities of
1059 H₂O will be degassed and the H₂O contents of melt inclusions will rapidly diffusively
1060 re-equilibrate with the new carrier melt composition (Gaetani et al., 2012). Even
1061 if samples are rapidly quenched upon eruption (preventing syn-eruptive H₂O diffu-
1062 sion), only the volatile contents of melt inclusions trapped in the shallowest storage
1063 reservoir can be reliably converted into saturation pressures (Gaetani et al., 2012).
1064 This contrasts with more H₂O-poor systems such as mid-oceanic ridges and oceanic
1065 islands, where H₂O only degasses in the upper few hundred metres of the crust, so
1066 ascent to a shallower reservoir is not accompanied by a drop in melt H₂O contents
1067 (although diffusive re-equilibration could occur if the resident melts in the shallower
1068 reservoir have different H₂O contents; Hartley et al., 2015).

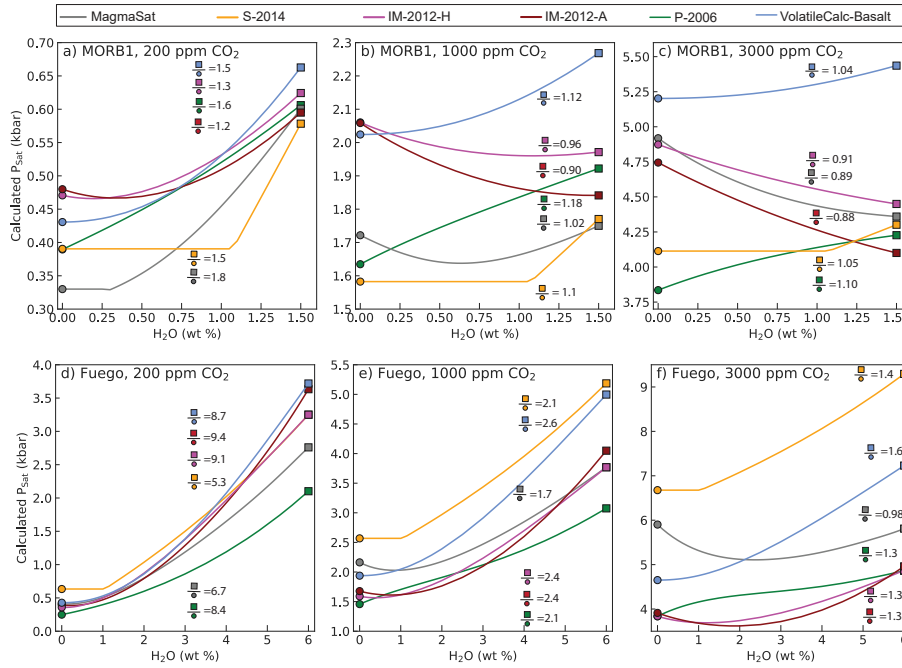


Figure 11. a-c) Relationship between saturation pressure and melt H₂O content for H₂O-poor melts (using the MORB1 composition at 1200°C). Three different melt CO₂ contents (200, 1000, 3000 ppm) are shown in part a, b and c respectively. The numbers on the graphs show the saturation pressure at 1.5 wt% H₂O (square symbol) divided by the saturation pressure at 0 wt% H₂O for each model. d-f) Sensitivity tests using the composition of a Fuego melt inclusion (Table 1) at 1000°C, and H₂O contents between 0–6 wt%. Note that the y scale for parts a-c is significantly smaller than parts d-f.

1069 To investigate the effect of H₂O re-equilibration on melt inclusion saturation
 1070 pressures in arcs, we repeat the sensitivity test described above, using the major
 1071 element composition of a Fuego melt inclusion with 49.7 wt% SiO₂ from Lloyd et
 1072 al. (2013, Table 1) and H₂O contents between 0–6 wt% (Fig. 11d-f). For melt in-
 1073 clusions with 200 ppm CO₂, complete diffusive loss of H₂O may result in saturation
 1074 pressures being underestimated by a factor of ~5–10×. Even for melts with 3000
 1075 ppm CO₂ (the highest pressure regime examined, and thus the best case scenario),
 1076 diffusive loss can affect saturation pressures by factors of 0.98–1.6× (similar in mag-
 1077 nitude to the sensitivity displayed by H₂O-poor melts at the lowest pressures; Fig.
 1078 11a vs. f). Only saturation pressures calculated in MagmaSat for the most CO₂-rich
 1079 melts display variations with variable H₂O-loss similar in magnitude to analytical

1080 errors. Thus, it is extremely important to determine whether melt inclusions have
1081 undergone H₂O-loss during ascent to a shallower reservoir or syn-eruptive degassing
1082 before using saturation pressures to deduce magma storage depths in H₂O-rich vol-
1083 canic systems.

1084 **5.2 Relationship between saturation pressure and dissolved CO₂** 1085 **content**

1086 Estimating the initial CO₂ contents of melt inclusions is also challeng-
1087 ing. While the total CO₂ content of the inclusion is not affected by diffusive re-
1088 equilibration, CO₂ may be partitioned from the melt phase into a vapour bubble.
1089 Cooling following melt inclusion entrapment is accompanied by the formation of a
1090 denser mineral phase from a less dense silicate melt, and differential thermal con-
1091 traction of the melt and crystal. These processes cause the internal pressure of the
1092 inclusion to drop (Steele-Macinnis et al., 2011; Maclennan, 2017), driving the nu-
1093 cleation and growth of a vapour bubble. This may be enhanced by the diffusive
1094 loss of H₂O, which also causes a pressure drop in the melt inclusion because of the
1095 high molar volume but low molecular weight of H₂O (Gaetani et al., 2012; Aster et
1096 al., 2016). A drop in pressure, combined with a decrease in the solubility of CO₂
1097 in the melt phase because of changes to the major element composition accompa-
1098 nying post-entrapment crystallization, causes CO₂ to partition strongly into the
1099 vapour bubble (L. R. Moore et al., 2015; Steele-Macinnis et al., 2011; Maclennan,
1100 2017; Wieser et al., 2021). A number of recent studies have quantified the amount of
1101 CO₂ in vapour bubbles using Raman Spectroscopy, and demonstrated that between
1102 15–99% of the total CO₂ budget of the inclusion may be held within the vapour
1103 bubble (Hartley et al., 2014; L. R. Moore et al., 2015; Wieser et al., 2021; Allison
1104 et al., 2021). This means that a large proportion of literature melt inclusion data,
1105 which only measured the CO₂ content of the glass phase, may have significantly
1106 underestimated initial CO₂ contents (and therefore saturation pressures).

1107 In relatively H₂O-poor systems such as Hawai'i and Iceland, where melt in-
1108 clusion CO₂ contents have the dominant control on saturation pressures (shown by
1109 the near horizontal slopes of most model isobars at low H₂O contents; Fig. 6), it is
1110 readily apparent that saturation pressures will be significantly underestimated if a
1111 CO₂-rich vapour bubble is not measured. In arcs, H₂O contents inferred from melt

1112 inclusions or mineral hygrometers are sometimes used to place first order constraints
 1113 on saturation pressures (e.g. Plank et al., 2013; Blundy & Cashman, 2005; Goltz
 1114 et al., 2020). However, even in very H₂O-rich melts, the non-vertical orientation of
 1115 isobars at high H₂O contents indicates that CO₂ contents still have an important
 1116 role in determining the saturation pressure (Fig. 6). Additionally, only a very small
 1117 number of studies have measured CO₂ in melt inclusion vapour bubbles from arc
 1118 systems (L. R. Moore et al., 2015; Aster et al., 2016; Venugopal et al., 2020; Mironov
 1119 et al., 2020). Thus, it is vital to determine the effect of CO₂ on saturation pressures
 1120 in H₂O-rich systems.

1121 Using a similar method to that for H₂O discussed above, we calculate satura-
 1122 tion pressures for the composition of a Fuego melt inclusion from Lloyd et al. (2013)
 1123 with varying CO₂ and H₂O contents. The mean melt inclusion glass CO₂ content
 1124 from this melt inclusion suite was 340 ppm (range of 59–786 ppm). However, Raman
 1125 analyses of vapour bubbles in the same sample set by L. R. Moore et al. (2015) re-
 1126 veals that 993–4776 ppm of CO₂ has migrated from the glass phase into the vapour
 1127 bubble following melt inclusion entrapment. Thus, we calculate saturation pressures
 1128 for CO₂ contents between 0–5000 ppm at 1000°C for 2, 4 and 6 wt% H₂O respec-
 1129 tively (after Plank et al., 2013).

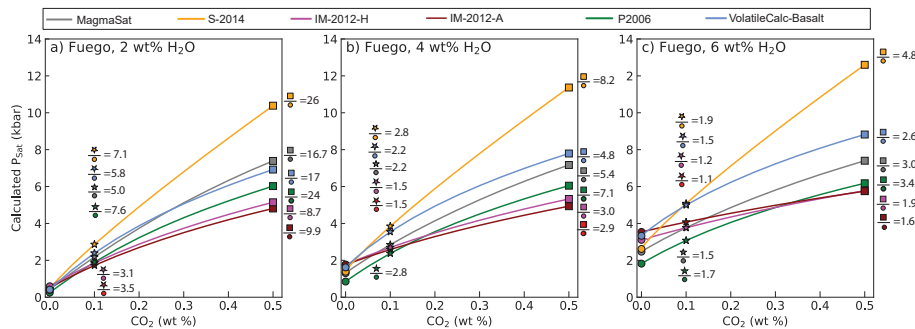


Figure 12. Relationship between saturation pressures and melt CO₂ contents for H₂O-rich melts (using the composition of a Fuego melt inclusion at 1000°C; Table 1). Three different melt H₂O contents (2, 4 and 6 wt%) are shown in part a, b and c) respectively. The numbers on the graphs show the saturation pressure at 5000 ppm CO₂ (square symbol) divided by the saturation pressure at 0 ppm CO₂ (circle), and the saturation pressure at 1000 ppm (star symbol) divided by the saturation pressure at 0 ppm CO₂ (circle) for each model.

1130 S-2014 is most sensitive to CO₂ content, and IM-2012-H and -A the least
1131 sensitive. With increasing H₂O, the change in saturation pressure with increasing
1132 CO₂ becomes smaller, but is still significant (Fig. 12). For example, calculating a
1133 H₂O-only saturation pressure for a melt inclusion with H₂O=6 wt% in MagmaSat
1134 would underestimate magma storage depths by a factor of 1.5 if the melt inclusion
1135 had 1000 ppm CO₂, and a factor of 3 if the inclusion had 5000 ppm CO₂. For a melt
1136 inclusion with 4 wt% H₂O, H₂O-only saturation pressures underestimate by a factor
1137 of ~2.2 for 1000 ppm CO₂, and 5.4 for 5000 pm CO₂. These variations in satura-
1138 tion pressure overwhelm the other errors associated with melt inclusion barometry
1139 (e.g., uncertainty in crustal density profiles, analytical errors associated with volatile
1140 measurements by FTIR or SIMS, differences between solubility models). Further
1141 investigation of the prevalence of CO₂-rich vapour bubbles in arc lavas is clearly
1142 required to have confidence in published barometric estimates in studies which did
1143 not measure the vapour bubbles, or used mineral hygrometers.

1144 Saturation pressures in rhyolitic magmas are also very sensitive to melt CO₂
1145 contents (Fig. 13). For example, saturation pressures calculated for 1000 ppm CO₂
1146 vs. 0 ppm CO₂ differ by factors of 5.7–8.8× for 2 wt% H₂O, and 1.6–2× for 6 wt%
1147 H₂O. Even saturation pressures calculated for 300 ppm CO₂ (0.03 wt%) vs 0 ppm
1148 CO₂ are a factor of ~2–3× higher for 2 wt% H₂O, and 1.2–1.3× higher for 6 wt%
1149 H₂O. The strong effect of CO₂ on saturation pressure is important to recognise
1150 when calculating saturation pressures using only melt H₂O contents, such as studies
1151 using mineral-melt hygrometers (Waters & Lange, 2013), or volatiles-by-difference
1152 methods to estimate H₂O contents of melt inclusions. It is also interesting to note
1153 that, to our knowledge, there are no published Raman measurements of CO₂ in
1154 vapour bubbles which grew after melt inclusion entrapment in dacitic-rhyolitic melt
1155 compositions. While the extremely low CO₂ contents of many rhyolitic melt inclu-
1156 sions are commonly interpreted to result from shallow crustal storage, it is becoming
1157 increasingly recognised that mafic melt inclusions with CO₂ below detection limit
1158 contain large quantities of CO₂ in the vapour bubble (Wieser et al., 2021). Thus, ex-
1159 amination of vapour bubbles in melt inclusions from more silicic systems (e.g., Fig. 1
1160 of Lowenstern, 2001) is likely warranted, to rule out the possibility that these melts
1161 crystallized at greater depths than calculated using measurements of CO₂ hosted in
1162 just the glass phase.

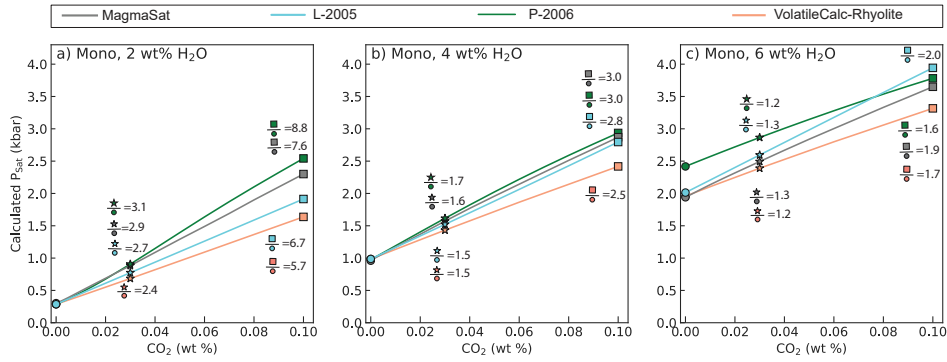


Figure 13. Sensitivity of saturation pressures to melt CO_2 contents at three different H_2O contents (2, 4 and 6 wt%) for the Mono Craters rhyolite. Ratios of saturation pressures at 0.03 wt% CO_2 (300 ppm; star symbol) vs. 0 wt% (circle), and 0.1 wt% (1000 ppm; square symbol) vs. 0 wt% CO_2 are shown on the figure.

1163 5.3 Sensitivity to Temperature

1164 The temperature of the melt at the time of entrapment is another source of un-
 1165 certainty when calculating saturation pressures, as melt or mineral-melt thermome-
 1166 ters are relatively imprecise. For example, the liquid MgO thermometer presented
 1167 in eq. 13 of Putirka (2008) has a standard error of $\pm 71^\circ\text{C}$, while the clinopyroxene-
 1168 liquid thermometer presented in their equation 28b has a standard error of $\pm 48^\circ\text{C}$.
 1169 Changes in the major element compositions of the melt inclusion during PEC and
 1170 diffusive H_2O -loss can also introduce errors when estimating entrapment tempera-
 1171 tures (as most thermometers are highly sensitive to the MgO and H_2O content of
 1172 the melt). Additionally, almost all solubility experiments are performed at supra-
 1173 liquidus conditions, while melt inclusion formation must take place at sub-liquidus
 1174 conditions, so extrapolation to lower temperatures is an unfortunate necessity.

1175 To investigate the sensitivity of different models to temperature, we calculate
 1176 the 0.5 and 2 kbar isobars for the MORB1 composition at 1000°C and 1400°C . Only
 1177 S-2014 shows no temperature dependency, because there is neither a temperature
 1178 or fugacity term in their equations. Interestingly, there is considerable disagree-
 1179 ment between the other models as to whether a hotter magma dissolves more or less
 1180 volatiles. MagmaSat and P-2006 predict an increase in pure CO_2 solubility with
 1181 increasing temperature, while VolatileCalc-Basalt and IM-2012-A and -H predict a

1182 much smaller decrease (Fig. 14a-c). In all models but IM-2012-A, isobars calculated
1183 for lower temperatures intercept the x axis ($\text{CO}_2=0$ wt%) at higher H_2O contents,
1184 so the temperature dependency of H_2O solubility is opposite to that for CO_2 solu-
1185 bility. To visualize the effect of these trends on calculated saturation pressures for
1186 the MORB1 composition, the calculated saturation pressures for melts with volatile
1187 contents represented by the yellow and cyan stars on Figure 14b are plotted against
1188 temperature (between 1000–1400°C; Fig. 14c-d). MagmaSat and P-2006 show the
1189 strongest temperature sensitivity, with a slope opposite to that of the more subtle
1190 changes predicted by VolatileCalc-Basalt and IM-2012.

1191 The lack of consensus as to whether increasing temperature increases or de-
1192 creases the solubility of H_2O and CO_2 indicates that this effect is relatively subtle,
1193 and overwhelmed by analytical errors associated with measuring experimental prod-
1194 ucts (and other sources of experimental scatter; e.g., Fig. 16a-b). This makes it
1195 very difficult for empirical models to fully constrain the temperature sensitivity,
1196 particularly given that the experiments conducted by any given study are usually
1197 performed at a single temperature. For example, all the experiments used to cali-
1198 brate the VolatileCalc-Basalt model were conducted at 1200°C, so the temperature
1199 dependency of this model results from the fugacity function, and $1/T$ terms from
1200 Dixon et al. (1995), rather than experimental observations.

1201 IM-2012 is calibrated on experiments mostly performed at 1200–1300°C (with
1202 a few spanning 1100–1400°C). Their empirical expressions contain $C_{\text{H}_2\text{O}} \times \frac{P}{T}$ and
1203 $C_{\text{CO}_2} \times \frac{P}{T}$ terms in their expressions for H_2O and CO_2 solubility respectively (equa-
1204 tion 11 and 15), where $C_{\text{H}_2\text{O}}$ and C_{CO_2} are empirically-derived constants, and P
1205 and T are pressure and temperature. In the hydrous model, $C_{\text{H}_2\text{O}}$ is negative (-
1206 0.02 ± 0.02), so H_2O solubility increases with increasing temperature, while in the
1207 anhydrous model $C_{\text{H}_2\text{O}}$ is positive (0.02 ± 0.02), so H_2O solubility decreases with
1208 increasing temperature (Fig. 14). As the magnitude of these coefficients is small, the
1209 temperature effect on H_2O solubility is small, and only visible at higher pressures
1210 (because of the P part of these terms; Fig. 14a vs. c). It is also worth noting that
1211 these coefficients in both models are within error of zero, showing that the experi-
1212 mental dataset used to calibrate this model showed very little evidence for a change
1213 in H_2O solubility with temperature. In both the hydrous and anhydrous models,

1214 C_{CO_2} is positive (0.12 ± 0.02 and 0.14 ± 0.02 respectively) and larger in magnitude
1215 than C_{H_2O} , so CO_2 solubility decreases with increasing temperature (see Fig. 14c).

1216 The approach taken by S-2014 and A-2019 is an interesting alternative when
1217 constructing solubility models. While S-2014 is calibrated on experiments conducted
1218 between $1200\text{--}1300^\circ\text{C}$ for CO_2 , and $1200\text{--}1250^\circ\text{C}$ for H_2O , their solubility equa-
1219 tions contain no temperature or fugacity term. Instead, these authors suggest that
1220 the H_2O model should ideally be used between $1150\text{--}1250^\circ\text{C}$. They perform addi-
1221 tional tests on experiments between $1050\text{--}1400^\circ\text{C}$ not used in the calibration, and
1222 show that their model predicts H_2O solubility within $\pm 10\%$ for 78% of experiments
1223 for this wider temperature range. The S-2014 testing dataset for CO_2 only has a
1224 slightly different temperature range than the calibration dataset ($1170\text{--}1250^\circ\text{C}$ vs.
1225 $1200\text{--}1250^\circ\text{C}$), so they do not suggest an expanded temperature range for CO_2 . Sim-
1226 ilarly, the spreadsheet for A-2019 (and the implementation of this model in VESI-
1227 cal) performs all calculations at 1200°C , regardless of the user-input temperature.
1228 Allison et al. (2019) suggest that this approach is likely valid between $1000\text{--}1400^\circ\text{C}$.

1229 Unlike empirical models, the temperature sensitivity of P-2006 and MagmaSat
1230 arises from the entropy differences between melt and fluid components. Given the
1231 limited experimental evidence for changes in solubility with temperature, the direc-
1232 tionality inferred by thermodynamical models is more likely to be correct, as the
1233 relative entropy differences between components are easier to constrain than decon-
1234 voluting subtle differences between the solubility of CO_2 and H_2O in experiments
1235 run at different temperatures, and because all empirical models are being extrapo-
1236 lated to lower temperatures than the supra-liquidus experiments used to calibrate
1237 them. However, the fact that P-2006 doesn't account for volatile speciation for ei-
1238 ther H_2O or CO_2 , and MagmaSat doesn't account for the two H_2O species in the
1239 melt means that these thermodynamic temperature sensitivities may also need further
1240 interrogation.

1241 Overall, although the differences between models is interesting, and important
1242 to recognise when extrapolating beyond the range of the calibration dataset, the
1243 uncertainty that temperature variations introduce to saturation pressure calcula-
1244 tions are relatively small for mafic melts. For example, an uncertainty in the initial
1245 entrapment temperature of $\pm 100^\circ\text{C}$ introduces an uncertainty similar to that asso-

1246 ciated with in-situ measurements of melt inclusion volatile contents ($\pm 5\text{--}10\%$; Fig.
 1247 14).

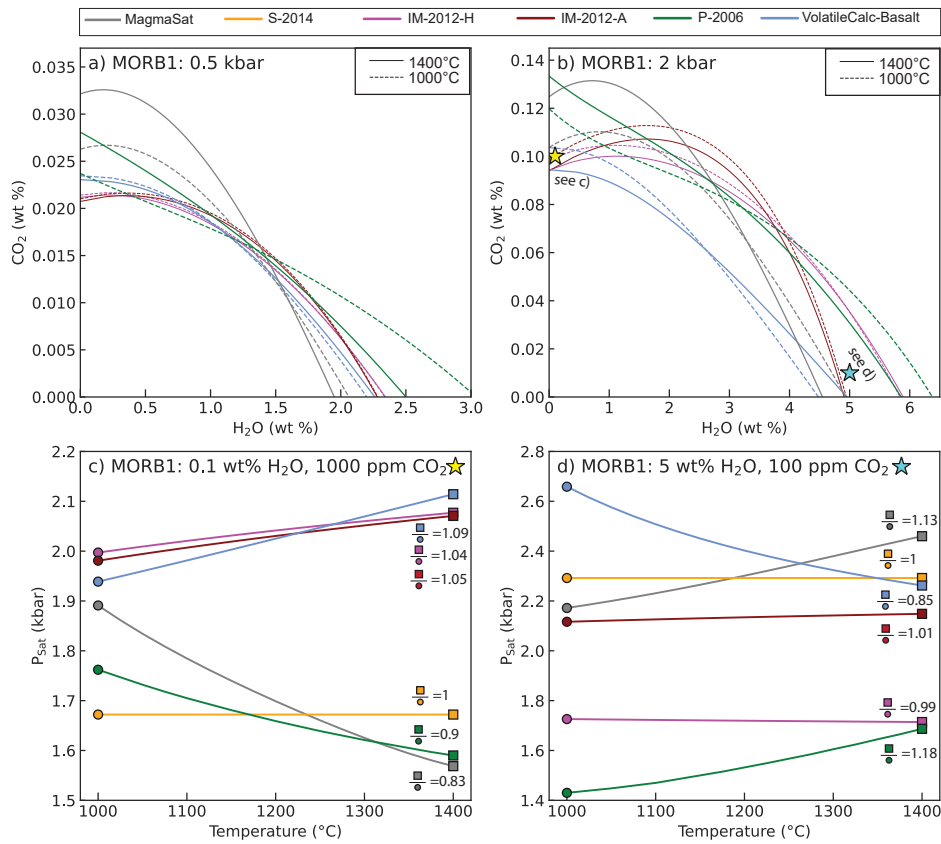


Figure 14. Evaluating model sensitivity to temperature (using the MORB1 composition).
 a-b) Isobars evaluated at 1000 and 1400°C and 0.5 and 2 kbar. c) Relationship between saturation
 pressure and temperature for a melt with 1000 ppm CO₂, 0.1 wt% H₂O (yellow star on a),
 d) 100 ppm CO₂, 5 wt% H₂O (cyan star on b). Ratios of saturation pressures at 1400°C (square
 symbol) to 1000°C (circle symbol) are shown on the figure.

1248 Similarly, temperature sensitivity in rhyolitic melts was evaluated by calcu-
 1249 lating isobars at 0.5 and 2 kbar for 700 and 900°C using the Mono Craters rhyolite
 1250 composition. As for the basaltic example, the directionality and magnitude of effect
 1251 of temperature on saturation pressures for melts with volatile contents indicated by
 1252 the colored stars is shown in Fig. 15c-d for temperatures between 700 and 1000°C.
 1253 VolatileCalc-Rhyolite shows the strongest temperature sensitivity, predicting that
 1254 the solubility of CO₂ decreases with increasing temperature. L-2005 also predicts
 1255 decreasing CO₂ solubility with increasing temperature, although this effect is smaller

1256 than in VolatileCalc-Rhyolite. Decreasing solubility of molecular CO₂ with increas-
 1257 ing temperature was demonstrated experimentally by Fogel and Rutherford (1990).
 1258 In contrast, the two thermodynamic models, P-2006 and MagmaSat, predict that
 1259 pure CO₂ solubility increases with increasing temperature. VolatileCalc-Rhyolite
 1260 also predicts that H₂O solubility decreases with increasing temperature, but the
 1261 effect is smaller than for CO₂.

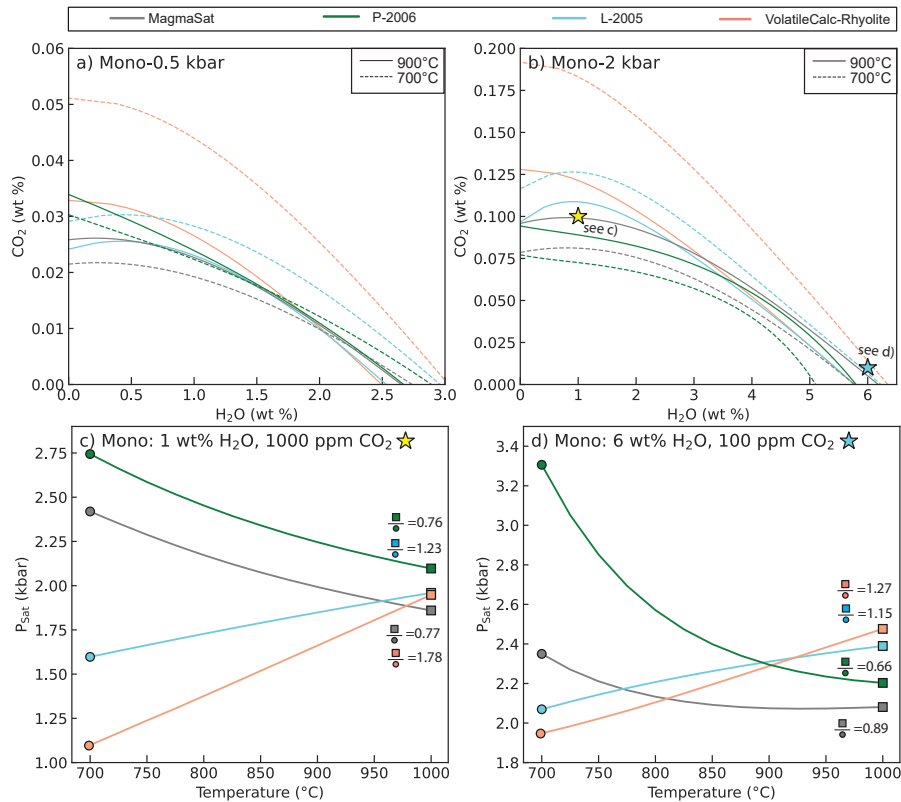


Figure 15. Sensitivity of saturation pressures for the Mono Craters rhyolite to temperature. a-b) Isobars calculated for different solubility models at 700 and 900°C and 0.5 and 2 kbar. c) Relationship between saturation pressure and temperature for a melt with 1000 ppm CO₂, 1 wt% H₂O (yellow star in b), d) 100 ppm CO₂, 6 wt% H₂O (cyan star in b). Ratios of saturation pressures at 900°C (square symbol) to 700°C (circle symbol) are shown on the figure.

1262 It is noteworthy that the temperature sensitivity of CO₂ solubility predicted
 1263 by L-2005 and VolatileCalc-Rhyolite is much greater than that shown by any of the
 1264 basaltic models (Fig. 14d-e vs. Fig 15d-e), and significant considering other sources
 1265 of error associated with saturation pressure calculations. MagmaSat and P-2006 also

1266 show a far greater sensitivity to H₂O solubility between 700–850°C in rhyolites than
1267 any of the basaltic models between 1000–1400°C (Fig. 14f vs. Fig 15f), although the
1268 sensitivity decreases between 800–900°C.

1269 Given the contrasting behaviour of empirical and thermodynamic models,
1270 and the relatively strong effect of temperature in rhyolitic melts, we suggest that
1271 users proceed with caution when extrapolating empirical models to temperatures
1272 significantly lower or higher than the calibration temperature of each model. It may
1273 be best to use empirical models at the calibration temperature (e.g., 1200°C for
1274 VolatileCalc-Basalt, 850°C for VolatileCalc-Rhyolite), which is the approach used by
1275 in the models of S-2014 and A-2019, rather than introduce a temperature sensitivity
1276 with the wrong sign. This is discussed in further detail for VolatileCalc-Rhyolite in
1277 section 6.

1278 **6 Intermediate Compositions**

1279 In this section, we compare the predictions of different solubility models for in-
1280 termediate melt compositions (andesites to dacites). Lavas with these compositions
1281 are dominant within subduction zones, and volcanoes erupting these compositions
1282 are extremely hazardous. Yet, there is a notable paucity of solubility experiments
1283 for andesitic and dacitic compositions relative to basalts and rhyolites (Fig. 2; King
1284 & Holloway, 2002; Botcharnikov et al., 2006). This section builds on the sensitiv-
1285 ity tests performed in section 5 to evaluate possible discrepancies between model
1286 outputs and experimental constraints.

1287 The calibration dataset of MagmaSat has the broadest coverage of andesitic-
1288 dacitic compositions of all the models described here (although it is far from exten-
1289 sive). While there are a number of pure H₂O experiments, MagmaSat only includes
1290 one pure CO₂ experiment on an andesitic melt (conducted at 1 GPa; King & Hol-
1291 loway, 2002), and no pure CO₂ experiments on dacitic melts. Similarly for mixed
1292 H₂O-CO₂, the calibration dataset for andesitic melts includes only four experiments
1293 from King and Holloway (2002), 21 from Botcharnikov et al. (2006) and three from
1294 Botcharnikov et al. (2007). Dacitic liquids are represented by the 12 experiments
1295 on mixed H₂O-CO₂ solubility by Behrens et al. (2004). As the P-2006 model had a
1296 decade fewer experimental constraints available for calibration, it only includes the

1297 one pure CO₂ and four mixed H₂O-CO₂ andesitic experiments of King and Holloway
1298 (2002). The IM-2012 model includes two pure H₂O experiments that lie within the
1299 andesite field on a TAS diagram, but no H₂O-CO₂ experiments, and no experiments
1300 in the dacitic field. None of the other models contain any andesitic or dacitic melts
1301 in their calibration datasets.

1302 **6.1 Comparing solubility models to experimental products**

1303 The suitability of different solubility models for andesitic-dacitic compositions
1304 can be evaluated by calculating isobars using the melt compositions, pressures and
1305 temperatures of different experimental studies, and comparing these isobars to mea-
1306 surements of dissolved volatile contents in experimental products (similar to the
1307 method used in the supplementary material of Ghiorso & Gualda, 2015). The 2
1308 and 5 kbar andesitic experiments of Botcharnikov et al. (2006) are shown in Fig.
1309 16a-b, the 1, 2, and 5 kbar dacitic experiments of Behrens et al. (2004) are shown in
1310 Fig. 16c-e, and the 10 kbar andesite experiments of King and Holloway (2002) are
1311 shown in Fig. 16f. Additional isobar diagrams for the 3–12 kbar basaltic-andesite
1312 experiments of Mangan et al. (2021) are shown in the Supporting Information.

1313 Isobar diagrams show that S-2014 significantly underpredicts CO₂ for all ex-
1314 periments except the most H₂O-poor composition of King and Holloway (2002).
1315 L-2005, VolatileCalc-Basalt and -Rhyolite also mostly plot to lower CO₂ contents
1316 than experimental products. IM-2012-H and -A do a reasonable job of recreating
1317 the most H₂O-poor experiments at <5 kbar, but curve rapidly down to intercept the
1318 x axis at lower H₂O contents than experimental products and other models. Mag-
1319 maSat is a good match to experimental data in Fig. 16d, e and f, but plots to lower
1320 CO₂ contents than experiments in Fig. 16 a, b and c. Using Fe³⁺ proportions best
1321 representing the experimental conditions, P-2006 only passes through experimental
1322 data on Figs. 16a-b, and e, and plots to significantly lower CO₂ contents than exper-
1323 iments (lower than MagmaSat) on Fig. 16c and d. P-2006 is a better match to most
1324 experiments if Fe³⁺/Fe_T=0, but overpredicts CO₂ solubility at 10 kbar for all redox
1325 states. Interestingly, none of the available models recreate the near-flat trajectory of
1326 dissolved CO₂ contents with increasing H₂O from Botcharnikov et al. (2006).

1327 The underprediction of CO₂ solubility by S-2014 is a good example of the
1328 dangers of extrapolating models accounting for the effect of melt composition using
1329 empirical expressions beyond the compositional range of the calibration dataset. The
1330 S-2014 model expresses CO₂ solubility as a function of the composition parameter,
1331 Π^* , with CO₂ solubility increasing as an exponential function of Π^* at a given pres-
1332 sure (equation 16). The melt compositions for the three sets of experimental studies
1333 shown in Fig. 16 all plot to much lower Π^* values than any of the melts in the cal-
1334 ibration dataset (orange diamonds; Fig. 17a). These low Π^* values mean that the
1335 S-2014 model predicts very low CO₂ solubilities. However, CO₂ solubility for melts
1336 with Π^* values outside the range of the calibration dataset may not follow the same
1337 exponential function of this parameter as melt compositions within the calibration
1338 range. Additionally, the exponential dependency of CO₂ solubility on Π^* incorpo-
1339 rated by S-2014 likely breaks down in more evolved melts, because Π^* represents the
1340 ability of the melt to form carbonate-bearing species, while more evolved melts con-
1341 tain increasing proportions of molecular CO₂ (Shishkina et al., 2014). For example,
1342 the proportion of molecular CO₂ to carbonate species varies between 0–4 wt% in the
1343 experiments of Botcharnikov et al. (2006), and 3–30 wt% in the dacitic experiments
1344 of Behrens et al. (2004).

1345 VolatileCalc-Basalt and VolatileCalc-Rhyolite underpredict CO₂ solubility
1346 for all intermediate experiments, with VolatileCalc-Rhyolite predicting lower pure
1347 CO₂ solubility than VolatileCalc-Basalt. This is noteworthy, because many publi-
1348 cations have calculated saturation pressures for andesitic and dacitic melts using
1349 VolatileCalc-Rhyolite (e.g., Blundy et al., 2006; Atlas et al., 2006; Cassidy et al.,
1350 2015; Koleszar et al., 2012). In the original publication, Newman and Lowenstern
1351 (2002) state: “because many andesites contain rhyolitic interstitial melt, Volatile-
1352 Calc may also be applicable to these intermediate compositions.” However, this
1353 should not be taken to suggest that VolatileCalc-Rhyolite is safely extrapolated to
1354 andesitic-dacitic melts. Instead, this statement is referring to the fact that many
1355 lavas with andesitic bulk compositions have rhyolitic groundmass/melt inclusion
1356 compositions (e.g., Tamura & Tatsumi, 2002; Reubi & Blundy, 2009), where
1357 VolatileCalc-Rhyolite may be applicable. Interestingly, VolatileCalc-Rhyolite iso-
1358 bars calculated for the reference temperature of this model (850°C) rather than
1359 the experimental temperature are a good match to experimental data at < 5 kbar

1360 (see Supporting Fig. S3). Thus, the main failure of this model in intermediate com-
1361 positions appears to result from the fact that this model is extremely sensitive to
1362 temperature, and these melts have much higher temperatures than the experiments
1363 used to calibrate this model. This supports our suggestion in section 4.2.1 that it
1364 may be better run models at their reference temperature, rather than extrapolate
1365 beyond the calibration range.

1366 It is also worth noting that all these experimental products have negative val-
1367 ues of the Dixon Π parameter (equation 2). As highlighted by G. Moore (2008),
1368 the full Π expression of Dixon (1997) cannot be used to calculate CO_2 solubility in
1369 calc-alkaline lavas, because Π is negative (yielding a negative solubility of CO_2 ; Fig.
1370 17).

1371 Differences between experimental data and isobars from IM-2012-H and -A are
1372 more complicated, because the discrepancies between models and experiments are
1373 very dependent on the pressure. For example, at 1 kbar, IM-2012-H and -A under-
1374 predict H_2O and CO_2 solubility relative to the experiments of Behrens et al. (2004),
1375 while at 5 kbar, they overpredict CO_2 solubility, but underpredict H_2O solubility
1376 (Fig. 16c vs.e). These discrepancies likely reflect this model being extrapolated
1377 towards the limits of its calibration dataset in terms of both pressure (most exper-
1378 iments were conducted at <5 kbar) and melt composition (Fig. 17, see the next
1379 section for more discussion).

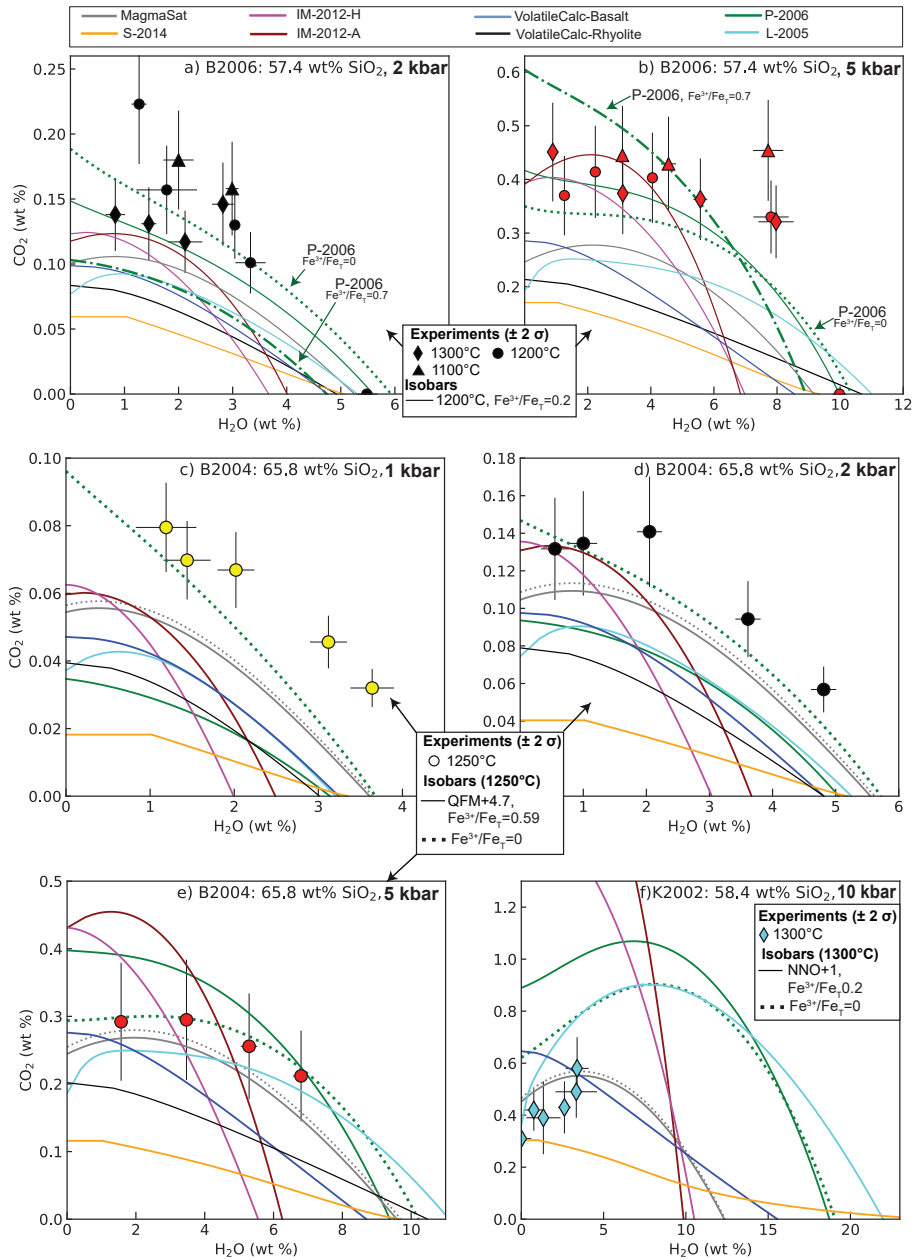


Figure 16. Assessing model fits to experimental data for andesitic and dacitic compositions a-b) Experiments from Botcharnikov et al. (2006). Isobars were calculated for 1200°C and $\text{Fe}^{3+}/\text{Fe}_T=0.2$ ($\sim\text{QFM}+1.5$). P-2006 isobars are also shown for $\text{Fe}^{3+}/\text{Fe}_T=0.7$ (the upper estimate of $\text{Fe}^{3+}/\text{Fe}_T$ in experimental products; dash-dotted line), and $\text{Fe}^{3+}/\text{Fe}_T=0$ (dotted line) c-e) Experiments from Behrens et al. (2004). Isobars are shown for $\text{Fe}^{3+}/\text{Fe}_T=0.59$ (f_{O_2} of $\text{QFM}+4.7$). For P-2006 and MagmaSat, isobars are also shown for $\text{Fe}^{3+}/\text{Fe}_T=0$. f) Experiments from King and Holloway (2002). Isobars are shown for $\text{Fe}^{3+}/\text{Fe}_T=0.2$. For P-2006 and MagmaSat, isobars are also shown for $\text{Fe}^{3+}/\text{Fe}_T=0$. VolatileCalc-Rhyolite isobars are not shown, as the spreadsheet doesn't calculate isobars above 5 kbar. Error bars on all plots shows the 2σ uncertainties from measurements of volatile contents in experimental products. $\text{Fe}^{3+}/\text{Fe}_T$ ratios were calculated from author-stated buffers using MELTS for Excel (Gualda & Ghiorsio, 2015).

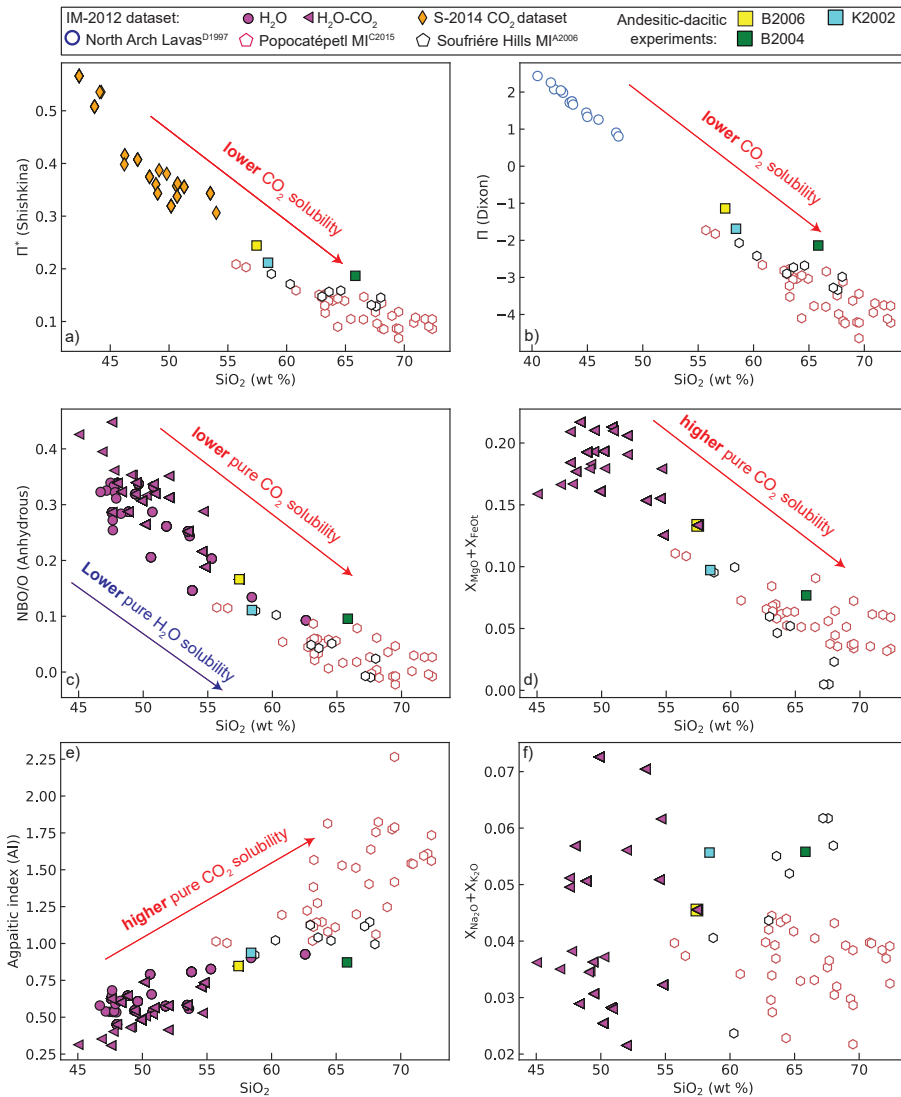


Figure 17. Comparing the calibration datasets of S-2014 and IM-2012 to the andesitic experiments of Botcharnikov et al. (2006), (B2006), Behrens et al. (2004), (B2004) and King and Holloway (2002), (K2002) shown in Fig. 16, and the melt inclusions from Popocatepetl (Atlas et al., 2006) and Soufrière Hills (Cassidy et al., 2015) shown in Fig. 18. Anhydrous molar fractions are used to calculate compositional parameters in parts c-f, because when accounting for discrepancies between isobars (e.g., on Fig. 18, the H₂O content and therefore hydrous cation fractions vary as a function of the pressure).

1380 The fact that no model passes through all available experiments demonstrates
1381 that further investigation of solubility in andesitic to dacitic melts is warranted.
1382 Using representative experimental $\text{Fe}^{3+}/\text{Fe}_T$ ratios, MagmaSat is the most accurate
1383 model, predicting dissolved volatile contents within $\sim 20\%$ of experimental products
1384 (considering reported error bars on dissolved volatile contents).

1385 The extreme sensitivity to the $\text{Fe}^{3+}/\text{Fe}_T$ ratio makes it very difficult to assess
1386 the accuracy of the P-2006 model (particularly given the relatively large uncertain-
1387 ties in the oxygen fugacity of experimental run products; King & Holloway, 2002;
1388 Botcharnikov et al., 2006). In all of the examples shown, P-2006 isobars calculated
1389 for $\text{Fe}^{3+}/\text{Fe}_T=0$ are a better fit to the experimental data than isobars calculated us-
1390 ing estimates of the $\text{Fe}^{3+}/\text{Fe}_T$ ratio of experiments. This suggests that, in relatively
1391 oxidising intermediate melts, P-2006 is overestimating the effect of Fe^{3+} species on
1392 volatile solubility. It is noteworthy that P-2006 is a particularly poor match to the
1393 high pressure andesitic experiments of King and Holloway (2002), despite the fact
1394 that these are the only intermediate experiments in the calibration dataset of this
1395 model.

1396 As all the experiments shown were used to calibrate MagmaSat, similar anal-
1397 ysis applied to new experimental data on andesitic compositions when it becomes
1398 available will provide further constraints on the accuracy of this model. Isobars for
1399 recent solubility experiments on a basaltic-andesite at 4–12 kbar by Mangan et al.
1400 (2021) are shown in Supporting Fig. S4 and S5. MagmaSat is a much better fit
1401 to this new data than P-2006, with experiments performed 400–815 MPa plotting
1402 within error of calculated MagmaSat isobars. In contrast, P-2006 overpredicts CO_2
1403 solubility (regardless of $\text{Fe}^{3+}/\text{Fe}_T$) at <600 MPa.

1404 **6.2 Case Study: Intermediate melt inclusions**

1405 To assess the impact of these model differences on the depths of magma stor-
1406 age reservoirs inferred from melt inclusions in volcanic arcs, we calculate saturation
1407 pressures using a variety of models for two suites of melt inclusions with andesitic-
1408 dacitic liquid compositions: 1) 34 melt inclusions from Volcán Popocatepetl, Mexico
1409 with 55.7–73.4 wt% SiO_2 (Figs. 2, 18a; Atlas et al., 2006), and 2) 8 melt inclusions
1410 from Soufrière Hills Volcano, Montserrat with 58.7–68.0 wt% SiO_2 (Figs. 2, 18b;

1411 Cassidy et al., 2015). Both studies calculated saturation pressures (and therefore
1412 magma storage depths) using VolatileCalc-Rhyolite.

1413 Cumulative frequency distributions for the Popocatepetl melt inclusions (Fig.
1414 18a) shows that P-2006 predicts the lowest saturation pressures, and S-2014 the
1415 highest, with MagmaSat, IM-2012-A, VolatileCalc-Basalt, VolatileCalc-Rhyolite,
1416 and IM-2012-H lying in-between these model extremes. Based on our analysis in
1417 the previous section suggesting that MagmaSat is the best calibrated model for
1418 intermediate melt compositions, we ratio saturation pressures from each model to
1419 those determined using MagmaSat (allowing model differences to be quantified).
1420 Additionally, because MagmaSat is a thermodynamic model that has been shown to
1421 work well for basaltic and rhyolitic compositions, it is effectively being interpolated
1422 to andesitic-dacitic compositions which are not represented in its calibration dataset
1423 (i.e., these melt inclusion compositions), rather than extrapolated (as for empiri-
1424 cal models such as S-2014, VolatileCalc-Basalt, and IM-2012 which are primarily
1425 calibrated on more mafic melt compositions; Fig. 2).

1426 The median saturation pressure for Popocatepetl melt inclusions calculated
1427 for VolatileCalc-Rhyolite is $1.26\times$ higher than for MagmaSat. The median for Mag-
1428 maSat is $\sim 1.2\times$ higher than for P-2006. The deviation relative to MagmaSat in-
1429 creases with SiO_2 content for VolatileCalc-Rhyolite (~ 1.1 to $1.5\times$), VolatileCalc-
1430 Basalt (~ 1 to $1.35\times$), and L-2005 (~ 1 to $1.4\times$). The deviation between S-2014
1431 and MagmaSat is very large, increasing from a factor of 2 at ~ 55 wt% SiO_2 to
1432 $\sim 5.5\times$ at 72.5 wt% SiO_2 . The deviation between IM-2012-H and -A and P-2006
1433 vs. MagmaSat shows no clear correlation with SiO_2 content (Supporting Fig. S6).
1434 The presence of discrepancies which correlate with melt composition is particularly
1435 concerning, because it means that choice of an inappropriate solubility model may
1436 introduce systematic error into a dataset as a function of melt inclusion composition.

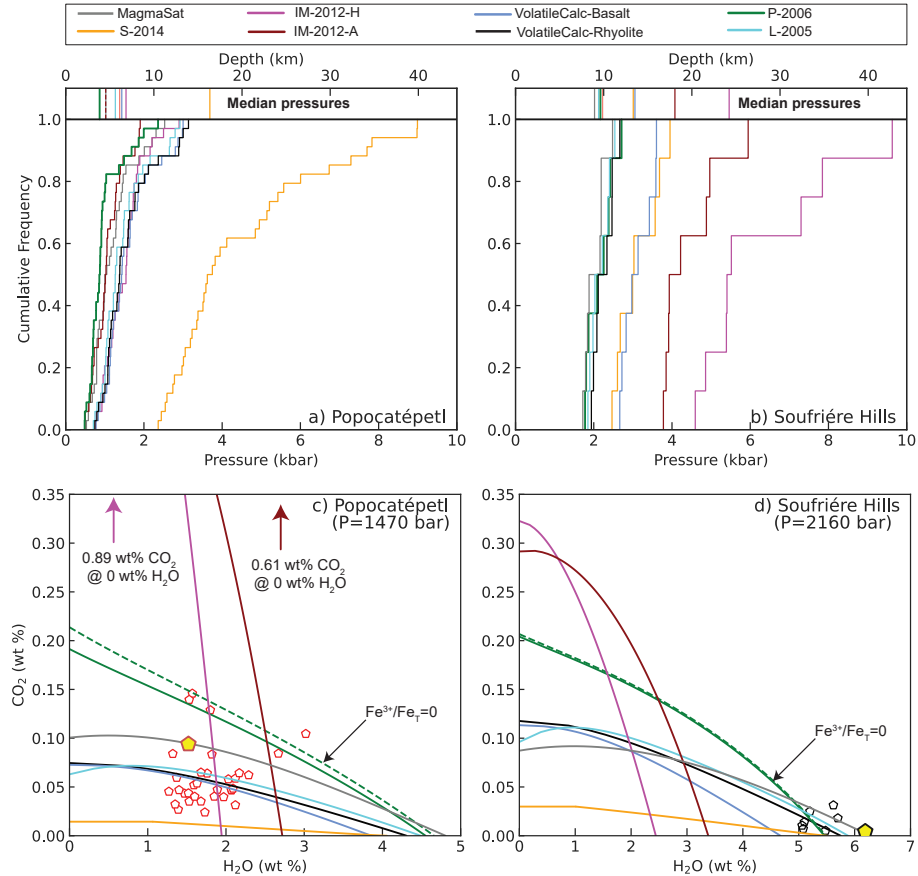


Figure 18. a-b) Cumulative distribution functions of saturation pressures from different models for melt inclusions from a) Popocatépetl (Atlas et al., 2006) and b) Soufrière Hills (Cassidy et al., 2015). $\text{Fe}^{3+}/\text{Fe}_T$ was set to 0.15. c) Isobars from different models calculated at the saturation pressure from MagmaSat (1470 bar) for the Popocatépetl melt inclusion shown with a yellow pentagon (at 1050°C following Atlas et al., 2006). The scale is trimmed to emphasize the differences between models at lower CO₂ contents, with the interception of the IM-2012 isobars with the y axis labelled on the plot. d) Isobars from different models calculated at the saturation pressure from MagmaSat (2160 bar) for the Soufrière Hills melt inclusion shown with a yellow pentagon (at 1000°C following Cassidy et al., 2015). Isobars are also shown for P-2006 with $\text{Fe}^{3+}/\text{Fe}_T=0$ (dotted line)

1437 MagmaSat predicts the lowest saturation pressures for the Soufrière Hills melt
 1438 inclusions, with L-2005, P-2006, and VolatileCalc-Rhyolite predicting reasonably
 1439 similar pressures. VolatileCalc-Basalt, S-2014 and IM-2012-A and -H are offset

1440 to higher pressures. Similar to the results for Popocatépetl, the ratio of saturation
1441 pressures for Soufrière Hills melt inclusions relative to MagmaSat for L-2005 (~ 1
1442 to $1.1\times$), VolatileCalc-Basalt (~ 1.25 to $1.35\times$) and VolatileCalc-Rhyolite (~ 1.05
1443 to $1.17\times$) increase with increasing SiO_2 (Supporting Fig. S7). Unlike Popocatépetl
1444 melt inclusions, the discrepancy between IM-2012 and MagmaSat increases dra-
1445 matically with increasing SiO_2 (from ~ 1.5 to $2.5\times$ for anhydrous, and 2 to $4.5\times$ for
1446 hydrous), while that for S-2014 shows a weak negative correlation with SiO_2 (from
1447 ~ 1.7 – $1.35\times$).

1448 The large discrepancies shown by IM-2012 (for Soufrière Hills) and S-2014 (for
1449 Popocatépetl) are best understood by examining an isobar calculated for the inclu-
1450 sion showing the largest deviation relative to MagmaSat in each dataset ($\text{SiO}_2=72.4$
1451 wt% for Popocatépetl, and 67.6 wt% for Soufrière Hills; yellow pentagon on Fig.
1452 18c-d) at the saturation pressure obtained from MagmaSat. For both sets of inclu-
1453 sions, S-2014 isobars intercept the x axis at similar H_2O contents to other models,
1454 but intercept the y axis at drastically lower CO_2 contents. This underestimation of
1455 CO_2 solubility likely results from the fact that the Π^* values of these inclusions lie
1456 well below that of the calibration dataset (as discussed for andesitic experiments;
1457 Fig. 17b).

1458 In contrast, IM-2012 predicts very high pure CO_2 solubility, and low pure H_2O
1459 solubility relative to the other models. Both IM-2012 models express the composi-
1460 tional dependence of H_2O solubility in terms of the parameter NBO/O, with melts
1461 with higher NBO/O values having higher H_2O solubility (equation 15). Both sets
1462 of melt inclusions possess much lower NBO/O values than the calibration dataset
1463 of IM-2012 (Fig. 17c-d). This is problematic, because the empirical relationship
1464 between NBO/O and pure H_2O solubility incorporated by IM-2012 has not been
1465 validated for these melt compositions. For example, Shishkina et al. (2014) show
1466 that IM-2012 drastically overestimates H_2O solubility in their basanite and nepheli-
1467 nite melt compositions. They point out that while IM-2012 conclude that there
1468 is only a small effect of melt composition on H_2O solubility, the IM-2012 model
1469 ends up showing a strong sensitivity to melt composition when extrapolated to the
1470 high NBO/O ratio in their basanite and nephelinite melts (and we invoke a similar
1471 explanation for the lower NBO/O ratios in melt inclusions discussed here).

1472 The IM-2012 expression for CO₂ solubility is more complicated, contain-
1473 ing terms for the Agpaitic index (AI), NBO/O, X_{Na₂O+K₂O}, X_{FeO+MgO} and X_{H₂O}
1474 (equation 11). These two sets of melt inclusions have higher AI, lower NBO/O ra-
1475 tios, similar values of X_{Na₂O+K₂O}, and lower X_{FeO+MgO} values than the calibration
1476 dataset (Fig. 17d-f). While the effect of NBO/O is more convoluted because it also
1477 affects the solubility of H₂O (which feeds back into the expression for CO₂), it is
1478 readily apparent that the positive coefficient attached to the AI term combined with
1479 the negative coefficient attached to the MgO+FeO term causes this model to predict
1480 higher CO₂ solubilities than the calibration dataset for the andesitic-dacitic melt
1481 inclusions considered here.

1482 The discrepancy between isobars for S-2014 and IM-2012 relative to Mag-
1483 maSat are relatively similar for the Popocatepetl and Soufrière Hills melt compo-
1484 sitions, while discrepancies for saturation pressures differ markedly (Fig. 18a-b vs.
1485 c-d). This is because the volatile contents of Popocatepetl melt inclusions are sig-
1486 nificantly more CO₂-rich (~0.02–0.15 wt% and higher), and H₂O-poor (~1–3 wt%)
1487 than Soufrière Hills melt inclusions (<0.04 wt% CO₂ and 5–6 wt% H₂O). For this
1488 reason, calculated saturation pressures for Popocatepetl melt inclusions are sensitive
1489 to the treatment of both CO₂ and H₂O in solubility models (Fig. 18b), while those
1490 for Soufrière Hills melt inclusions are mostly sensitive to pure H₂O solubility. Thus,
1491 S-2014 overestimates saturation pressures for Popocatepetl melt inclusions because
1492 this model drastically underestimates the solubility of pure CO₂. In contrast, S-2014
1493 only slightly underestimates H₂O solubility relative to MagmaSat, so only slightly
1494 overpredicts saturation pressures for H₂O-rich Soufrière Hills melt inclusions. The
1495 discrepancy between IM-2012 and MagmaSat is much smaller for Popocatepetl rel-
1496 ative to Soufrière Hills because, fortuitously, the IM-2012-H isobar intercepts the
1497 MagmaSat isobar at H₂O contents similar to these Popocatepetl melt inclusions.
1498 IM-2012-H and -A drastically underestimates the solubility of pure H₂O, so overes-
1499 timates saturation pressures for the H₂O-rich Soufrière Hills melt inclusions relative
1500 to other models.

1501 It is worth noting that Iacono-Marziano never intended their model to be ap-
1502 plied to andesites, and when discussing the limitations of their model, they explicitly
1503 warn that their empirical expressions poorly incorporates the effect of MgO and FeO
1504 on CO₂ solubility because of the restricted range of these oxides in the calibration

1505 dataset. We have included this discussion as an extreme example of the danger of
1506 extrapolating empirical models beyond their calibration range. However, the sen-
1507 sitivity of this model to the FeO and MgO content of the melt also presents issues
1508 when applied to high MgO basaltic liquids. For example, Wieser et al. (2021) show
1509 that IM-2012 predicts higher saturation pressures for highly primitive (high MgO)
1510 melt inclusions from Kilauea Volcano relative to S-2014 and MagmaSat. This likely
1511 reflects the higher values of $X_{\text{FeO}+\text{MgO}}$ in these melt inclusions relative to the cali-
1512 bration dataset, which causes IM-2012 to predict lower CO₂ solubility (the opposite
1513 directionality to that seen for the intermediate melt inclusions discussed here).

1514 The H₂O-rich nature of Soufrière Hills melt inclusions means that VolatileCalc-
1515 Rhyolite predicts much more similar saturation pressures to MagmaSat (1.07–1.15×;
1516 Supporting Fig. S6) than for Popocatepetl (1.1–1.5× higher; Supporting Fig. S5),
1517 because the main failure of VolatileCalc-Rhyolite for intermediate compositions at
1518 moderate to high temperatures (>850 °C) is its prediction of pure CO₂ solubility
1519 (Figs. 16, 18c-d). The discrepancy for both VolatileCalc models and L-2005 relative
1520 to MagmaSat is significantly smaller than for S-2014 and IM-2012. This is because
1521 the solubility differences during evolution for basaltic to rhyolitic compositions are
1522 relatively small (30–40%) compared to the error associated with the extrapolating
1523 an empirical model far beyond its compositional range. Overall, this case study
1524 shows the importance of checking that the calibration dataset of a model contains
1525 melts similar to those in the sample set of interest, particularly if the effect of melt
1526 composition is parameterized empirically.

1527 **7 Best practices for data visualization and curation**

1528 **7.1 Isobar Diagrams: limitations and alternatives**

1529 As demonstrated by the preceding section, isobar diagrams are a useful tool to
1530 visualize variations in volatile solubility for a specific melt composition. However,
1531 many suites of melt inclusions have considerable major element variability, which
1532 translates into differing solubilities of H₂O-CO₂ at a given pressure, and different
1533 isobar shapes at a given pressure (Wieser et al., 2021; Roggensack, 2001; Iacovino et
1534 al., 2021). We use two suites of melt inclusions to demonstrate this point.

1535 First, we consider a suite of basaltic melt inclusions from Butajira volcanoes in
1536 the Main Ethiopian Rift from Iddon and Edmonds (2020). We calculate isobars for a
1537 representative inclusion composition (BJ08_7; Fig. 19a), and then we compare these
1538 to the isobars calculated for each individual melt inclusion composition at 1 and 3
1539 kbar (Fig. 19a-b). 3 kbar isobars calculated from the composition of each individual
1540 melt inclusion from Butajira (Fig. 19b) cover the entire region of H₂O-CO₂ space
1541 that is bracketed by the 2 and 4 kbar isobars calculated in MagmaSat for the repre-
1542 sentative melt inclusion composition (Fig. 19b vs. a). In fact, saturation pressures
1543 calculated using any given melt inclusion composition vs. the major element compo-
1544 sition of the melt inclusion in question can affect the saturation pressure by almost a
1545 factor of 2. By extension, visual inspection of melt inclusion volatile concentrations
1546 plotted on isobar diagrams may be associated with an error of this magnitude).

1547 Second, we calculate isobars at 300 and 700 bars for a representative subset
1548 of melt inclusions from the 2018 eruption of Kīlauea with PEC-corrected MgO con-
1549 tents between 6.4 to 13.5 wt% (Wieser et al., 2021). Although less extreme than the
1550 Butajira example, the spread of isobars calculated for a single sample at 700 bars
1551 for multiple melt inclusions is wider than the distance between isobars calculated
1552 100 bar apart for a specific melt inclusion. Similar isobar spreads are seen for both
1553 Kīlauea and Butajira using IM-2012 (Supporting Fig. S8 and S9).

1554 VESICAL solves the problem of potentially misleading isobar diagrams by
1555 facilitating rapid calculations of saturation pressures for large suites of melt in-
1556 clusions. For example, calculating saturation pressures for the 33 melt inclusions
1557 in the dataset of Iddon and Edmonds (2020) using VolatileCalc-Basalt, S-2014,
1558 and IM-2012 takes only 4.2 seconds if VESICAL is run on the ENKI server. Mag-
1559 maSat is slightly slower, taking 31.5 seconds (still <1 s per sample). MagmaSat
1560 calculations may run faster if ThermoEngine is installed locally (calculations take
1561 26.3 s using a Dell Inspiron laptop with 16 GB RAM and an Intel-i7 processor, see
1562 <https://gitlab.com/ENKI-portal/ThermoEngine> for installation help).

1563 Once users have calculated saturation pressures for each inclusion, a number of
1564 different x-y plots will provide more information than isobar diagrams. For example,
1565 G. Moore (2008) suggests that users could plot two graphs, one showing melt inclu-
1566 sion CO₂ content against saturation pressure and one showing melt inclusion H₂O

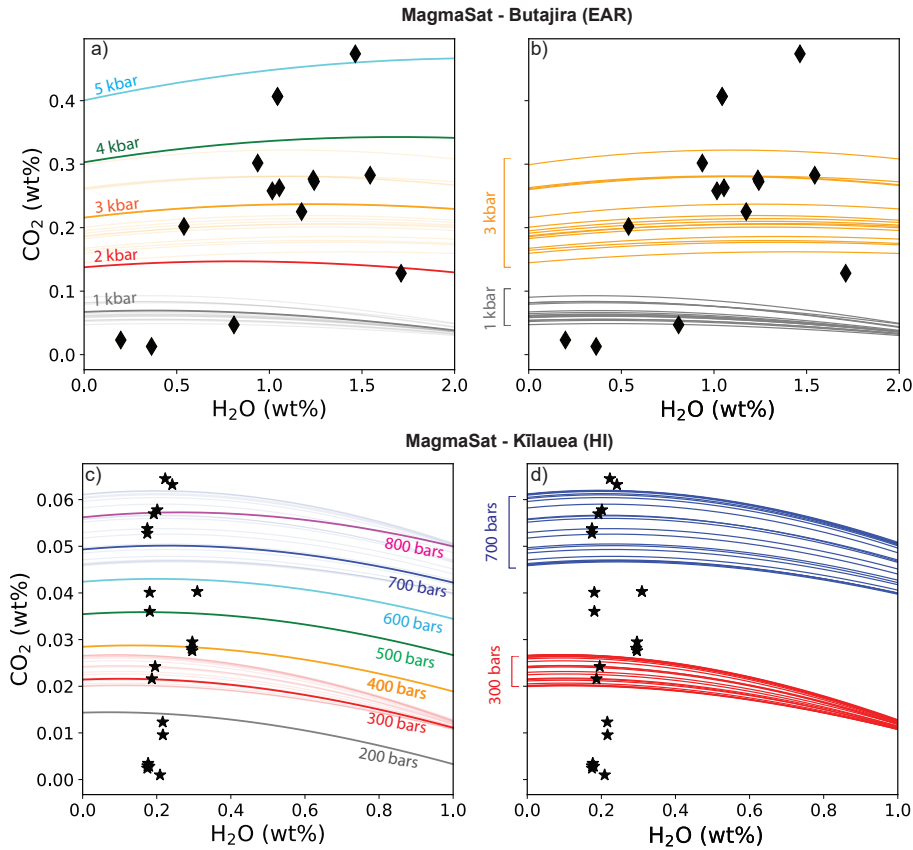


Figure 19. a-b) Isobars for olivine-hosted melt inclusions from Iddon and Edmonds (2020) calculated at 1170°C. a) MagmaSat isobars for melt inclusion BJ08.7 from Butajira with melt inclusion volatile data overlain. b) 1 and 3 kbar isobars calculated for the major element composition of each individual melt inclusion from Butajira (underlain as light lines in a). c-d) As for a-b, but using a representative subset of melt inclusions from Kilauea (Wieser et al., 2021). To save computation time as this study analyses >100 melt inclusions, PEC-corrected compositions were sorted by MgO content, and every 5th inclusion composition was used to calculate an isobar. Isobars are calculated for a temperature calculated from the melt inclusion MgO content using the thermometer of Helz and Thornber (1987).

1567 contents against saturation pressure. This allows clustering of saturation pressures
 1568 to be observed, and determination of the importance of each volatile species when
 1569 calculating saturation pressure. Alternatively, saturation pressures could be plotted
 1570 as histograms, cumulative density functions, or box/violin plots to assess clustering.
 1571 Additionally, the ability to easily filter calculated saturation pressures by additional

1572 variables in python (e.g., host mineral content, amount of post-entrapment crystal-
1573 lization, sample location, stratigraphic height) will help to elucidate the record of
1574 the magmatic plumbing system preserved in different crystal populations. For ex-
1575 ample, Wieser et al. (2021) show that melt inclusions hosted in low forsterite olivine
1576 crystals from Kīlauea Volcano crystallized at $\sim 1\text{--}2$ km depth, while melt inclusions
1577 hosted within higher forsterite olivines crystallized at $\sim 3\text{--}5$ km depth.

1578 **7.2 Assessing Errors**

1579 The ability to calculate saturation pressures using a number of different models
1580 in VESIcal is advantageous, because it can provide assessment of the systematic
1581 errors associated with model choice. If different solubility models produce satura-
1582 tion pressures which are statistically distinguishable using tests such as ANOVA or
1583 the Kolmogorov-Smirnov test, or differences between models exceed 10–20% (the
1584 approximate quoted error on most models), users need to evaluate their melt compo-
1585 sitions, pressures and temperatures in the context of the calibration dataset of each
1586 solubility model. Several Jupyter notebooks aiding these comparisons are provided
1587 alongside VESIcal part I (Iacovino et al., 2021). Additionally, comparisons between
1588 any available experimental data for relevant melt compositions and different solu-
1589 bility models using a workflow similar to that used here for andesites (e.g., isobar
1590 diagrams as in Fig. 16, plots of melt composition vs. calibration datasets) will help
1591 users select a suitable model. As well as examining melt compositions, users should
1592 also evaluate whether they are extrapolating temperature-sensitive models beyond
1593 the calibration range (as discussed here for VolatileCalc-Rhyolite).

1594 In general, if a natural silicate melt composition is poorly represented by ex-
1595 perimental data, MagmaSat is probably the best model to use, as its thermodynamic
1596 nature is more suitable to extrapolation to melt compositions not represented in the
1597 calibration dataset than empirical models such as IM-2012, S-2014, or VolatileCalc-
1598 Basalt. However, the comprehensive nature of MagmaSat means that the fit to
1599 experimental data from any specific region of major element space is compromised
1600 by the fact the model is optimizing the overall fit to many different major element
1601 compositions. Thus, where present, models developed for specific volcanic centres,
1602 or highly weighted towards specific melt compositions (e.g, A-2019 for the 6 cen-
1603 ters they investigate, or IM-2012 for alkaline compositions) may return a better fit.

1604 While these composition-specific models may be well calibrated in terms of melt
1605 composition, users must also check that they are applying the model within the
1606 recommended pressure and temperature range.

1607 VESICAL also opens up the capability to handle errors arising from volatile
1608 solubility modelling using the advanced functionality of Python3 packages such as
1609 Numpy, SciPy and PyMC to perform Bayesian statistical techniques (e.g., Markov
1610 Chain Monte Carlo methods). This means the uncertainty in all input parameters
1611 (e.g., temperature, analytical uncertainties in volatile and major element contents,
1612 uncertainty arising from post-entrapment crystallization corrections) can be prop-
1613 agated into a resulting error distribution for each melt inclusion. These techniques
1614 are increasingly being utilized by igneous petrologists, with recent applications in-
1615 cluding calculating error distributions for diffusion timescales (Mutch et al., 2019),
1616 the contribution of melts from distinct mantle sources (Gleeson et al., 2020), and
1617 propagating uncertainties in vapour bubble growth models (Rasmussen et al., 2020).

1618 **7.3 Data Curation**

1619 Now that VESICAL makes it possible to calculate saturation pressures for large
1620 melt inclusion datasets in short amounts of time, it is vital that data is published
1621 in a way that allows such calculations to be performed retrospectively (e.g., recal-
1622 culating literature saturation pressures from a given volcanic center/region to use a
1623 single solubility model). The concentration of major elements and volatile elements
1624 should be provided within a single spreadsheet or database, ideally alongside the
1625 composition of the mineral host. Additionally, if melt inclusions are corrected for
1626 post-entrapment crystallization (PEC), both raw and corrected major and volatile
1627 element concentrations should be published. Particularly for more chemically-
1628 complex host minerals like pyroxene and plagioclase, it is highly likely that com-
1629 munity standards on the best PEC procedure will change with time. Finally, given
1630 that numerous recent studies have shown that bubble CO₂ contents can change
1631 calculated saturation pressures by up to an order of magnitude (section 5), even if
1632 authors were unable to perform Raman analyses, it should be noted whether each
1633 melt inclusion contained a vapour bubble (and ideally an estimate of the volume
1634 proportion of the vapour bubble). This information may allow the CO₂ contents in
1635 vapour bubbles to be reconstructed theoretically by future studies, given the recent

1636 proliferation of vapour bubble growth models (e.g. Aster et al., 2016; Rasmussen et
1637 al., 2020; MacLennan, 2017).

1638 Proper data curation is particularly vital in the world of volatile solubility
1639 modelling because it is very likely that many more experiments will be published
1640 over the next decade, allowing the creation of new solubility models that are cali-
1641 brated over an even wider region of P-T and compositional space. Many publica-
1642 tions could not be used for comparisons in this study, because there was simply no
1643 way to combine volatile element concentrations and major element concentrations
1644 (which were often reported in different tables with non-unique or non-matching
1645 sample names), or not reported at all. It would be a great shame if published melt
1646 inclusion datasets could not be input into these new models to recalculate saturation
1647 pressures, and gain a greater understanding of magma storage in the Earth's crust.

1648 **8 Future work**

1649 The comparisons drawn in this review highlight several research areas where
1650 further experimental work is required to be able to distinguish which model be-
1651 haviours are accurate. First, significantly more experiments are needed on andesitic-
1652 dacitic melt compositions. Figure 16 shows that it is currently impossible to differ-
1653 entiate a potential failure in any given solubility model from anomalies in any given
1654 set of experiments (e.g., the differential effect of addition of H₂O on CO₂ solubility
1655 in different experiments; Fig. 16b. vs f).

1656 One of the challenges when assessing CO₂ solubility in andesitic-dacitic melts
1657 is the fact that CO₂ is present as both carbonate and molecular CO₂. Carbon
1658 species do appear separately in FTIR spectra, but the accuracy of FTIR-derived
1659 volatile concentrations can be affected by peak overlap (e.g., Brooker et al., 2001b),
1660 as well as uncertainty in peak baseline and absorption coefficients (Botcharnikov et
1661 al., 2006; Mangan et al., 2021). SIMS cannot distinguish different carbon species
1662 (only yields total carbon), but may help to resolve issues with FTIR as a result of
1663 increased understanding of the optimal analysis conditions for volatiles in silicate
1664 glasses of the last few decades. However, in addition to its substantial cost relative
1665 to FTIR, accurate SIMS measurements are reliant on having a suite of standards
1666 with similar major element compositions and a range of volatile contents (and these

1667 standards are often characterized by FTIR, so are subject to the caveats mentioned
1668 above).

1669 Second, the effect of redox on volatile solubility across the range encountered
1670 in terrestrial magmas is still poorly constrained (section 5). This discrepancy largely
1671 reflects the fact that the redox conditions at which many experiments in the litera-
1672 ture were conducted are uncertain and/or highly variable (e.g., Botcharnikov et al.,
1673 2006). Because of this uncertainty, many calibration datasets are built without being
1674 able to constrain the quantities of Fe_2O_3 and FeO for each experimental run. While
1675 our investigation of intermediate melts indicates that the strong sensitivity of CO_2
1676 solubility to melt redox shown by P-2006 is likely anomalous because of the presence
1677 of experiments with extremely high calculated $\text{Fe}^{3+}/\text{Fe}_T$ ratios in the calibration
1678 dataset, further experiments where Fe_2O_3 and FeO proportions are accurately mea-
1679 sured are needed to be certain that this behaviour is not real. It is also noteworthy
1680 that almost all the andesitic experiments were performed at higher oxygen fugacities
1681 than lavas erupted at volcanic arcs. When the calibration dataset for a given set of
1682 compositions is so small, this makes it difficult to deconvolve changes in volatile sol-
1683 ubility with melt composition compared to redox. Recent advances in measurements
1684 of $\text{Fe}^{3+}/\text{Fe}_T$ using Fe K-edge micro-X-ray absorption near-edge structure (XANES)
1685 spectroscopy in hydrous glasses (Cottrell et al., 2018) could provide an avenue to
1686 better constrain this parameter in future (and past) experimental products.

1687 It is also worth noting that all the models discussed here only consider the
1688 effect of redox through terms for Fe^{2+} and Fe^{3+} in the melt, constraining their ap-
1689 plicability to melts more oxidising than the IW buffer. In more reducing conditions,
1690 the co-existing CO_2 -rich phase may be graphite or diamond rather than a CO_2 -rich
1691 vapour phase (Eguchi & Dasgupta, 2018), and the dissolved volatile species may
1692 be CO, CH_4 and H_2 (Mysen et al., 2009). This means that extreme caution is re-
1693 quired when applying these solubility models to highly reducing conditions such as
1694 those found on other planetary bodies (e.g., the Moon, Mars and Mercury; Li et al.,
1695 2017).

1696 Third, there is still significant uncertainty regarding the exact nature of H_2O
1697 and CO_2 mixing at higher pressure. This reflects the difficulty in measuring mixed
1698 H_2O - CO_2 fluids that were in equilibrium with the melt during the experiment. If

1699 measured at all, methods in the literature span from puncture and weight loss of
1700 frozen capsules (i.e., when frozen the CO₂ is released, but not the H₂O; Shishkina
1701 et al., 2010) to more sophisticated and accurate vacuum line manometry (G. Moore
1702 et al., 2008; Iacovino et al., 2013; Allison et al., 2019). New infinite path laser spec-
1703 trometry technology may offer potential improvement of this critical measurement,
1704 but challenges associated with small sample sizes remain. More work determining
1705 the pure CO₂ solubility as a function of pressure and temperature would also be of
1706 great benefit in constraining the behavior of H₂O-poor fluids.

1707 Fourth, we show that the sensitivity of dissolved volatile contents to temper-
1708 ature is highly model-specific. Given the difficulties with constraining temperature
1709 sensitivity experimentally (Iacono-Marziano et al., 2012), we suggest that it may be
1710 best to parametrize future empirical models at a single temperature (e.g., A–2019,
1711 S–2014), or incorporate the temperature sensitivity predicted by thermodynami-
1712 cal models, rather than introduce a spurious temperature dependency which is not
1713 founded in experimental data, nor consistent with the relative entropy of melt and
1714 fluid terms.

1715 Finally, it is worth noting that all of the solubility models discussed only con-
1716 sider H₂O-CO₂ in the vapour phase, while in reality, natural fluids in volcanic sys-
1717 tems may contain relatively large proportions of F, Cl, and S, as well as a separate
1718 brine phase (Botcharnikov et al., 2007). Additionally, at higher pressures and tem-
1719 peratures, significant quantities of major element species will dissolve into a H₂O-
1720 rich fluid (e.g., Si, Na, K), with silicate melt and hydrous fluids becoming completely
1721 miscible above a critical temperature (Bureau & Keppler, 1999). This causes a pure
1722 H₂O model to underestimate the true solubility of H₂O at these conditions. Com-
1723 bined with the fact that it is near-impossible to quench silicate melts with >9±1
1724 wt% H₂O to a glass phase which can be analysed by SIMS or FTIR (Gavrilenko
1725 et al., 2019; Mitchell et al., 2017), quantifying the solubility of H₂O at condition
1726 relevant to lower crustal magma storage will require experimental innovations (e.g.
1727 Makhluף et al., 2020; Mitchell et al., 2017). Models will also need to be developed
1728 which are capable of calculating equilibria between a silicic melt phase and a com-
1729 plex aqueous fluid (Ghiorso & Sverjensky, 2016; Sverjensky et al., 2014; Huang &
1730 Sverjensky, 2019). Recently, a new equation of state for estimating the dielectric
1731 constant of water and new equation of state parameters for major solute species has

1732 enabled thermodynamic mass transfer calculations for fluid-rock systems up to 6
1733 GPa and 1000 ° C (Facq et al., 2014; Debret & Sverjensky, 2017; Huang & Sverjen-
1734 sky, 2019; Sverjensky et al., 2014), significantly advancing our ability to model fluid
1735 behavior in volcanically relevant systems (e.g., Iacovino et al., 2020).

1736 **9 Conclusion**

1737 This review uses the new open-source Python3 tool VESIcal (Iacovino et
1738 al., 2021), in addition to VolatileCalc (Newman & Lowenstern, 2002) and Solw-
1739 cad (Papale et al., 2006) to draw extensive comparisons between the behaviour of
1740 9 different solubility models for a range of melt compositions. We show that these
1741 models predict surprisingly different volatile solubilities, particularly for pure CO₂
1742 or mixed CO₂-H₂O fluids. Even for melt compositions that are well represented in
1743 the calibration datasets of multiple models (e.g., MORBs), calculated solubilities for
1744 pure CO₂ can deviate from one another by factors of ~2. Differential treatment of
1745 H₂O-CO₂ mixing enhances these differences when calculating volatile solubility for
1746 melts containing both volatile species. The solubility of CO₂ predicted by different
1747 rhyolitic models also differs substantially, overwhelming other sources of uncertainty
1748 such as analytical errors on measurements of volatile contents or uncertainties in
1749 crustal density profiles. Differences are most pronounced for peralkaline rhyolites
1750 where there are fewer experimental constraints.

1751 Overall, these comparisons demonstrate that it is vital to pick a model which is
1752 calibrated for the pressure, temperature, and melt composition of interest. Choice of
1753 a poorly calibrated model could introduce a systematic error of a factor of 2 or more
1754 in estimates of saturation pressures. This has widespread implications for published
1755 estimates of magma storage depths within volcanic systems, and indicates that re-
1756 evaluation of published magma storage depths calculated using older models may be
1757 warranted.

1758 We also investigate the sensitivity of different models to variation in parame-
1759 ters such as H₂O content (with relevance to diffusive re-equilibration), CO₂ content
1760 (with relevance to melt inclusion vapour bubble growth), temperature and oxygen
1761 fugacity. We suggest that by performing similar sensitivity tests in the future, the
1762 uncertainties affecting calculations of volatile solubility in magmatic systems (and

1763 therefore the limitations of each study) can be quantified. We also demonstrate that
1764 isobar diagrams are a poor visualization method for determining magma storage
1765 depths in systems where melt inclusions possess diverse melt inclusion chemistry, so
1766 encourage users to take advantage of the ease and speed of calculations in VESIcal
1767 to determine the saturation pressure for each melt inclusion of interest. Saturation
1768 pressures can then be visualized as various cumulative frequency distributions, his-
1769 tograms, or violin plots, and plotted against melt inclusion H₂O and CO₂ contents,
1770 or parameters relating to host crystal chemistry, to gain greater insight into the
1771 factors controlling magma storage depths within volcanic systems.

1772 Finally, we identify that further experimental constraints are required to ac-
1773 curately estimate volatile solubility in andesitic-dacitic melts, and that further work
1774 is needed to understand the effect of temperature, redox, and non-ideal mixing be-
1775 tween H₂O-CO₂ on volatile solubility.

1776

1777 **Acknowledgments**

1778 PW acknowledges funding from a NERC DTP studentship (NE/L002507/1) and
1779 a National Science Foundation grant (1948862). KI and GMM were supported by
1780 the NASA Jacobs JETS Contract (NNJ13HA01C). We acknowledge support from
1781 the National Science Foundation, ICER-20-26904, granted to OFM Research (PI.
1782 Ghiorso) for maintaining the ENKI server used to perform VESIcal calculations. We
1783 thank Jackie Dixon, Giada Iacono-Marziano, Paolo Papale, and Mark Ghiorso for
1784 help tracking down and using existing calculation tools, and for help constructing
1785 model calibration datasets. We also thank Mark Ghiorso and Paolo Papale for help-
1786 ful reviews which improved the clarity and robustness of the first version, and David
1787 Neaveon the secon Version. We greatly appreciate the late Peter Fox for his editorial
1788 handling of the first draft of this manuscript, and his overall support for the VESIcal
1789 project.

1790 **Data Availability** The Jupyter notebooks and associated Excel spreadsheets
1791 are hosted at https://github.com/PennyWieser/VESIcal_II, and are archived
1792 with Zenodo (10.5281/zenodo.5798833, <https://zenodo.org/record/5798833>).

1793 Videos showing how to use VESICAL are hosted on YouTube <https://www.youtube>
1794 [.com/channel/UCpvCCs5KMxz0xXWm0seF8Qw](https://www.youtube.com/channel/UCpvCCs5KMxz0xXWm0seF8Qw).

1795 References

- 1796 Allan, J. F., BATIZA, R., PERFIT, M. R., FORNARI, D. J., & SACK, R. O.
1797 (1989). Petrology of lavas from the lamont seamount chain and adjacent
1798 east pacific rise, 10 n. *Journal of Petrology*, 30(5), 1245–1298.
- 1799 Allison, C. M., Roggensack, K., & Clark, A. (2021). Highly explosive basaltic erup-
1800 tions driven by co2 exsolution. *Nature Communications*.
- 1801 Allison, C. M., Roggensack, K., & Clarke, A. B. (2019). H₂O–CO₂ solubility in
1802 alkali-rich mafic magmas: new experiments at mid-crustal pressures. *Contribu-
1803 tions to Mineralogy and Petrology*, 174(7), 58.
- 1804 Anderson. (1974). Evidence for a picritic, volatile-rich magma beneath mt. shasta,
1805 california. *Journal of Petrology*, 15(2), 243–267.
- 1806 Aster, E. M., Wallace, P. J., Moore, L. R., Watkins, J., Gazel, E., & Bodnar, R. J.
1807 (2016). Reconstructing CO₂ concentrations in basaltic melt inclusions using
1808 raman analysis of vapor bubbles. *Journal of Volcanology and Geothermal
1809 Research*, 323, 148–162.
- 1810 Atlas, Z. D., Dixon, J. E., Sen, G., Finny, M., & Martin-Del Pozzo, A. L. (2006).
1811 Melt inclusions from volcán popocatepetl and volcán de colima, mexico: melt
1812 evolution due to vapor-saturated crystallization during ascent. *Journal of
1813 Volcanology and Geothermal Research*, 153(3-4), 221–240.
- 1814 Behrens, H., Ohlhorst, S., Holtz, F., & Champenois, M. (2004). CO₂ solubility in
1815 dacitic melts equilibrated with H₂O–CO₂ fluids: Implications for modeling the
1816 solubility of CO₂ in silicic melts. *Geochimica et Cosmochimica Acta*, 68(22),
1817 4687–4703.
- 1818 Blank, J., Stolper, E., & Carroll, M. (1993). Solubilities of carbon dioxide and water
1819 in rhyolitic melt at 850 c and 750 bars. *Earth and Planetary Science Letters*,
1820 119(1-2), 27–36.
- 1821 Blundy, J., & Cashman, K. (2005). Rapid decompression-driven crystallization
1822 recorded by melt inclusions from mount st. helens volcano. *Geology*, 33(10),
1823 793–796.
- 1824 Blundy, J., Cashman, K., & Humphreys, M. (2006). Magma heating by

- 1825 decompression-driven crystallization beneath andesite volcanoes. *Nature*,
1826 *443*(7107), 76–80.
- 1827 Botcharnikov, R. E., Behrens, H., & Holtz, F. (2006). Solubility and speciation of
1828 c–o–h fluids in andesitic melt at t= 1100–1300 c and p= 200 and 500 mpa.
1829 *Chemical Geology*, *229*(1-3), 125–143.
- 1830 Botcharnikov, R. E., Holtz, F., & Behrens, H. (2007). The effect of co2 on the solu-
1831 bility of h2o-cl fluids in andesitic melt. *European Journal of Mineralogy*, *19*(5),
1832 671–680.
- 1833 Bowen, N. (1928). The evolution of the igneous rocks, princeton, univ. *Press*,
1834 *Princeton, New Jersey*.
- 1835 Brooker, R., Kohn, S., Holloway, J., & McMillan, P. (2001a). Structural controls on
1836 the solubility of co2 in silicate melts: part i: bulk solubility data. *Chemical Ge-*
1837 *ology*, *174*(1-3), 225–239.
- 1838 Brooker, R., Kohn, S., Holloway, J., & McMillan, P. (2001b). Structural controls
1839 on the solubility of co2 in silicate melts: part ii: Ir characteristics of carbonate
1840 groups in silicate glasses. *Chemical Geology*, *174*(1-3), 241–254.
- 1841 Bucholz, C. E., Gaetani, G. A., Behn, M. D., & Shimizu, N. (2013). Post-
1842 entrapment modification of volatiles and oxygen fugacity in olivine-hosted
1843 melt inclusions. *Earth and Planetary Science Letters*, *374*, 145–155.
- 1844 Bureau, H., & Keppler, H. (1999). Complete miscibility between silicate melts and
1845 hydrous fluids in the upper mantle: experimental evidence and geochemical
1846 implications. *Earth and Planetary Science Letters*, *165*(2), 187–196.
- 1847 Burgisser, A., Alletti, M., & Scaillet, B. (2015). Simulating the behavior of volatiles
1848 belonging to the c–o–h–s system in silicate melts under magmatic conditions
1849 with the software d-compress. *Computers & Geosciences*, *79*, 1–14.
- 1850 Burnham, C. W. (1979). The importance of volatile constituents. *The evolution of*
1851 *the igneous rocks*, 439–482.
- 1852 Burnham, C. W., & Davis, N. (1971). The role of h 2 o in silicate melts; i, pvt rela-
1853 tions in the system naalsi 3 o 8-h 2 o to 10 kilobars and 1000 degrees c. *Amer-*
1854 *ican Journal of Science*, *270*(1), 54–79.
- 1855 Burnham, C. W., & Davis, N. (1974). The role of h 2 o in silicate melts; ii, ther-
1856 modynamic and phase relations in the system naalsi 3 o 8-h 2 o to 10 kilobars,
1857 700 degrees to 1100 degrees c. *American Journal of Science*, *274*(8), 902–940.

- 1858 Cassidy, M., Edmonds, M., Watt, S. F., Palmer, M. R., & Gernon, T. M. (2015).
1859 Origin of basalts by hybridization in andesite-dominated arcs. *Journal of*
1860 *Petrology*, *56*(2), 325–346.
- 1861 Cocheo, P., & Holloway, J. (1993). The solubility of h₂O in basanitic melts at low
1862 pressure. *EOS Transactions of the American Geophysical Union* *74*.
- 1863 Cottrell, E., Lanzirotti, A., Mysen, B., Birner, S., Kelley, K. A., Botcharnikov, R.,
1864 ... Newville, M. (2018). A mössbauer-based xanes calibration for hydrous
1865 basalt glasses reveals radiation-induced oxidation of Fe. *American Mineralogist:*
1866 *Journal of Earth and Planetary Materials*, *103*(4), 489–501.
- 1867 Debret, B., & Sverjensky, D. (2017). Highly oxidising fluids generated during serpen-
1868 tinite breakdown in subduction zones. *Scientific reports*, *7*(1), 1–6.
- 1869 Dingwell, D. B. (1986). Volatile solubilities in silicate melts.
- 1870 Dixon, J. E. (1997). Degassing of alkalic basalts. *American Mineralogist*, *82*(3-4),
1871 368–378.
- 1872 Dixon, J. E., Stolper, E. M., & Holloway, J. R. (1995). An experimental study of
1873 water and carbon dioxide solubilities in mid-ocean ridge basaltic liquids. part i:
1874 calibration and solubility models. *Journal of Petrology*, *36*(6), 1607–1631.
- 1875 Duan, X. (2014). A general model for predicting the solubility behavior of h₂O–CO₂
1876 fluids in silicate melts over a wide range of pressure, temperature and composi-
1877 tions. *Geochimica et Cosmochimica Acta*, *125*, 582–609.
- 1878 Duan, Z., & Zhang, Z. (2006). Equation of state of the h₂O, CO₂, and h₂O–CO₂ sys-
1879 tems up to 10 gpa and 2573.15 K: Molecular dynamics simulations with ab
1880 initio potential surface. *Geochimica et cosmochimica acta*, *70*(9), 2311–2324.
- 1881 Eggler, D. (1973). Role of CO₂ in melting processes in the mantle. *Carnegie Inst.*
1882 *Wash. Yearb*, *72*, 457–467.
- 1883 Eguchi, J., & Dasgupta, R. (2018). A CO₂ solubility model for silicate melts from
1884 fluid saturation to graphite or diamond saturation. *Chemical Geology*, *487*,
1885 23–38.
- 1886 Facq, S., Daniel, I., Montagnac, G., Cardon, H., & Sverjensky, D. A. (2014). In situ
1887 raman study and thermodynamic model of aqueous carbonate speciation in
1888 equilibrium with aragonite under subduction zone conditions. *Geochimica et*
1889 *Cosmochimica Acta*, *132*, 375–390.
- 1890 Fine, G., & Stolper, E. (1986). Dissolved carbon dioxide in basaltic glasses: con-

- 1891 concentrations and speciation. *Earth and Planetary Science Letters*, *76*(3-4), 263–
1892 278.
- 1893 Flowers, G. C. (1979). Correction of holloway’s (1977) adaptation of the modified
1894 redlich-kwong equation of state for calculation of the fugacities of molecular
1895 species in supercritical fluids of geologic interest. *Contributions to Mineralogy
1896 and Petrology*, *69*(3), 315–318.
- 1897 Fogel, R. A., & Rutherford, M. J. (1990). The solubility of carbon dioxide in rhy-
1898 olitic melts; a quantitative ftir study. *American Mineralogist*, *75*(11-12), 1311–
1899 1326.
- 1900 Freise, M. (2004). *Differenzierung von basalten einer “large igneous province”
1901 am beispiel des kerguelen plateaus. eine experimentelle studie* (Unpublished
1902 doctoral dissertation). PhD thesis, University of Hannover.
- 1903 Gaborieau, M., Laubier, M., Bolfan-Casanova, N., Mccammon, C., Vantelon, D.,
1904 Chumakov, A., . . . Venugopal, S. (2020). Determination of fe³⁺/σfe of olivine-
1905 hosted melt inclusions using mössbauer and xanes spectroscopy. *Chemical
1906 Geology*, 119646.
- 1907 Gaetani, G. A., O’Leary, J. A., Shimizu, N., Bucholz, C. E., & Newville, M. (2012).
1908 Rapid reequilibration of h₂o and oxygen fugacity in olivine-hosted melt inclu-
1909 sions. *Geology*, *40*(10), 915–918.
- 1910 Gavrilenko, M., Krawczynski, M., Ruprecht, P., Li, W., & Catalano, J. G. (2019).
1911 The quench control of water estimates in convergent margin magmas. *Ameri-
1912 can Mineralogist: Journal of Earth and Planetary Materials*, *104*(7), 936–948.
- 1913 Gerlach, T. M. (1986). Exsolution of h₂o, co₂, and s during eruptive episodes at ki-
1914 lauea volcano, hawaii. *Journal of Geophysical Research: Solid Earth*, *91*(B12),
1915 12177–12185.
- 1916 Ghiorso, M. S., Carmichael, I. S., Rivers, M. L., & Sack, R. O. (1983). The gibbs
1917 free energy of mixing of natural silicate liquids; an expanded regular solution
1918 approximation for the calculation of magmatic intensive variables. *Contribu-
1919 tions to Mineralogy and Petrology*, *84*(2), 107–145.
- 1920 Ghiorso, M. S., & Gualda, G. A. (2015). An h₂o–co₂ mixed fluid saturation model
1921 compatible with rhyolite-melts. *Contributions to Mineralogy and Petrology*,
1922 *169*(6), 1–30.
- 1923 Ghiorso, M. S., & Sack, R. O. (1995). Chemical mass transfer in magmatic pro-

- 1924 cesses iv. a revised and internally consistent thermodynamic model for the
1925 interpolation and extrapolation of liquid-solid equilibria in magmatic systems
1926 at elevated temperatures and pressures. *Contributions to Mineralogy and*
1927 *Petrology*, 119(2-3), 197–212.
- 1928 Ghiorso, M. S., & Sverjensky, D. A. (2016). The melts-dew connection: Integration
1929 of thermodynamic models for magmatic systems and aqueous fluids at elevated
1930 temperatures and pressures. In *Agu fall meeting abstracts* (Vol. 2016, pp.
1931 V33H–04).
- 1932 Gleeson, M. L., Gibson, S. A., & Williams, H. M. (2020). Novel insights from fe-
1933 isotopes into the lithological heterogeneity of ocean island basalts and plume-
1934 influenced morbs. *Earth and Planetary Science Letters*, 535, 116114.
- 1935 Gleeson, M. L., Stock, M. J., Pyle, D. M., Mather, T. A., Hutchison, W., Yirgu,
1936 G., & Wade, J. (2017). Constraining magma storage conditions at a restless
1937 volcano in the main ethiopian rift using phase equilibria models. *Journal of*
1938 *Volcanology and Geothermal Research*, 337, 44–61.
- 1939 Goltz, A. E., Krawczynski, M. J., Gavrilenko, M., Gorbach, N. V., & Ruprecht, P.
1940 (2020). Evidence for superhydrous primitive arc magmas from mafic enclaves
1941 at shiveluch volcano, kamchatka. *Contributions to Mineralogy and Petrology*,
1942 175(12), 1–26.
- 1943 Goranson, R. W. (1931). Solubility of water in granite magmas. *Eos, Transactions*
1944 *American Geophysical Union*, 12(1), 183–183.
- 1945 Gualda, G. A., & Ghiorso, M. S. (2015). Melts _ e xcel: Am icrosoft e xcel-based
1946 melts interface for research and teaching of magma properties and evolution.
1947 *Geochemistry, Geophysics, Geosystems*, 16(1), 315–324.
- 1948 Gualda, G. A., Ghiorso, M. S., Lemons, R. V., & Carley, T. L. (2012). Rhyolite-
1949 melts: a modified calibration of melts optimized for silica-rich, fluid-bearing
1950 magmatic systems. *Journal of Petrology*, 53(5), 875–890.
- 1951 Hamilton, D., Burnham, C. W., & Osborn, E. (1964). The solubility of water and ef-
1952 fects of oxygen fugacity and water content on crystallization in mafic magmas.
1953 *Journal of Petrology*, 5(1), 21–39.
- 1954 Hartley, M. E., Maclennan, J., Edmonds, M., & Thordarson, T. (2014). Reconstruct-
1955 ing the deep co₂ degassing behaviour of large basaltic fissure eruptions. *Earth*
1956 *and Planetary Science Letters*, 393, 120–131.

- 1957 Hartley, M. E., Neave, D. A., MacLennan, J., Edmonds, M., & Thordarson, T.
1958 (2015). Diffusive over-hydration of olivine-hosted melt inclusions. *Earth*
1959 *and Planetary Science Letters*, *425*, 168–178.
- 1960 Hauri, E. (2002). Sims analysis of volatiles in silicate glasses, 2: isotopes and abun-
1961 dances in hawaiian melt inclusions. *Chemical Geology*, *183*(1-4), 115–141.
- 1962 Hauri, E., Kent, A. J., & Arndt, N. (2002). Melt inclusions at the millennium: to-
1963 ward a deeper understanding of magmatic processes. *ChGeo*, *183*(1-4), 1–3.
- 1964 Helz, R., & Thornber, C. R. (1987). Geothermometry of kilauea iki lava lake, hawaii.
1965 *Bulletin of Volcanology*, *49*(5), 651–668.
- 1966 Hervig, R., Dunbar, N., Westrich, H. R., & Kyle, P. R. (1989). Pre-eruptive water
1967 content of rhyolitic magmas as determined by ion microprobe analyses of melt
1968 inclusions in phenocrysts. *Journal of Volcanology and Geothermal Research*,
1969 *36*(4), 293–302.
- 1970 Hervig, R., & Williams, P. (1988). Sims microanalysis of minerals and glasses for h
1971 and d. *SIMS VI Proceedings*, 961–964.
- 1972 Hess, K., & Dingwell, D. (1996). Viscosities of hydrous leucogranitic melts: A non-
1973 arrhenian model. *American Mineralogist*, *81*(9-10), 1297–1300.
- 1974 Holloway, J. R. (1977). Fugacity and activity of molecular species in supercritical
1975 fluids. In *Thermodynamics in geology* (pp. 161–181). Springer.
- 1976 Holloway, J. R., & Blank, J. G. (1994). Application of experimental results to coh
1977 species in natural melts. *Reviews in mineralogy*, *30*, 187–187.
- 1978 Huang, F., & Sverjensky, D. A. (2019). Extended deep earth water model for pre-
1979 dicting major element mantle metasomatism. *Geochimica et Cosmochimica*
1980 *Acta*, *254*, 192–230.
- 1981 Huber, C., Townsend, M., Degruyter, W., & Bachmann, O. (2019). Optimal depth
1982 of subvolcanic magma chamber growth controlled by volatiles and crust rheol-
1983 ogy. *Nature Geoscience*, *12*(9), 762–768.
- 1984 Huppert, H. E., & Woods, A. W. (2002). The role of volatiles in magma chamber
1985 dynamics. *Nature*, *420*(6915), 493–495.
- 1986 Husen, A., Almeev, R. R., & Holtz, F. (2016). The effect of h₂o and pressure on
1987 multiple saturation and liquid lines of descent in basalt from the shatsky rise.
1988 *Journal of Petrology*, *57*(2), 309–344.
- 1989 Iacono-Marziano, G., Morizet, Y., Le Trong, E., & Gaillard, F. (2012). New experi-

- 1990 mental data and semi-empirical parameterization of h₂o-co₂ solubility in mafic
1991 melts. *Geochimica et Cosmochimica Acta*, *97*, 1–23.
- 1992 Iacovino, K., Guild, M. R., & Till, C. B. (2020). Aqueous fluids are effective oxidiz-
1993 ing agents of the mantle in subduction zones. *Contributions to Mineralogy and*
1994 *Petrology*, *175*(4), 1–21.
- 1995 Iacovino, K., Matthews, S., Wieser, P. E., Moore, G., & Begue, F. (2021). Vesi-
1996 cal part i: An open source thermodynamic model engine for mixed volatile
1997 solubility in silicate melts. *EarthArxiv* -<https://doi.org/10.31223/X5D606>.
- 1998 Iacovino, K., Moore, G., Roggensack, K., Oppenheimer, C., & Kyle, P. (2013). H₂
1999 o-co₂ solubility in mafic alkaline magma: applications to volatile sources and
2000 degassing behavior at erebus volcano, antarctica. *Contributions to Mineralogy*
2001 *and Petrology*, *166*(3), 845–860.
- 2002 Iddon, F., & Edmonds, M. (2020). Volatile-rich magmas distributed through the
2003 upper crust in the main ethiopian rift. *Geochemistry, Geophysics, Geosystems*,
2004 *21*(6), e2019GC008904.
- 2005 Jakobsson, S. (1997). Solubility of water and carbon dioxide in an icelandite at 1400
2006 c and 10 kilobars. *Contributions to Mineralogy and Petrology*, *127*(1-2), 129–
2007 135.
- 2008 Kerrick, D., & Jacobs, G. (1981). A modified redlich-kwong equation for h₂ o, co
2009 2, and h₂ o-co₂ mixtures at elevated pressures and temperatures. *American*
2010 *Journal of Science*, *281*(6), 735–767.
- 2011 King, P., & Holloway, J. (2002). Co₂ solubility and speciation in intermediate (an-
2012 desitic) melts: the role of h₂o and composition. *Geochimica et Cosmochimica*
2013 *Acta*, *66*(9), 1627–1640.
- 2014 Koleszar, A., Kent, A. J., Wallace, P. J., & Scott, W. E. (2012). Controls on long-
2015 term low explosivity at andesitic arc volcanoes: Insights from mount hood,
2016 oregon. *Journal of Volcanology and Geothermal Research*, *219*, 1–14.
- 2017 Koleszar, A., Saal, A., Hauri, E., Nagle, A., Liang, Y., & Kurz, M. (2009). The
2018 volatile contents of the galapagos plume; evidence for h₂o and f open system
2019 behavior in melt inclusions. *Earth and Planetary Science Letters*, *287*(3-4),
2020 442–452.
- 2021 La Spina, G., Arzilli, F., Llewellyn, E., Burton, M., Clarke, A. B., Vitturi, M. d.,
2022 ... Mader, H. (2021). Explosivity of basaltic lava fountains is controlled by

- 2023 magma rheology, ascent rate and outgassing. *Earth and Planetary Science*
2024 *Letters*, 553, 116658.
- 2025 Lesne, P., Scaillet, B., Pichavant, M., & Beny, J.-M. (2011). The carbon dioxide
2026 solubility in alkali basalts: an experimental study. *Contributions to Mineralogy*
2027 *and Petrology*, 162(1), 153–168.
- 2028 Lesne, P., Scaillet, B., Pichavant, M., Iacono-Marziano, G., & Beny, J.-M. (2011).
2029 The h₂o solubility of alkali basaltic melts: an experimental study. *Contribu-*
2030 *tions to Mineralogy and Petrology*, 162(1), 133–151.
- 2031 Le Voyer, M., Hauri, E., Cottrell, E., Kelley, K. A., Salters, V. J., Langmuir, C. H.,
2032 ... Füre, E. (2019). Carbon fluxes and primary magma co₂ contents along the
2033 global mid-ocean ridge system. *Geochemistry, Geophysics, Geosystems*, 20(3),
2034 1387–1424.
- 2035 Li, Y., Dasgupta, R., & Tsuno, K. (2017). Carbon contents in reduced basalts at
2036 graphite saturation: Implications for the degassing of mars, mercury, and the
2037 moon. *Journal of Geophysical Research: Planets*, 122(6), 1300–1320.
- 2038 Liu, Y., Zhang, Y., & Behrens, H. (2005). Solubility of h₂o in rhyolitic melts at low
2039 pressures and a new empirical model for mixed h₂o–co₂ solubility in rhyolitic
2040 melts. *Journal of Volcanology and Geothermal Research*, 143(1-3), 219–235.
- 2041 Lloyd, A. S., Plank, T., Ruprecht, P., Hauri, E., & Rose, W. (2013). Volatile loss
2042 from melt inclusions in pyroclasts of differing sizes. *Contributions to Mineral-*
2043 *ogy and Petrology*, 165(1), 129–153.
- 2044 Lowenstern, J. B. (1995). Applications of silicate-melt inclusions to the study of
2045 magmatic volatiles. *Magmas, fluids and ore deposits*, 23, 71–99.
- 2046 Lowenstern, J. B. (2001). Carbon dioxide in magmas and implications for hydrother-
2047 mal systems. *Mineralium Deposita*, 36(6), 490–502.
- 2048 Lowenstern, J. B. (2003). Melt inclusions come of age: volatiles, volcanoes, and
2049 sorby’s legacy. In *Developments in volcanology* (Vol. 5, pp. 1–21). Elsevier.
- 2050 Lucic, G., Berg, A.-S., & Stix, J. (2016). Water-rich and volatile-undersaturated
2051 magmas at hekla volcano, iceland. *Geochemistry, Geophysics, Geosystems*,
2052 17(8), 3111–3130.
- 2053 MacLennan, J. (2017). Bubble formation and decrepitation control the co₂ content of
2054 olivine-hosted melt inclusions. *Geochemistry, Geophysics, Geosystems*, 18(2),
2055 597–616.

- 2056 Makhluף, A. R., Newton, R., & Manning, C. (2020). Experimental investigation of
2057 phase relations in the system $\text{NaAlSi}_3\text{O}_8$ – H_2O at high temperatures and pres-
2058 sures: liquidus relations, liquid–vapor mixing, and critical phenomena at deep
2059 crust–upper mantle conditions. *Contributions to Mineralogy and Petrology*,
2060 *175*(8), 1–20.
- 2061 Mangan, M. T., Sisson, T. W., Hankins, W. B., Shimizu, N., & Vennemann, T.
2062 (2021). Constraints on deep, CO_2 -rich degassing at arc volcanoes from solubility
2063 experiments on hydrous basaltic andesite of Pavlof volcano, Alaska peninsula,
2064 at 300 to 1200 MPa. *American Mineralogist: Journal of Earth and Planetary*
2065 *Materials*, *106*(5), 762–773.
- 2066 Métrich, N., & Wallace, P. J. (2008). Volatile abundances in basaltic magmas and
2067 their degassing paths tracked by melt inclusions. *Reviews in Mineralogy and*
2068 *Geochemistry*, *69*(1), 363–402.
- 2069 Mironov, N., Tobelko, D., Smirnov, S., Portnyagin, M. V., & Krasheninnikov, S.
2070 (2020). Estimation of CO_2 content in the gas phase of melt inclusions using
2071 Raman spectroscopy: Case study of inclusions in olivine from the Karymsky
2072 volcano (Kamchatka). *Russian Geology and Geophysics*, *61*(5-6), 600–610.
- 2073 Mitchell, A. L., Gaetani, G. A., O’Leary, J. A., & Hauri, E. H. (2017). H_2O sol-
2074 ubility in basalt at upper mantle conditions. *Contributions to Mineralogy and*
2075 *Petrology*, *172*(10), 1–16.
- 2076 Moore, G. (2008). Interpreting H_2O and CO_2 contents in melt inclusions: constraints
2077 from solubility experiments and modeling. *Reviews in Mineralogy and Geo-*
2078 *chemistry*, *69*(1), 333–362.
- 2079 Moore, G., & Carmichael, I. (1998). The hydrous phase equilibria (to 3 kbar) of
2080 an andesite and basaltic andesite from western Mexico: constraints on water
2081 content and conditions of phenocryst growth. *Contributions to Mineralogy and*
2082 *Petrology*, *130*(3-4), 304–319.
- 2083 Moore, G., Roggensack, K., & Klonowski, S. (2008). A low-pressure–high-
2084 temperature technique for the piston-cylinder. *American Mineralogist*, *93*(1),
2085 48–52.
- 2086 Moore, G., Vennemann, T., & Carmichael, I. (1998). An empirical model for the sol-
2087 ubility of H_2O in magmas to 3 kilobars. *American Mineralogist*, *83*(1), 36–42.
- 2088 Moore, L. R., Gazel, E., Tuohy, R., Lloyd, A. S., Esposito, R., Steele-MacInnis, M.,

- 2089 ... Bodnar, R. J. (2015). Bubbles matter: An assessment of the contribution
2090 of vapor bubbles to melt inclusion volatile budgets. *American Mineralogist*,
2091 *100*(4), 806–823.
- 2092 Mutch, E. J., Maclennan, J., Shorttle, O., Edmonds, M., & Rudge, J. F. (2019).
2093 Rapid transcrustal magma movement under iceland. *Nature Geoscience*, *12*(7),
2094 569–574.
- 2095 Mysen, B. O. (1976). The role of volatiles in silicate melts; solubility of carbon
2096 dioxide and water in feldspar, pyroxene, and feldspathoid melts to 30 kb and
2097 1625 degrees c. *American Journal of Science*, *276*(8), 969–996.
- 2098 Mysen, B. O., Egger, D. H., Seitz, M., & Holloway, J. R. (1976). Carbon dioxide in
2099 silicate melts and crystals; part i, solubility measurements. *American Journal*
2100 *of Science*, *276*(4), 455–479.
- 2101 Mysen, B. O., Fogel, M. L., Morrill, P. L., & Cody, G. D. (2009). Solution behavior
2102 of reduced coh volatiles in silicate melts at high pressure and temperature.
2103 *Geochimica et Cosmochimica Acta*, *73*(6), 1696–1710.
- 2104 Newman, S., & Lowenstern, J. B. (2002). Volatilecalc: a silicate melt–h₂o–co₂ solu-
2105 tion model written in visual basic for excel. *Computers & Geosciences*, *28*(5),
2106 597–604.
- 2107 Ochs, F. A., & Lange, R. A. (1999). The density of hydrous magmatic liquids. *Sci-*
2108 *ence*, *283*(5406), 1314–1317.
- 2109 Papale, P. (1997). Modeling of the solubility of a one-component h₂o or co₂
2110 fluid in silicate liquids. *Contributions to Mineralogy and Petrology*, *126*(3),
2111 237–251.
- 2112 Papale, P. (1999). Modeling of the solubility of a two-component h₂o+ co₂ fluid in
2113 silicate liquids. *American Mineralogist*, *84*(4), 477–492.
- 2114 Papale, P., Moretti, R., & Barbato, D. (2006). The compositional dependence of
2115 the saturation surface of h₂o+ co₂ fluids in silicate melts. *Chemical Geology*,
2116 *229*(1-3), 78–95.
- 2117 Papale, P., Neri, A., & Macedonio, G. (1999). The role of water content and magma
2118 composition on explosive eruption dynamics. *Physics and Chemistry of the*
2119 *Earth, Part A: Solid Earth and Geodesy*, *24*(11-12), 969–975.
- 2120 Plank, T., Kelley, K. A., Zimmer, M. M., Hauri, E., & Wallace, P. J. (2013). Why
2121 do mafic arc magmas contain 4 wt% water on average? *Earth and Planetary*

- 2122 *Science Letters*, 364, 168–179.
- 2123 Portnyagin, M., Almeev, R., Matveev, S., & Holtz, F. (2008). Experimental evidence
2124 for rapid water exchange between melt inclusions in olivine and host magma.
2125 *Earth and Planetary Science Letters*, 272(3-4), 541–552.
- 2126 Putirka, K. D. (2008). Thermometers and barometers for volcanic systems. *Reviews*
2127 *in Mineralogy and Geochemistry*, 69(1), 61–120.
- 2128 Rasmussen, D. J., Plank, T. A., Wallace, P. J., Newcombe, M. E., & Lowenstern,
2129 J. B. (2020). Vapor-bubble growth in olivine-hosted melt inclusions. *American*
2130 *Mineralogist: Journal of Earth and Planetary Materials*, 105(12), 1898–1919.
- 2131 Reubi, O., & Blundy, J. (2009). A dearth of intermediate melts at subduction zone
2132 volcanoes and the petrogenesis of arc andesites. *Nature*, 461(7268), 1269–
2133 1273.
- 2134 Roedder, E. (1979). Origin and significance of magmatic inclusions. *Bulletin de Min-*
2135 *eralogie*, 102(5), 487–510.
- 2136 Roggensack, K. (2001). Unraveling the 1974 eruption of fuego volcano (guatemala)
2137 with small crystals and their young melt inclusions. *Geology*, 29(10), 911–914.
- 2138 Rohatgi, A. (2017). *Webplotdigitizer*. Austin, Texas, USA.
- 2139 Saal, A. E., Hauri, E., Langmuir, C. H., & Perfit, M. R. (2002). Vapour undersat-
2140 uration in primitive mid-ocean-ridge basalt and the volatile content of earth’s
2141 upper mantle. *Nature*, 419(6906), 451–455.
- 2142 Shishkina, T., Botcharnikov, R. E., Holtz, F., Almeev, R., & Portnyagin, M. V.
2143 (2010). Solubility of h₂o-and co₂-bearing fluids in tholeiitic basalts at pressures
2144 up to 500 mpa. *Chemical geology*, 277(1-2), 115–125.
- 2145 Shishkina, T., Botcharnikov, R. E., Holtz, F., Almeev, R. R., Jazwa, A. M., & Jaku-
2146 biak, A. A. (2014). Compositional and pressure effects on the solubility of h₂o
2147 and co₂ in mafic melts. *Chemical Geology*, 388, 112–129.
- 2148 Sides, I., Edmonds, M., MacLennan, J., Swanson, D., & Houghton, B. (2014a). Erup-
2149 tion style at kilauea volcano in hawai ‘i linked to primary melt composition.
2150 *Nature Geoscience*, 7(6), 464.
- 2151 Sides, I., Edmonds, M., MacLennan, J., Swanson, D., & Houghton, B. (2014b).
2152 Magma mixing and high fountaining during the 1959 kilauea iki eruption,
2153 hawai ‘i. *Earth and Planetary Science Letters*, 400, 102–112.
- 2154 Silver, L. A. (1988). *Water in silicate glasses* (Unpublished doctoral dissertation).

- 2155 California Institute of Technology.
- 2156 Silver, L. A., Ihinger, P. D., & Stolper, E. (1990). The influence of bulk composition
2157 on the speciation of water in silicate glasses. *Contributions to Mineralogy and*
2158 *Petrology*, *104*(2), 142–162.
- 2159 Silver, L. A., & Stolper, E. (1989). Water in albitic glasses. *Journal of petrology*,
2160 *30*(3), 667–709.
- 2161 Steele-Macinnis, M., Esposito, R., & Bodnar, R. J. (2011). Thermodynamic model
2162 for the effect of post-entrapment crystallization on the H_2O - CO_2 systematics
2163 of vapor-saturated, silicate melt inclusions. *Journal of Petrology*, *52*(12),
2164 2461–2482.
- 2165 Stevenson, J. (2015). *Tasplot*. [https://bitbucket.org/jsteven5/tasplot/src/](https://bitbucket.org/jsteven5/tasplot/src/master/)
2166 [master/](https://bitbucket.org/jsteven5/tasplot/src/master/). bitbucket.
- 2167 Stolper, E. (1982). Water in silicate glasses: an infrared spectroscopic study. *Contri-*
2168 *butions to Mineralogy and Petrology*, *81*(1), 1–17.
- 2169 Stolper, E., Fine, G., Johnson, T., & Newman, S. (1987). Solubility of carbon diox-
2170 ide in albitic melt. *American Mineralogist*, *72*(11-12), 1071–1085.
- 2171 Sverjensky, D. A., Harrison, B., & Azzolini, D. (2014). Water in the deep earth: the
2172 dielectric constant and the solubilities of quartz and corundum to 60 kb and
2173 1200 c. *Geochimica et Cosmochimica Acta*, *129*, 125–145.
- 2174 Tamura, Y., & Tatsumi, Y. (2002). Remelting of an andesitic crust as a possible
2175 origin for rhyolitic magma in oceanic arcs: an example from the Izu–Bonin arc.
2176 *Journal of Petrology*, *43*(6), 1029–1047.
- 2177 Tucker, J. M., Hauri, E., Pietruszka, A. J., Garcia, M. O., Marske, J. P., & Trusdell,
2178 F. A. (2019). A high carbon content of the Hawaiian mantle from olivine-
2179 hosted melt inclusions. *Geochimica et Cosmochimica Acta*, *254*, 156–172.
- 2180 Tuttle, O. F., & Bowen, N. L. (1958). *Origin of granite in the light of experimental*
2181 *studies in the system NaAlSi₃O₈-KAlSi₃O₈-SiO₂-H₂O* (Vol. 74). Geological Society
2182 of America.
- 2183 Venugopal, S., Schiavi, F., Moune, S., Bolfan-Casanova, N., Druitt, T., & Williams-
2184 Jones, G. (2020). Melt inclusion vapour bubbles: the hidden reservoir for
2185 major and volatile elements. *Scientific Reports*, *10*(1), 1–14.
- 2186 Wallace, P. J., Anderson, A. T., & Davis, A. M. (1995). Quantification of pre-
2187 eruptive exsolved gas contents in silicic magmas. *Nature*, *377*(6550), 612–616.

- 2188 Waters, L. E., & Lange, R. A. (2013). Crystal-poor, multiply saturated rhyolites
2189 (obsidians) from the cascade and mexican arcs: evidence of degassing-induced
2190 crystallization of phenocrysts. *Contributions to Mineralogy and Petrology*,
2191 *166*(3), 731–754.
- 2192 Waters, L. E., & Lange, R. A. (2015). An updated calibration of the plagioclase-
2193 liquid hygrometer-thermometer applicable to basalts through rhyolites. *Ameri-
2194 can Mineralogist*, *100*(10), 2172–2184.
- 2195 Wieser, P. E., Lamadrid, H., Maclennan, J., Edmonds, M., Matthews, S., Iacovino,
2196 K., . . . others (2021). Reconstructing magma storage depths for the 2018
2197 kilauean eruption from melt inclusion co2 contents: the importance of vapor
2198 bubbles. *Geochemistry, Geophysics, Geosystems*, *22*(2), e2020GC009364.